

AN INVESTIGATION OF EMISSIONS AND EFFICIENCY
CHARACTERISTICS OF A PHOSPHORIC ACID
FUEL CELL ENGINE

By

JAMES H. FLETCHER

A DISSERTATION PRESENTED TO THE GRADUATE SCHOOL
OF THE UNIVERSITY OF FLORIDA IN PARTIAL FULFILLMENT
OF THE REQUIREMENTS FOR THE DEGREE OF
DOCTOR OF PHILOSOPHY

UNIVERSITY OF FLORIDA

1999

ACKNOWLEDGEMENTS

I thank my family and friends for their overwhelming support, especially Sydney. Dr. Roan's commitment and contributions to my studies were invaluable and very much appreciated. I would like to thank my co-workers in the laboratory as well as my committee members for their insight and challenges. Finally, I thank Becky Hoover for her understanding and her patience.

TABLE OF CONTENTS

	<u>Page</u>
ACKNOWLEDGEMENTS	ii
LIST OF TABLES	vii
LIST OF FIGURES	x
ABSTRACT	xv
CHAPTERS	
1 INTRODUCTION	1
2 LITERATURE REVIEW	6
Introduction	6
Fuel Delivery System	7
Hydrogen	8
Hydrogen storage	8
Hydrogen refueling	10
Cost and infrastructure	11
Other Fuels	12
Reforming Process	15
Steam Reforming	16
Partial oxidation reforming	17
Autothermal reforming	18
Preferential Oxidation (PROX)	19
Methanol Steam Reforming	20
Thermodynamics	20
Kinetics	22
Fuel Cell Stack Models	25
Introduction	25
Background	25
Stack Modeling Goals	27
Performance Parameters	29
Current density	31
Stack temperature	31
Carbon monoxide poisoning	31
Other performance factors	33
Cell/Stack Models	34
System Models	37
Design Point Models	39
Off-Design Models	43
Efficiency	46

Introduction.....	46
Efficiency Definitions.....	47
Thermodynamic efficiency	47
Voltage efficiency	48
Current efficiency.....	49
Electrochemical efficiency	50
Heating value efficiency	50
Fuel cell efficiency	50
Fuel processor efficiency	51
Gross system efficiency.....	51
Net system efficiency	51
Reported Efficiency.....	52
Emissions	53
Fuel Chain Emissions.....	56
 3 FUEL CELL ENGINE DESCRIPTION	 59
Introduction	59
Background	59
Fuel Cell System Description	61
Reformer Subsystem	62
Fuel Cell Stack Subsystem	68
Coolant Loop	70
Power Electronics Subsystem.....	71
Control Subsystem	72
Fuel Cell Engine Operation.....	74
Startup	74
Normal Operation	76
Shutdown	77
 4 EXPERIMENTAL METHOD	 79
Instrumentation and Data Acquisition	79
Introduction.....	79
Control Signals and Strategy	80
Temperature Measurement	83
Pressure Measurement	83
Flow Measurement	84
Parasitic Power Measurement.....	86
Gas and Liquid Analysis.....	87
Liquid reformat component analysis	87
Gas reformat analysis	88
Emissions Testing	89
Data Acquisition	90
Hardware.....	91
Software	94

Brassboard Test Plan	95
Conclusion	97
5 RESULTS AND DISCUSSION	98
Introduction	98
Steady-State Operation	98
Polarization Curves	98
P-01 and P-02 Control	104
Reformate Quality	108
Reformer Catalyst bed Temperatures	109
Reformate condensate Analysis	110
Reformate gas (non-condensable) analysis	114
Fuel Utilization	115
Stack Efficiency	118
Reformer Energy Balance	118
Burner B-01 combustion temperature	122
Reformer exhaust temperature	123
Reformer Burner Trim Pump P-03	127
HX-05 Vaporizer Heat Exchanger	129
Fuel Cell Stack Energy Balance	131
Coolant Loop	132
Coolant Loop Energy Balance	134
HX-01 vaporizer heat exchanger	134
Stack waste heat	136
Startup burner/HX-03 operation	139
Conclusion	143
Total Methanol Flow Rate	145
System Efficiency	149
Power Conditioning	150
Parasitic Power Consumption	152
Net Overall Engine Efficiency	157
Conclusion	160
Transient Operation	160
Introduction	160
Transient Performance	161
Startup and Shutdown	166
Introduction	166
Engine Startup	166
Startup methanol consumption	167
Startup parasitic power consumption	168
Reformer bed catalyst temperatures	170
Engine Shutdown	172
Shutdown methanol consumption	172
Shutdown parasitic power consumption	174
Conclusion	174

Aging Considerations	176
Introduction	176
Reformer Degradation	177
Stack Degradation	177
Conclusions	180
Emissions	180
Introduction	180
Emissions Testing	182
Steady-State Brassboard Testing	183
Reformer Exhaust Port	184
HX-03 Exhaust	188
Total Emissions Levels	188
Startup/Shutdown/Idle Operation	191
Startup process	191
Shutdown	194
Idle condition	195
Conclusion	198
5 CONCLUSIONS AND RECOMENDATIONS	199
Conclusion	199
Recommendations	203
REFERENCES	204
BIOGRAPHICAL SKETCH	210

LIST OF TABLES

<u>Table</u>	<u>page</u>
2.1 Important design parameters of various hydrogen storage methods for a passenger car with 340 mile range	9
2.2 Design goals for on-board storage of hydrogen for a fuel cell powered full-size automobile with 80 miles per gallon gasoline equivalent and 380 mile range	10
2.3 Selected potential fuels for fuel cell systems	13
2.4 Net hydrogen energy per unit weight and volume of selected fuels plus water required for the ideal reforming process	15
2.5 Availability of selected fuels to garner a 10% share of the transportation energy sector	15
2-6 Steam reforming reactions for methane, methanol, and ethanol	16
2-7 Partial oxidation reforming reactions for methane, methanol, and ethanol...	18
2-8 Decomposition reaction scheme for methanol steam reforming	23
2-9 Oxidation-Reduction reaction scheme for methanol steam reforming.....	23
2-10 Typical electrochemical reactions in fuel cells	26
2-11 Abbreviated list of important parameters for the fuel cell stack.....	30
2-12 Equations for phosphoric acid cells.....	38
2-13 System design point parameters	41
2-14 Design point case studies	42
2-15 Results of design point case studies	42
2-16 Reported fuel cell system efficiencies	54

2-17 Results of PC25 emissions testing based on PPMv (15% O ₂ , Dry)	55
2-18 Comparison of PC25 emissions to the utility average on a pounds per mega-watt basis	55
2-19 Comparison of transit bus emissions tested by West Virginia University	56
2-20 Efficiency and emission levels of selected fuel chains	58
3-1 Brassboard fuel cell system specifications	62
3-2 Brassboard steam reformer specifications	68
3-3 Fuel cell stack specifications	69
3-4 Control equipment specifications	74
4-1 Analog input signals	81
4-2 Analog output control signals	82
4-3 Additional thermocouple data	84
4-4 Additional brassboard data	87
4-5 Specifications of the Daqbook 200	92
5-1 Results of P-01 and P-02 flow meter testing	108
5-2 Results of liquid NMR testing	113
5-3 Gas chromatograph results for the dry reformat	115
5-4 Average methanol flow rates of pumps P-01 and P-03	129
5-5 Results of first law steady flow analysis for the fuel cell stack	132
5-6 Results of energy balance for the coolant loop	140
5-7 Methanol flow rates for each pump during steady-state operation	148
5-8 Time required to achieve 90% of steady-state efficiency if startup and shutdown energy is accounted for	176
5-9 Carbon Monoxide (CO) levels for the brassboard engine	190

5-10 Comparison of emission testing of brassboard engine by the University of Florida and Fuji	190
5-11 Normalized Carbon Monoxide (CO) levels for the brassboard engine	191

LIST OF FIGURES

<u>Figure</u>	<u>page</u>
2-1 Typical fuel cell polarization curve	28
2-2 The current density distribution across a typical cell.....	32
2-3 Temperature distribution across a Fuji stack with liquid coolant plates placed every five power producing cells	32
3-1 Simple schematic of the brassboard fuel cell engine	63
3-2 Configuration of the entire brassboard fuel cell engine	64
3-3 Typical methanol steam reformer cross-section	66
3-4 Fuel cell/battery hybrid arrangement	73
4-1 Brassboard schematic with transducer locations	93
5-1 Brassboard fuel cell engine polarization curve and stack power output.....	100
5-2 Brassboard fuel cell engine steady-state normalized polarization curve and stack efficiency curve.....	100
5-3 Brassboard fuel cell engine polarization curve history since manufacture...	103
5-4 Brassboard fuel cell engine polarization curve history while at the University of Florida.....	103
5-5 Relationship between stack temperature and stack voltage at 25% of design stack power output	105
5-6 Graph of the actual P-01 and P-02 pump voltages versus calculated values..	105
5-7 Results of pump P-01 methanol flow rate testing at 20C	107
5-8 Calculated equilibrium mole values of CO and H ₂ (per mole of methanol) for methanol steam reforming with steam-to-carbon ratios of 1.0 and 1.5	107

5-9 Reformer bed temperatures at 25% steady-state power output	111
5-10 Reformer bed temperatures at 37.5% steady-state power output	111
5-11 Reformer bed temperatures at 50% steady-state power output	112
5-12 Reformer bed temperatures at 62.5% steady-state power output	112
5-13 Graph of primary methanol fuel flow as a function of stack current	117
5-14 Fuel utilization as a function of the stack current	117
5-15 Brassboard fuel cell stack fuel utilization as a function of stack power output	119
5-16 Stack and average cell efficiency as a function of percent of design power output	119
5-17 Reformer burner thermocouple readings during startup for the 50 kW fuel cell engine	124
5-18 Reformer burner thermocouple readings and calculated adiabatic flame temperature as a function of stack power output	124
5-19 Graph of reformer exhaust temperature and stack power output as a function of time for power outputs between 25% and 75% of design power output (25kW).	126
5-20 The overall heat transfer within the brassboard reformer	126
5-21 Relationship between the middle reformer bed temperature TCA-102 and the P-03 voltage at 25% of design power output	128
5-22 Relationship between the middle reformer bed temperature TCA-102 and the P-03 voltage at 37.5% of design power output	128
5-23 Graph of methanol vaporizer HX-05 temperature (TC-105) and voltage along with the pump P-03 voltage as a function of time at 25% power output	130
5-24 Graph of methanol vaporizer HX-05 temperature (TC-105) and power consumed along with the pump P-03 voltage as a function of time at 37.5% power output	130

5-25 Nominal stack temperature as a function of the percent of design power output	135
5-26 Graph of heat transfer requirements of the vaporizer heat exchanger HX-01. HX-01 transfers heat from the coolant to vaporize the fuel mixture	137
5-27 Graph of stack waste heat transfer to the coolant as a function of the stack current. The normalized waste transfer rate is also included	137
5-28 Graph of the heat transfer rate and the normalized heat transfer rate for HX-01 and the fuel cell stack	138
5-29 Stack coolant inlet temperature and F-02 and P-02 operation for 25% of design power output	142
5-30 Stack coolant inlet temperature and F-02 and P-02 operation for 37.5% of design power output	142
5-31 Stack coolant inlet temperature and F-02 and P-04 operation for 50% of stack design power output	144
5-32 Stack coolant inlet temperature and F-02 and P-04 operation for 62.5% of stack design power output	144
5-33 Graph of the total methanol flow rate as a function of time for 25%, 37.5%, 50%, and 62.5% of the design power output	146
5-34 Instantaneous methanol flow rate for the three fuel pumps during steady state operation at 25% of design power output	147
5-35 Instantaneous methanol flow rate for the three fuel pumps during steady state operation at 37.5% of design power output	147
5-36 Graph of the brassboard fuel cell engine system efficiency as a function of power output. The cell efficiency and stack efficiency are also included	151
5-37 Graph of the DC-DC converter efficiency (power output/power input) as a function of the percent of design power output	151
5-38 Graph of the overall engine efficiency as a function of design power output. The cell, stack, and system efficiency curves are presented for comparison	154

5-39 Typical total parasitic power consumption curve for 25% of design power output	155
5-40 Typical total parasitic power consumption curve for 37.5% of design power output	155
5-41 Typical total parasitic power consumption curve for 50% of design power output	156
5-42 Typical total parasitic power consumption curve for 62.5% of design power output	156
5-43 Important parameters that determine the shape of the parasitic power curve as a function of time for the 25% power output case	158
5-44 Net overall engine efficiency curve for the brassboard engine. Also included are the cell, stack system, overall efficiencies	158
5-45 Instantaneous net overall efficiency for 25% of design power output	159
5-46 Graph of P-01 voltage and P-01 methanol flow rate for an up-transient from 25% to 50% of design power output	164
5-47 Graph of the reformer bed temperatures and P-01 methanol flow rate as a function of time during an up-transient from 25% to 50% of design power output	164
5-48 Graph of reformer bed temperatures as a function of time for repeated transients between 25% and 50% of design power output	165
5-49 Comparison of reformer bed temperatures for steady-state 50% of design power output and transient operation between 37.5% and 62.5% of design power output	165
5-50 Various methanol flow rates as a function of time	169
5-51 Total methanol flow rate during startup as a function of time	169
5-52 Instantaneous parasitic power consumption during startup	171
5-53 Instantaneous parasitic power and important component voltages for startup	171
5-54 Reformer bed temperature profiles during normal startup	173
5-55 Reformer bed temperature profiles during startup where the catalyst bed is overheated	173

5-56 Parasitic power consumption curve for engine shutdown	175
5-57 Catalyst bed temperatures for the 50 kW bus fuel cell engine. The bottom bed has been severely damaged resulting in high bed temperatures.....	179
5-58 Graph showing the increased stack current due to brassboard degradation...	179
5-59 System efficiency curves for the brassboard engine when new (1989) and after 10 years of operation (1999).....	181
5-60 Carbon monoxide levels for the brassboard engine operating at 25% of design power output	185
5-61 Carbon monoxide levels for the brassboard engine operating at 37.5% of design power output.....	185
5-62 Carbon monoxide levels for the brassboard engine operating at 50% of design power output	186
5-63 Carbon monoxide levels for the brassboard engine operating at 62.5% of design power output	186
5-64 Graph of the CO and HC levels for the 50 kW bus fuel cell engine.....	189
5-65 Graph of the CO level for the HX-03 exhaust port at 25% of design power output	189
5-66 Startup CO levels for the reformer burner exhaust during mode 1.....	193
5-67 Startup CO levels for the reformer burner exhaust during mode 2.....	193
5-68 Carbon monoxide level for the HX-03 exhaust port during startup	196
5-69 Carbon monoxide levels for the reformer exhaust port during shutdown	196
5-70 Carbon monoxide levels for the idle condition	197

Abstract of Dissertation Presented to the Graduate School
of the University of Florida in Partial Fulfillment of the
Requirements for the Degree of Doctor of Philosophy

AN INVESTIGATION OF EMISSIONS AND EFFICIENCY
CHARACTERISTICS OF A PHOSPHORIC ACID
FUEL CELL ENGINE

By

James H. Fletcher

December, 1999

Chairman: Vernon P. Roan
Major Department: Mechanical Engineering

There is immense interest in increasing efficiency and reducing emissions from power producing devices. This is especially true of the transportation application which contributes a significant portion of the energy consumption and emission production worldwide. One of the most promising technologies for clean, efficient propulsion systems is the fuel cell.

Based on modeling work completed in support of the Department of Energy Fuel Cell Bus Program, the University of Florida received a fully functional, 25 kW methanol-fueled, steam-reformed, liquid-cooled, phosphoric acid fuel cell engine designed for laboratory use. The engine was designed as a brassboard and was the building block of the 50 kW engines integrated into the three fuel cell buses. The brassboard engine is unique in that it was designed for laboratory use, thus allowing

unusual access to the engine and electronics. The goal of this research was to begin development of the basic understanding of transportation fuel cell engine behavior, primarily in the areas of efficiency and emissions.

The net overall engine efficiency ranged from 13.5% at 6.5 kW stack power output to 32% at 20 kW stack power output. These values are well below many published values for efficiency. One reason for the low efficiency is all parasitic power losses were accounted for. Also, all flows of methanol were monitored. The engine has four methanol pumps, one pump for the primary fuel/water mixture and three ancillary pumps. The results of testing showed that at low power outputs, the ancillary flows were up to 75% of the primary fuel flow. Component interaction, control strategy limitations, etc. were investigated and the associated efficiency losses were documented to begin to develop an understanding of fuel cell engine performance

Emission testing showed that carbon monoxide (CO) was the primary regulated emission. At 6.5 kW stack power output, the CO levels were approximately 30 grams per hour, while at 20 kW the CO level was <0.2 grams per hour. The high levels and sources of CO at low stack power are established.

CHAPTER 1 INTRODUCTION

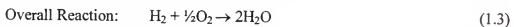
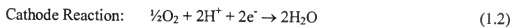
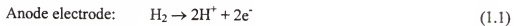
There is immense interest in increasing efficiency and reducing emissions from power producing devices. This is especially true in the transportation application, which is responsible for 70% of the nation's carbon monoxide emissions, 30% of the volatile organic compounds, and 39% of the nitrous oxides, all major components of air pollution [1]. This need for clean, efficient propulsion systems has led to significant research in the areas of new technologies.

The United States Government and the auto industry formed the Partnership for New Generation Vehicle (PNGV) Program in 1993 with the stated goal of a mid-size family car with a propulsion system capable of 80 miles per gallon. In addition, the California Air Resources Board (CARB) continued to develop ever more stringent emission standards, including a mandate for a certain number of zero-emission vehicles (ZEV), for future cars to be sold in the state of California. These requirements have led to an exhaustive analysis of possible propulsion systems for future cars. One of the most promising technologies is the fuel cell.

Fuel cells are electrochemical devices that convert the chemical energy of a fuel and oxidant directly to electrical energy. The principle is the same as a battery, but the fuel and oxidant are stored external to the fuel cell device. Therefore, limitations inherent to battery systems such as low energy density need not apply to fuel cells. The

fuel cell is not a heat engine, so it is not limited by the Carnot efficiency. Thus fuel cells do not require high temperatures to achieve high efficiencies. Theoretical efficiencies for typical fuel cells operating at standard temperature and pressure are greater than 80%. In addition, the real fuel cell may operate with low irreversibilities resulting in efficiencies that approach the ideal case.

The typical fuel cell operates by consuming hydrogen at the anode electrode and oxygen at the cathode electrode. The hydrogen molecule is absorbed to the platinum anode electrode and stripped of electrons, with the stripped electrons travelling through an external circuit and the hydronium ions (H^+) migrating through the electrolyte to the cathode electrode. Oxygen is absorbed on the platinum catalyst of the cathode electrode and reduced, and with the electrolyte ion transfer [H^+ , $(OH)^-$, etc.] and the external electron transfer, forms water. Fuel cells are typically classified by their electrolyte type, which alters the reaction mechanism. The electrode reaction equations for an acid electrolyte fuel cell are shown below:



Hydrogen is the fuel of choice because of its high electrochemical reactivity and simple reaction scheme with minimal side reactions.

If hydrogen and oxygen are available, electricity can be produced with only water as the byproduct. Fuel cell systems are not limited to hydrogen as the only primary fuel and may utilize air as the oxidizer. Many fuels, including many hydrocarbons, can be converted or “reformed” into a hydrogen-rich gas. This potential

allows the fuel cell system designer numerous choices, from utilizing pure hydrogen or methanol or more conventional fuels such as gasoline and diesel.

Traditionally, fuel cells have been bulky, heavy, and costly relative to their power output which has restrained their usefulness to a few niche markets. Hydrogen-oxygen fuel cells have provided the electrical energy requirements (as well as water) for all manned NASA space missions. In contrast, International Fuel Cells has developed a commercially-available 200 kW phosphoric acid fuel cell system which utilizes natural gas (or other hydrocarbon fuels) and untreated air and provides the user electricity and hot water.

In 1986, Los Alamos National Laboratory reported that fuel cell technology had progressed to a point that it was feasible to power a transit bus with a fuel cell/battery hybrid arrangement [2]. As a result, the Department of Energy (DOE), Department of Transportation (DOT), and the South Coast Air Quality Management District began a program to develop a phosphoric acid fuel cell (PAFC)/battery hybrid transit bus. Simultaneously, towards the end of the 1980's, significant progress was made in the performance of polymer electrolyte membrane (PEM) fuel cells [3]. PEM fuel cells had the advantage over PAFC of lower operating temperature, smaller weight, lower volume, absence of a liquid corrosive electrolyte and simple stack design. It was now believed to be possible to fit a PEM fuel cell system into a light-duty vehicle. The projected costs of the fuel cell systems also dropped significantly as research led to reducing the platinum catalyst loading on the electrodes to less than 1% of previous levels.

Interest in fuel cell technology grew rapidly during the 1990's in many sectors - government, industry, and university. The Department of Transportation began developing their second-generation fuel cell transit bus. Major auto producers began investing large sums of money in existing fuel cell companies (e.g., Daimler-Benz and Ford) or began programs to develop their own fuel cell technology (e.g., General Motors and Toyota). Numerous reports and journal articles were published describing the opportunity for high efficiencies, low emissions, and fuel flexibility and the resulting benefits to society.

A major problem was (and is) that there were (and are) only a very few fully operational, liquid-fueled fuel cell systems. As a result, there is a lack of fundamental understanding of how the major subsystems interact and the important factors involved in optimizing the performance. This is evidenced by the fact that most of the systems built have performed well below expectations in the areas of efficiency, emissions, and life. Clearly, many of these deficiencies are associated with poor thermal integration and the lack of overall system understanding.

As part of the DOE/DOT fuel cell bus program, the University of Florida (UF) developed computer models of two fuel cell systems and helped design the vehicle powertrain. As part of the program, two contractors built and demonstrated ½ scale (25 kW) "brassboard" engines. After the first phase of the project was complete, both of the brassboards including a 25 kW, methanol-fueled, liquid-cooled phosphoric acid complete laboratory system were transferred to UF. This system has involved into a valuable, unique research tool. The system is complete, including all the components required to convert liquid methanol to controlled, direct current electricity. It was

designed for the laboratory research, thus giving relatively easy access to all components, flow lines, control signals, etc.

A goal of the present research was to use the 25 kW fuel cell system to begin to develop a more fundamental understanding of a complete fuel cell system. As a result, various system efficiency curves have been developed and the causes of efficiency losses have been documented. The interaction among components, including system limitations associated with an integrated system, have been explored. The control strategy and its limitations have been investigated. And finally the levels of and sources of emissions have been concluded.

CHAPTER 2 LITERATURE REVIEW

Introduction

There is enormous interest in fuel cell technology. The potential for clean, efficient power, particularly in the transportation application, has resulted in extensive numbers of publications on various aspects of fuel cell technology. A problem, however, is that there is very little available hardware and actual data on which to base the publications. The result is conflicting and often misleading information on the performance characteristics of fuel cell “engines”. This literature review considers and interprets some of the major publications, especially those pertaining to fuel cell engines designed for the transportation application, of particular interest are those in the areas of modeling and overall engine performance.

Fuel cell systems or “engines” (transportation nomenclature) consist of many subsystems including the stack, air/fuel delivery subsystems, and the power conditioning system. The stack is the subsystem where the electrical power is generated through the electrochemical combination of fuel and oxidant. There are a variety of different types of fuel cell stacks, but the two most mentioned in the transportation application are phosphoric acid (PAFC) and polymer-electrolyte-membrane (PEM). The fuel that is typically consumed by the stack is hydrogen gas because of its high

electrochemical reactivity and simple reaction scheme. Other possible anode fuels include carbon monoxide and methanol. The fuel delivery subsystem consists of

components required to deliver the appropriate form of the fuel to the stack. A variety of fuels can be converted into a hydrogen rich gas through a reformation process. The power conditioning includes the components required to convert the variable fuel cell stack DC power into an acceptable power. Power conditioning is an important part of the fuel cell system, but outside the scope of this study which is devoted to the fuel and air to DC power processes.

Fuel Delivery System

Typical fuel cell stacks utilize hydrogen gas as fuel for the anode electrode. Thus fuel cell systems that utilize stored on-board pure hydrogen have the potential to be simple and efficient, especially for the transportation application. The difficulties and challenges for the fuel cell system designer in utilizing on-board pure hydrogen storage include the following:

- storing enough fuel in a low-weight, low-volume, and low-cost storage system
- infrastructure for refueling
- cost of hydrogen delivered to the vehicle
- possible safety problems

Commercial hydrogen gas is currently produced through conversion of natural gas (methane). It may also be produced from virtually any liquid hydrocarbon fuel, therefore the question for the transportation fuel cell engine designer is whether to produce hydrogen (steam reformer, autothermal reformer) from on-board liquid hydrocarbons or to produce the hydrogen gas off-board and store pure hydrogen on-board.

Hydrogen Fuel

Hydrogen storage

A safe, compact, lightweight, low cost on-board means of storage of hydrogen fuel would significantly enhance the commercial viability of fuel cell powered vehicles [4, 5]. Numerous on-board hydrogen storage systems have been proposed including the following [4]:

- compressed hydrogen gas (3000-15000 psi)
- low or ambient pressure liquid hydrogen
- pressurized liquid hydrogen under 5000-15000 psi (hybrid cryo-pressure system)
- rechargeable hydrides
- hydrogen cryoadsorption (carbon adsorption)
- chemical hydride.

At present, compressed hydrogen gas, liquid hydrogen, and hybrid cryo-pressure system are the most likely candidates for near-term vehicular hydrogen storage. Table 2-1 summarizes some of the more important parameters concerning hydrogen on-board storage [4]: A stored hydrogen weight of 15 pounds is required to deliver a vehicle range of approximately 340 miles.

Cryo-liquid hydrogen storage has the best weight percentage, smallest volume, and lowest tank storage cost. However, other problems exist. Storage is limited to a maximum of 2 days without venting or boil-off to reduce the vapor pressure [6]. Boil-off rates of 1-2% a day are achievable, but may be higher, thus lowering system efficiency [5, 7]. Significant quantities of energy are required to liquify hydrogen, from

30-50% of the higher heating value [7, 8]. In addition, energy must be added to heat the hydrogen before it enters the fuel cell stack. Cryo-pressure liquid hydrogen, liquid hydrogen under 5000 psia pressure, does not have as favorable characteristics as low pressure liquid hydrogen, but boil-off of hydrogen can be prevented until the vapor pressure reaches 5000 psia and the required heat energy input is less. In addition, its characteristics are significantly better than pressurized gas. Pressurized gas suffers problems associated with the volume of the system as well as low weight percentage of hydrogen.

Table 2.1: Important design parameters of various hydrogen storage methods for a passenger car with 340 mile range.

Type of Storage	Weight Percentage (usable H ₂ weight/total fueled system weight)	Volume of Complete (15 lb. stored H ₂) System (ft ³)	Projected Cost (15 lb. of stored H ₂ with production quantity > 1 million units/year)
Cryo-liquid	16.1%	7.7	\$400
Cryo-pressure liquid	10.1%	8.7	\$600
5000 psi gas	6.7%	12.3	\$1000
5000 psi cryoadsorption	4.8%	7.8	> \$1000
Rechargeable hydride	3.0% (at best)	7.7	\$2000

Source: [4]

For comparison, Table 2-2 presents the design goals for on-board hydrogen storage for a full-size fuel cell powered vehicle required to achieve a driving range of 380 miles with a fuel economy of 80 miles per gallon gasoline equivalent [5]:

Cryo-liquid hydrogen best meets the design goals. Pressurized gas systems fall short, especially in the area of system volume. Daimler-Chrysler recently introduced a

NeCar IV which is fueled by liquid-hydrogen, although other designs of the NeCar IV utilize steam reformed methanol.

Table 2.2: Design goals for on-board storage of hydrogen for a fuel cell powered full-size automobile with 80 miles per gallon gasoline equivalent and 380 mile range.

Storage Type	H ₂ Weight (lb.)	Total weight (lb.)	Total Volume	Total Cost	Life (miles)	Refuel Time (min)
5000 psi gas	12.5	217	<9 ft ³	\$300	100,000	5
Cryo-liquid	12.5	100	<6 ft ³	\$300	100,000	5

Source: [5]

Hydrogen refueling

The goal is to refuel a fuel cell vehicle in 5 minutes, which is on the same magnitude as gasoline [5]. Critical problems, however, exist with refueling either liquid hydrogen or gaseous hydrogen. Quick refueling of gaseous hydrogen results in significant increases in gas temperature. The Joule-Thompson coefficient for hydrogen gas near ambient conditions is negative, resulting in an increase in temperature as hydrogen undergoes a throttling process [9]. Analyses have shown a 270 °F increase in gas temperature in a 5 minute, 5000 psia refueling process [5]. As the stored gas temperature cools, the tank pressure drops thus resulting in lower mass storage of hydrogen. One method to eliminate the temperature is to refrigerate the hydrogen gas before transferring the gas into the tank, although the energy input is prohibitive. Another possible solution is to use a liquid hydrogen supply system, allowing the liquid to boil as it enters the storage tank. This is the method used by Chicago Transit Authority to refuel their three Ballard fuel cell buses. A description of the refueling

[10]. There are significant problems and safety issues associated with refueling of liquid hydrogen including [5, 6]:

- air condensate/freezing
- approximately 10% vaporization
- metering/fill detection

Fill detection is difficult because the liquid-vapor boundary is not distinct.

Cost and infrastructure

An analysis of the required hydrogen infrastructure and resulting fuel cost is beyond the scope of this literature review. It is important, however, to note that the virtually 100% of commercial hydrogen is currently produced from natural gas feedstock. This is the same feedstock that produces the majority of the methanol, and a proper comparison between the two fuels (or any fuels) requires an analysis beginning at the feedstock fuel.

A report by Ford Motor Company presented to the Department of Energy provides a detailed breakdown of various cost estimates for producing hydrogen, from the utilization of large steam methane reforming plants to on-site electrolyzers [11]. The cost goal for delivered hydrogen was \$3.12/kg based on the on the premise of the fuel operating cost per mile remaining the same as an internal combustion vehicle [11]. The delivered hydrogen cost goal is affected by the following:

- fuel cell engine efficiency
- taxation policies
- feedstock fuel and electrical costs
- drive cycle.

The projected costs varied significantly, even for similar processes. Costs projections ranged from \$2.29/kg to \$10.94/kg of delivered hydrogen for different methane steam reformer designs [11]. As expected costs were typically reduced for increased number of fuel cell vehicles supported. Ford Motor Company concluded that compressed hydrogen (5000 psia) could be delivered to fuel cell vehicles at a cost competitive with gasoline per mile driven.

A report from Ogden of Princeton University compares hydrogen, methanol, and gasoline on vehicle design, costs, and infrastructure development [12]. The prices of the fuel vary widely depending on factors such as off-peak electricity prices, size of plant, distribution network, etc. but were similar to the results from Ford. These are two of many reports detailing the hydrogen cost and infrastructure needs.

Other Fuels

Fuel cell designers are not limited to pure hydrogen as the only possible fuel choice. Fuel cell systems can utilize a variety of fuels that are reformed or cracked into a hydrogen-rich gas. These fuels include conventional fuels (gasoline or diesel) and alternative fuels, both hydrocarbon fuels (natural gas, methanol, and ethanol) and non-hydrocarbon fuels (ammonia). Almost any fuel with a significant hydrogen content may be utilized.

There are a number of critical issues to consider when selecting a fuel, including the following [13]:

- safety considerations
- storage considerations
- availability in quantity

- new infrastructure requirements and per unit of delivered hydrogen
- cost per unit of available energy
- environmental considerations (production, delivery, and consumption)
- compatibility with fuel cell systems- hydrogen production

Safety considerations and storage considerations are often interconnected. Fuels that are stored as liquids at atmospheric temperature and pressure have inherent safety advantages. Safety concerns include the following:

- storage temperature and pressure
- toxic and corrosive properties
- flammability limits
- ignition energy
- auto-ignition temperatures

Storage concerns include but are not limited to fuel energy per unit volume, fuel energy per unit mass, and storage energy requirements. Storage energy requirements include thermal conditioning (heating or cooling) and compression energy (gas storage). Table 2-3 lists lower heating value per unit volume and mass for selected candidate fuels [13].

Table 2-3. Selected potential fuels for fuel cell systems.

Fuel Type	Lower Heating Value/Volume (kcal/l)	Lower Heating Value/Mass (kcal/kg)
Gasoline (liquid, 25 °C)	7600	10556
Ethanol (liquid, 25 °C)	5089	6442
Methanol (liquid, 25 °C)	3800	4798
Methane (liquid, -161.5 °C)	8594	11936
Methane (gas, 5000 psi)	2745	11936
Hydrogen (liquid, -252 °C)	2027	28628
Hydrogen (gas, 5000 psi)	658	28628

Source: [13]

The liquid fuels compare favorably in energy per unit volume and have adequate energy per unit mass. In addition gasoline, ethanol, and methanol are easily stored in simple fuel tanks so the fuel volume is approximately the storage volume. Hydrogen has a significant energy per unit mass, but this is offset by the low energy per unit volume plus the additional volume of the storage container (insulation, vessel walls, etc.).

Table 2-3 is incomplete since all of the fuels (except hydrogen) require water to execute the reforming process. The volume and weight associated with the water is not wasted, however, as much of the water is converted to hydrogen. Table 2-4 depicts a more complete picture by including the weight and volume of the required water and comparing the lower heating value of the total hydrogen produced from an ideal reforming process on a weight and mass basis.

The availability of a candidate fuel is an important consideration when making a fuel choice. In order for fuel cell systems or engines to enter the transportation market, the fuel chosen must be available in significant quantities. Gasoline and diesel fuel availability and existing infrastructure are the primary reasons that a substantial effort is underway to develop gasoline-fueled and diesel-fueled fuel cell engines [14, 15]. Table 2-5 details the availability of selected alternative fuels to garner a 10% share of the transportation sector [13]. As shown in Table 2-5, only natural gas is available in sufficient quantities to allow for a 10% market share. However, as with all the other fuels, most of the available fuel energy is already utilized in other sectors of society such as hot water heating, cooking, etc. Therefore, to make an impact on the transportation sector, significant investment in production capacity and other infrastructure would be required.

Table 2-4: Net hydrogen energy per unit weight and volume of selected fuels plus water required for the ideal reforming process.

Fuel Type	Fuel + H ₂ O (kg mix)/(kg fuel)	Net H ₂ Energy/Vol. kcal/(liter of mix)	Net H ₂ Energy/Mass kcal/(kg mix)
Ethanol (liquid, 25 °C)	2.15	3082	3463
Methanol (liquid, 25 °C)	1.56	3250	3233
Methane (liquid, -161.5 °C)	3.25	3963	4437
Methane (gas, 5000 psi)	3.25	2186	4437
Hydrogen (liquid, -252 °C)	1.0	2027	28628
Hydrogen (gas, 5000 psi)	1.0	658	28628

Source: [13]

Table 2-5: Availability of selected fuels to garner a 10% share of the transportation energy sector.

Fuel Type	Quantity Required for 10% of Transportation Market	Approximate Current Production Capacity	Production as a Percent of Requirement
Natural gas	$320 \times 10^9 \text{ ft}^3$	$17.5 \times 10^{12} \text{ ft}^3$	5500%
Hydrogen	$250 \times 10^6 \text{ bbl}$	$5 \times 10^6 \text{ bbl}$	2%
Methanol	$140 \times 10^6 \text{ bbl}$	$36 \times 10^6 \text{ bbl}$	26%
Ethanol	$100 \times 10^6 \text{ bbl}$	$20 \times 10^6 \text{ bbl}$	20%

Source:[13]

Reforming Process

Reforming is a generic term used to describe the reaction process of converting a fuel into a hydrogen-rich gas stream. The goals of the reforming process are to maximize the hydrogen yield, minimize the required energy input, and to minimize contaminants such as carbon monoxide.

A comprehensive review of the reforming process was completed by A.D. Little [8] in a report to the U.S. Department of Energy. The most promising processes for reforming hydrocarbons and alcohols are the following :

- Catalytic steam reforming
- Non-catalytic partial oxidation (POX)
- Catalytic autothermal reforming (ATR)

Steam reforming

Steam reforming of hydrocarbons into hydrogen and synthetic gas is an established chemical process in many industries. Steam reforming is an endothermic reaction where the fuel is reacted with steam in the presence of a suitable catalyst to produce a hydrogen rich gas [8]. The initial fuel decomposition reaction is followed by a water gas shift reaction where steam and carbon monoxide are reacted to form hydrogen and carbon dioxide. The major reactions for steam reforming of methanol, methane, and ethanol are listed in Table 2-6 [8].

Table 2-6: Steam reforming reactions for methane, methanol, and ethanol.

Type of Fuel	Type of Reaction	Reaction	ΔH_{298} KJ/mole
Methane	Decomposition	$\text{CH}_4 + \text{H}_2\text{O} \leftrightarrow \text{CO} + 3\text{H}_2$	+ 206.14
	Water Gas Shift	$\text{CO} + \text{H}_2\text{O} \leftrightarrow \text{H}_2 + \text{CO}_2$	- 41.17
	Overall (Ideal)	$\text{CH}_4 + 2\text{H}_2\text{O} \leftrightarrow 4\text{H}_2 + \text{CO}_2$	+ 164.97
Methanol	Decomposition	$\text{CH}_3\text{OH} \leftrightarrow 2\text{H}_2 + \text{CO}$	+ 90.13
	Water Gas Shift	$\text{CO} + \text{H}_2\text{O} \leftrightarrow \text{H}_2 + \text{CO}_2$	- 41.17
	Overall (Ideal)	$\text{CH}_3\text{OH} + \text{H}_2\text{O} \leftrightarrow 3\text{H}_2 + \text{CO}_2$	+ 48.96
Ethanol	Decomposition	$\text{C}_2\text{H}_5\text{OH} \leftrightarrow \text{CO} + \text{H}_2 + \text{CH}_4$	+ 49.05
	Methane	$\text{CH}_4 + \text{H}_2\text{O} \leftrightarrow \text{CO} + 3\text{H}_2$	+ 206.14
	Water Gas Shift	$\text{CO} + \text{H}_2\text{O} \leftrightarrow \text{H}_2 + \text{CO}_2$	- 41.17
	Overall (Ideal)	$\text{C}_2\text{H}_5\text{OH} + \text{H}_2\text{O} \leftrightarrow 6\text{H}_2 + 2\text{CO}_2$	+ 172.85

Source: [8]

Methanol steam reforming requires the least energy input (48.96 KJ/mole).

Methane and ethanol steam reforming occurs at catalyst bed temperatures of 600-1000 °C, while methanol can be steam reformed as low as 250 °C. At higher temperatures, the carbon monoxide (CO) levels in the product stream can be as high as 10%. To

reduce CO levels, the reaction products are often passed through a high temperature shift reactor (HTS) operating at 300-450 °C and then through a low-temperature shift reactor (LTS) operating at 150-250 °C. The shift reactors minimize CO by the water gas shift reaction which favors hydrogen and carbon dioxide at low temperatures. For stationary systems, steam reforming is typically used to maximize the hydrogen yield.

Partial oxidation reforming (POX)

Partial oxidation reforming is a non-catalytic reaction where the required heat input for the decomposition reaction (Table 2-7) is supplied by oxidizing a fraction of the feedstock fuel. The extent of the reaction is controlled by the amount of oxygen added to the fuel stream. Approximately 20% of the heating value of the fuel is used to provide the reaction heat input, and the extent of the combustion reaction is partially dictated by the need to suppress carbon formation [16]. The primary reaction is the following [16]:



Partial oxidation has typically been used to reform heavy hydrocarbons or coal, fuel feedstocks that are difficult to steam reform. Partial oxidation typically occurs at 1100-1500 °C, and can utilize pure oxygen or air if nitrogen dilution of the product gas is not a concern. The major reactions for partial oxidation of methane, methanol, and ethanol are listed in Table 2-7 [8].

Methanol has the simplest reaction scheme, and theoretically does not rely on the water gas shift reaction to reduce the carbon monoxide. In practice, however, incomplete and side reactions cause high levels CO, and thus the product stream is passed through shift reactors to remove CO.

Table 2-7: Partial oxidation reforming reactions for methane, methanol, and ethanol.

Fuel Type	Type of Reaction	Reaction	ΔH_{298} KJ/mole
Methane	Combustion	$\text{CH}_4 + \frac{1}{2}\text{O}_2 \leftrightarrow \text{CO} + 2\text{H}_2$	+ -35.68
	Combustion	$\text{CH}_4 + \text{O}_2 \leftrightarrow \text{CO}_2 + 2\text{H}_2$	-318.67
	Decomposition	$\text{CH}_4 + 2\text{H}_2\text{O} \leftrightarrow \text{CO}_2 + 4\text{H}_2$	164.97
	Water Gas Shift	$\text{CO} + \text{H}_2\text{O} \leftrightarrow \text{H}_2 + \text{CO}$	<u>-41.17</u>
	Overall (Ideal)	$\text{CH}_4 + \frac{1}{2}\text{O}_2 + 2\text{H}_2\text{O} \leftrightarrow 3\text{H}_2 + \text{CO}_2$	+ 76.88
Methanol	Combustion	$\text{CH}_3\text{OH} + \frac{1}{2}\text{O}_2 \leftrightarrow 2\text{H}_2 + \text{CO}_2$	- 192.86
	Decomposition	$\text{CH}_3\text{OH} + \text{H}_2\text{O} \leftrightarrow 3\text{H}_2 + \text{CO}_2$	<u>+ 48.96</u>
	Overall (Ideal)	$\text{CH}_3\text{OH} + \frac{1}{2}\text{H}_2\text{O} + \frac{1}{2}\text{O}_2 \leftrightarrow 2\frac{1}{2}\text{H}_2 + \text{CO}_2$	-71.95
Ethanol	Combustion	$\text{C}_2\text{H}_5\text{OH} + \frac{1}{2}\text{O}_2 \leftrightarrow 2\text{CO} + 3\text{H}_2$	+ 13.37
	Combustion	$\text{C}_2\text{H}_5\text{OH} + 1\frac{1}{2}\text{O}_2 \leftrightarrow 2\text{CO}_2 + 3\text{H}_2$	- 552.61
	Decomposition	$\text{C}_2\text{H}_5\text{OH} + 3\text{H}_2\text{O} \leftrightarrow 2\text{CO}_2 + 6\text{H}_2 + 2\text{CO} + 2\text{H}_2\text{O}$	+ 172.85
	Water Gas Shift	$\leftrightarrow 2\text{H}_2 + 2\text{CO}$	
	Overall (Ideal)	$\text{C}_2\text{H}_5\text{OH} + 2/3\text{O}_2 + 2\frac{1}{2}\text{H}_2\text{O} \leftrightarrow 14/3\text{H}_2 + 2\text{CO}_2$	<u>82.34</u> 149.58

Source: [8]

The quantity of hydrogen gas produced per mole of feedstock fuel is less for partial oxidation than steam reforming for all three fuels, because a fraction of the fuel is consumed through combustion to provide the heat required for the overall reaction.

The main advantage of partial oxidation reforming in transportation applications is the fast startup times, since zero time is required to raise the temperature of a catalyst mass.

Autothermal reforming (ATR)

Autothermal reforming is a hybrid technology that combines the catalytic aspect of steam reforming with the oxidation feature of partial oxidation [8]. Two catalysts are often used, one to promote combustion and the second to promote the steam reforming reactions. The temperature of operation falls below the POX reactors and above the

steam reformer reactors. The main reactions are similar to the POX scheme, and the product stream is typically passed through a two-stage water gas shift reactor. Being a hybrid technology, autothermal reforming has the advantages and disadvantages of both steam reforming and partial oxidation. The main problem with autothermal reforming is that the startup time is not as fast as POX (due to the catalyst bed) and the hydrogen yield is not as high as steam reforming (due to partial combustion of the feedstock fuel).

Preferential oxidation (PROX)

Polymer electrolyte membrane (PEM) fuel cell stacks operate best with anode gas streams with less than 50 ppm carbon monoxide. Carbon monoxide has a higher chemical affinity for the platinum catalyst than hydrogen at fuel cell stack operating temperatures of 80-100 °C and thus occupy active sites, effectively “poisoning” the catalytic surface. For all the above reforming concepts, even with a two-stage shift reactor, the CO levels are typically well above 100 ppm. To further reduce the CO levels, a preferential oxidation reactor (PROX) is used to perform selective catalytic oxidation of the CO but not the hydrogen [8 and others].

Phosphoric acid fuel cell stacks (PAFC) operate at 160-200 °C and can tolerate 1-2% CO levels in the anode stream without significant loss in performance. Because of this higher CO tolerance, it is generally not necessary to utilize a PROX reactor and it is not desirable with a PAFC because there is some inevitable oxidation of hydrogen in a PROX reactor, thus lowering the effective conversion efficiency.

Methanol Steam Reforming

Methanol steam reforming is the most common type of reforming of a liquid fuel for fuel cell systems. Methanol has the following characteristics that make it attractive for the transportation fuel cell system:

- liquid fuel that is easily stored
- can be manufactured from numerous sources, including natural gas, coal, and biomass
- easily converted to a hydrogen rich gas at low temperatures [16]
- single carbon molecule minimizes the potential for carbon formation from carbon-to-carbon bond cracking reactions [16]

Steam reforming is of significant interest because of the high hydrogen yield, possible simple reaction scheme, and well-developed catalyst technology. Because of these favorable characteristics, abundant research has been completed on the thermodynamics, kinetics, and design considerations of methanol steam reforming.

Thermodynamics

Numerous references have completed comprehensive reviews of the thermodynamics of methanol steam reforming. By studying the reaction thermodynamics, the conditions that favor increased methanol conversion, increased hydrogen production, and minimized required heat input can be determined. Actual reformation processes can be compared to the ideal case (chemical equilibrium) to determine the effectiveness of the steam reformer design.

A thermodynamic review of methanol steam reforming was completed by Amphlett [17]. In this study, the thermodynamic equilibria was investigated for the

catalytic steam reformation of methanol for the following conditions: range of pressure of 101-3040 kPa; temperature range of 400-700 K; and for feed ratios (also known as water-to-methanol ratio or steam-to-carbon ratio) of 1.50-0.67. Four models for possible reaction products were considered and the equilibrium gas composition for each model was calculated. The required energy input was not considered.

The four models of reforming product gas composition were constructed based on the following constituents: H_2 , CO_2 , CO , H_2O , CH_3OH , CH_4 , and C . The simplest model consisted of the primary reformation products H_2 , CO , and CO_2 as well as H_2O and unreacted CH_3OH . Models 2 and 3 included Model 1 constituents plus CH_4 and C respectively. Model 4 consisted of Model 1 constituents plus both CH_4 and CO . Further studies have shown that Model 1 reasonably depicts the product gas composition [18, 19].

The product gas constituents for each model were derived from a series of equations involving species balances and equilibrium reaction constants. For example, Model 2 equations included the following reactions:



The results of the equilibrium analysis showed that methanol conversion is nearly 100% for temperatures greater than 600 °K for all pressures, and nearly 100% at low pressures for temperatures less than 600 °K and feed ratios of 1.5. This indicates that a well-

designed reformer with the proper space gas velocity should result in nearly complete conversion of methanol.

Further results show that hydrogen production is maximized at low pressures, temperatures between 400 and 500 °K, and excess H₂O. Low pressures result in greater percentage of methanol conversion. Low temperatures and excess water favor a shift towards H₂ production in the water-gas shift reaction. The conditions to maximize hydrogen production are 230 °C, pressure of 101 kPa, and a steam-to-carbon ration greater than unity [23].

Models 2-4 show CH₄ or C formation results in decreased H₂ production. Carbon is minimized if excess water and temperatures above 500 °K are employed. Methane can be formed when CO₂ and H₂O are present, and therefore selective catalysts are required that inhibit formation of methane. Other studies have verified similar results, including the conclusion that Model 1 from Amphlett is a reasonable model for methanol steam reformation [8, 16, 21, 24-26].

Kinetics

Knowledge of the reaction mechanism and reaction rates is required to properly design a methanol steam reformer. Thermodynamics can provide the equilibrium gas compositions and theoretical heat input, but a kinetic study is required to determine important reformer design parameters such as gas space velocity and required catalyst loadings. Amphlett reported that the methanol steam reforming process is initially a methanol decomposition reaction followed by a water gas shift reaction [18-20] and this is the same mechanism reported by A.D. Little [8]. Table 2-8 lists the reactions for this mechanism. The steam reforming reaction kinetics were studied utilizing small-scale

reformer tubes and CuO-ZnO low temperature catalyst [18-20]. Initial results of both studies show that Model 1 by Amphlett [17] best depicted the product gas constituents [23]. The results of the testing showed CO concentrations well below equilibrium values. The explanation provided for the low CO levels was that the short length of the reformer tubes resulted in a low methanol conversion rate (inadequate residence times), resulting in excess water in the product stream that shifts the CO to CO₂. The hydrogen and carbon dioxide concentrations in the product stream were very close to the equilibrium values predicted by Model 1.

Table 2-8: Decomposition reaction scheme for methanol steam reforming.

Type of Reaction	Reaction	ΔH_{298} KJ/mole
Reforming	$\text{CH}_3\text{OH} \leftrightarrow 2\text{H}_2 + \text{CO}$	+ 90.13
Water Gas Shift	$\text{CO} + \text{H}_2\text{O} \leftrightarrow \text{H}_2 + \text{CO}_2$	- 41.17
Overall (Ideal)	$\text{CH}_3\text{OH} + \text{H}_2\text{O} \leftrightarrow 3\text{H}_2 + \text{CO}_2$	+ 48.96

Source: [21]

Further studies have shown the possibility of a different reaction mechanism. Within this alternative mechanism, methanol reduces a site and water oxidizes the site back to the original condition [27]. The reactions are shown in Table 2-9.

Table 2-9: Oxidation-Reduction reaction scheme for methanol steam reforming.

Type of Reaction	Reaction
Site reduction	$\text{CH}_3\text{OH} + \langle \text{S-O} \rangle \leftrightarrow 2\text{H}_2 + \text{CO}_2 + \langle \text{S} \rangle$
Site oxidation	$\text{H}_2\text{O} + \langle \text{S} \rangle \leftrightarrow \text{H}_2 + \langle \text{S-O} \rangle$
Water-gas shift	$\text{CO} + \text{H}_2\text{O} \leftrightarrow \text{H}_2 + \text{CO}_2$

Source: [27]

Other papers have also presented this mechanism as an alternative [21, 25]. In this mechanism, carbon dioxide is formed directly by the site reduction reaction. Carbon monoxide is then formed through the water gas shift reaction. The available data

appears to correlate the reduction-oxidation mechanism as many papers show carbon monoxide levels below equilibrium levels [20, 25]. If the reduction-oxidation mechanism is correct, the task of removing CO from the product stream is easier than for the decomposition scheme since the highest levels of CO are those of equilibrium while for the decomposition scheme the lowest levels of CO are those of equilibrium.

Additional studies have attempted to analyze the important reactions other than the methanol decomposition reaction [20]. This is accomplished by utilizing “gas runs”; for example using a feed gas composition of only H_2 and CO_2 and studying the reverse water gas shift reaction. Tests results from the gas runs verified the simple reaction mechanism [18, 19] over certain temperature ranges ($<180\text{ }^{\circ}C$) and further work is required for temperatures above $180\text{ }^{\circ}C$.

Other studies have investigated the important design considerations for methanol steam reformers [28-30]. Kumar compares methanol steam reforming to methanol partial oxidation in the areas of hydrogen production, product gas composition, energy conversion, and dynamic response. Dusterwald studies the effects on the rate of catalyst deactivation [28]. This is important as transportation steam reformers are made smaller and lighter (less catalyst mass) than stationary systems with similar flow rates. Deactivation was shown to be a function of utilization and shutdown procedures [28]. Ohl presented a model that determines the fundamental factors in the design of a fast-responding methanol steam reformer. Calculations showed that a well-designed steam reformer could obtain a transient response time on the order of 15-20 seconds [29]. The factors most affecting the transient response time include the convective heat transfer coefficient, catalyst thermal capacity, surface area, and inner

wall temperature [29]. This confirms that the response time of the steam reformer is heat transfer limited.

Fuel Cell Stack Models

Introduction

As stated earlier, interest in fuel cells systems, engines, sub-components, etc. is considerably greater than available research hardware. As such, much of the research is simply theoretical in nature or based on small-scale devices. This is especially true of fuel cell stack modeling. The interest in PEM or PAFC systems operating on a liquid fuel feedstock is strong due to their potential for transportation applications. However only a handful of complete systems exist and most remain with the original manufacture. Therefore, many models utilize small (1" x 1") single cells operating on premixed gas (simulated reformat) to provide data to calibrate and verify stack models. This small scale testing limits the scope and accuracy of available models and simulations.

Background

A fuel cell stack consists of a series of individual cells connected together. Each cell consists of a porous anode electrode, a porous cathode electrode and electrolyte matrix. The fuel, typically hydrogen, is electrochemically oxidized at the anode electrode. The oxidant, typically oxygen (either pure oxygen or oxygen in air), is electrochemically reduced at the cathode electrode. The ion transfer (hydrogen ions for phosphoric acid and PEM cells) occurs across the electrolyte. The electron transfer occurs through an external circuit resulting in electrical current. Typical electrochemical reactions for fuel cells are shown in Table 2-10 [31].

Since each cell produces nominally 0.6-0.7 volts, the cells are normally connected in series to produce a working stack voltage. The area of each cell, an indication of sites available for the electrochemical reaction, determines the current limit for the cell or stack. By adjusting the cell area and the number of cells, the desired output voltage, current, and power is obtained.

Table 2-10: Typical electrochemical reactions in fuel cells.

Fuel Cell Type	Anode Reaction	Cathode Reaction
Proton Exchange	$\text{H}_2 \rightarrow 2\text{H}^+ + 2\text{e}^-$	$1/2\text{O}_2 + 2\text{H}^+ + 2\text{e}^- \rightarrow \text{H}_2\text{O}$
Phosphoric Acid	$\text{H}_2 \rightarrow 2\text{H}^+ + 2\text{e}^-$	$1/2\text{O}_2 + 2\text{H}^+ + 2\text{e}^- \rightarrow \text{H}_2\text{O}$
Alkaline	$\text{H}_2 + (\text{OH})^- \rightarrow 2\text{H}_2\text{O} + 2\text{e}^-$	$1/2\text{O}_2 + \text{H}_2\text{O} + 2\text{e}^- \rightarrow 2(\text{OH})^-$
Molten Carbonate	$\text{H}_2 + \text{CO}_3^{2-} \rightarrow \text{H}_2\text{O} + \text{CO}_2 + 2\text{e}^-$	$1/2\text{O}_2 + \text{CO}_2 + 2\text{e}^- \rightarrow \text{CO}_3^{2-}$
	$\text{CO} + \text{CO}_3^{2-} \rightarrow 2\text{CO}_2 + 2\text{e}^-$	
Solid Oxide	$\text{H}_2 + \text{O}^{2-} \rightarrow \text{H}_2\text{O} + 2\text{e}^-$	$1/2\text{O}_2 + 2\text{e}^- \rightarrow \text{O}^{2-}$
	$\text{CO} + \text{O}^{2-} \rightarrow \text{CO}_2 + 2\text{e}^-$	
	$\text{CH}_4 + 4\text{O}^{2-} \rightarrow 2\text{H}_2\text{O} + \text{CO}_2 + 8\text{e}^-$	

Source: [31]

In addition to power producing cells, the fuel cell stack contains the following other components:

- gas manifolding
- cooling plates
- electrical connects
- insulation
- end plates

The gas manifolding system delivers the flow of fuel and oxidant to each individual cell. A properly designed manifolding system would deliver equal flow of fuel and oxidant to each cell to maximize performance. Cooling plates are typically placed

between every 3-5 cells to remove excess heat generated during the electrochemical reaction. The endplates are bolted together to provide compression to seal the stack. Insulation is used to maintain stack temperature and allow the stack waste heat to be used for other purposes such as liquid fuel vaporization. Finally, the overall stack voltage and current as well as individual cell voltage and current are often monitored to determine the performance of the stack.

Stack Modeling Goals

The goal of cell or stack modeling is to be able to reasonably predict the performance of the stack for a range of input parameters. The performance of the stack is typically determined by how efficiently the hydrogen and oxygen are converted into water and electricity, and the cell voltage as a function of current density indicates this. The current density, typically mA/cm², is used to normalize the curve for comparison of cells and stacks of different areas. A plot of the voltage versus the current or current density is called the polarization curve, and a typical plot is shown in Figure 2-1 [32].

The maximum electrical work (reversible) available for a fuel cell operating at constant pressure and temperature is indicated by the change in the Gibbs free energy of the electrochemical reaction [31, 33]

$$W_{el} = \Delta G = -nFE \quad (2.6)$$

where: W_{el} = electrical work

ΔG = change in Gibbs free energy

n = number of electrons

F = Faraday's constant (96,439 Coulombs/gmole electrons)

E = reversible cell voltage

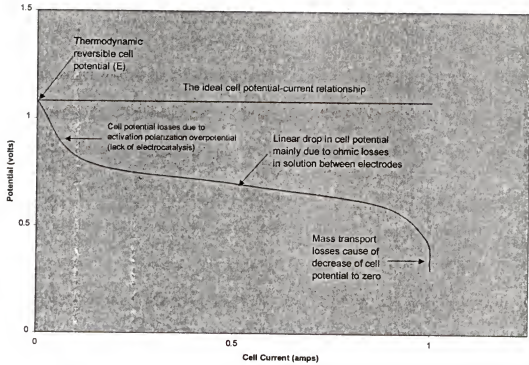


Figure 2-1: Typical fuel cell polarization curve [32].

A typical fuel cell electrochemical reaction is the following:



The reversible thermodynamic potential for the above reaction assuming ideal gas is the

Nerst equation [34]:

$$E = E^\circ + (RT/nF) \ln [\text{P}_{\text{H}_2}^* (\text{P}_{\text{O}_2}^*)^{1/2}] \quad (2.8)$$

where: E° = reversible potential at the standard state (25 °C, 1atm.)

$\text{P}_{\text{H}_2}^*, \text{P}_{\text{O}_2}^*$ = partial pressure (atm)

Typical values for the reversible cell potential for a PAFC or PEM cell range from 1.05-

1.23 V. Fuel cells producing power operate irreversibly, and therefore the primary

application of the reversible cell voltage is for comparison purposes in determining losses within the cell. Also, the reversible case is never achieved even at zero current as competing anodic side reactions play a role, resulting in the open-circuit potential being a mixed potential which is lower than the ideal case by 0.1-0.2 volts [32].

The losses within the cell have been separated into three categories: activation polarization, ohmic polarization, and mass transport/concentration polarization. Activation polarization losses are associated with sluggish kinetics. As the cell produces a current, it is driven from the equilibrium condition. Activation polarization results from losses associated with adsorption of reactant species, transfer of electrons across the double layer, and desorption of the product species. Activation losses predominate at lower current densities, and losses are caused nearly entirely from the reduction of oxygen at the cathode [35]. Ohmic losses include resistance to electrical flow and to flow of ions within the electrolyte. Concentration losses become important at high current densities because large concentration gradients are created. The concentration losses are associated with energy lost in overcoming resistance to mass transfer and manifest as heat within the cell electrolyte near the electrode [34].

Performance Parameters

The polarization curve for a given stack is not fixed, but changes with changing input parameters such as the stack temperature, contaminants (e.g., carbon monoxide), pressures, and aging. These parameters effect the position and shape of the polarization curve. Table 2-11 provides an abbreviated list of important fuel cell stack parameters [36]. Comprehensive stack models become complicated very quickly as not only are

there many parameters involved, but many parameters are localized and change within the cell structure. Examples of localized parameters include the following:

- partial pressures of the fuel and oxidant as they are consumed by the stack
- quantity of water produced within the porous cathode electrode
- temperature variations from cell to cell within a cell

Table 2-11: Abbreviated list of important parameters for the fuel cell stack.

Parameter	Description
Operating	
• Pressure	Fuel and air operating pressures of the fuel cell stack
• Temperature	Target point for the fuel cell stack operating pressure
• Humidity	The relative humidity of the air entering the stack
• Stoichiometry	The amount of excess fuel and air that is delivered to the stack. May be different for fuel and air.
Design	
Membrane-Electrode Assembly	
• Membrane	Type and thickness of material
• Catalyst	Type and amount used on each electrode
• Electrode	Material for electrode and amount and type of impregnation material
Stack	
• MEA active area	Active area of the Membrane-Electrode-assembly (MEA)
• Aspect Ratio	Ratio of the bipolar plates length-to-width ratio
• Number of cells	Number of cells in a stack
• Plate material	Construction material of the bipolar plates
• Flow configuration	Relationship of fuel entry point to the air entry point
• Gas delivery system	Means of getting the gases through the stack
• Cooling plate material	Construction material of the cooling plates
• Cooling Fluid	Fluid used to cool the stack
• Cooling plate frequency	Number of cells between the cooling plates
• Stack construction	Means of connecting the individual components

Source: [36]

Current density

The current density of a cell is not uniform. As the fuel and oxidant pass across the cell, they are consumed and their partial pressures change, thus changing the driving force for the reaction. In addition, localized parameters such as electrolyte conductivity or membrane properties also play a role. Each electrode surface is equipotential, thus areas of high current density drive down the overall efficiency of the cell. Figure 2-2 is an example of current distribution for a flat plate at a constant potential [32].

Stack temperature

The temperature throughout the stack is non-uniform. The current density, which is an indication of the local reaction rate, is also an indication of the local waste heat generated. Thus areas of high current density will have locally higher temperatures. This varying current and temperature distribution make localized modeling of the cell difficult. In addition to temperature variations within a particular cell, the average temperature of adjoining cells is different due to the positioning of the cooling plates. The cell furthest from the cooling plates will have a higher temperature as dictated by the heat removal requirements. For cooling plates every 5 cells, Fuji reported cell temperature variations of 15 °C, while models have shown 8 °C temperature difference in 4 cell stacks [32, 37]. This further complicates the performance modeling of an entire stack as well as prohibiting a simple definition for stack temperature. Figure 2-3 details the temperature variation between cells in a stack [32].

Carbon monoxide poisoning

The presence of carbon monoxide in a hydrogen rich gas stream acts as a temporary poison to electrocatalytic activity of platinum electrodes [31]. The effect of

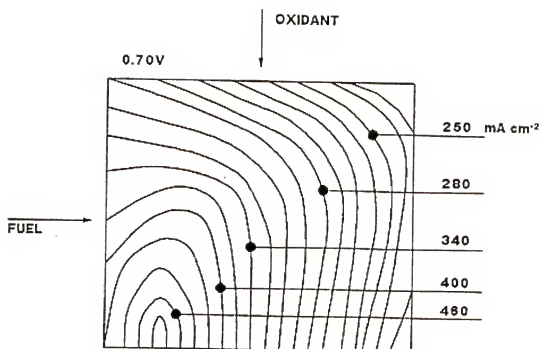


Figure 2-2: The current density distribution across a typical cell [38].

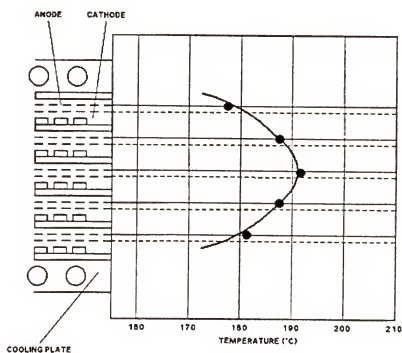


Figure 2-3: Temperature distribution across a Fuji stack with liquid coolant plates placed every five power producing cells [38].

CO poisoning is temperature related, so PAFC operating at 190 °C can tolerate 1% CO without noticeable detriment while PEM fuel cells operating at 80 °C are limited to 100 ppm [32]. Rodrigues reported on modeling efforts to predict the equilibrium cell output voltage as a function of current density and CO partial pressure [38]. The model attempted to predict the surface coverage of CO and the effect on activation overpotential (losses in cell potential due to sluggish electrochemistry). The model had limited success, in part because of the unusual shape of polarization curves of cells poisoned with even low levels (100 ppm) of CO. In a paper presented by Paffett, the effect of bleeding 2% oxygen into the CO contaminated hydrogen-rich anode fuel stream was investigated [39]. The results of single cell test showed that 2% oxygen injection in 100 ppm CO contaminated fuel stream resulted in nearly similar cell performance as the case of zero CO. In addition, a 2% air injection (0.4% oxygen), resulted in full performance with negligible loss of hydrogen through direct combination of CO with the oxygen.

Other performance factors

Other important stack performance factors include pressure and flow path configurations. The stack operating pressure has a direct effect on stack performance by determining the partial pressure of the reactants. The increase in performance of the stack must be weighed against the parasitic power costs of providing fuel and oxidant at higher pressures. The flow path configuration (co-flow, counterflow, cross flow, etc.) of fuel and oxidant can have a significant effect on stack performance. In a paper by Mitsuda, the interaction between the fuel utilization (percentage of hydrogen consumed by the cell) and the flow configuration was investigated [40]. Results showed little

correlation between cell performance and flow configuration for 80% utilization, but noticeable differences at 90% utilization.

Cell/Stack Models

Two examples of fairly comprehensive cell/stack models are presented by Springer [41] and Bernadi [35] for the PEM fuel cell. The model by Springer [41] is an isothermal, one-dimensional steady-state representation of a PEM cell which concentrates on the water transport properties that are critical to the performance of a PEM cell. The model by Bernadi is also an isothermal, one-dimensional, steady-state representation of a PEM cell. Most model "calibration" parameters and properties were obtained from general experimental data independent of specific fuel cell data. Both models required a significant number of simplifying assumptions, such as isothermal operation, which lead to errors, especially in the case of fuel cell stacks where actual temperature variations are significant. Wohr presented a dynamic model that included mass transport limitations, particularly in the humidification process [37]. The difficulty in utilizing the above models is that they require "knowledge of parameters which are not readily available, such as, transfer coefficients, humidity levels, membrane, electrode, and active catalyst layer thicknesses" [42].

To ease the problem of limited availability of data and properties, Amphlett [42-44] used a combination of mechanistic model development and empirical data to develop models for a PEM cell/stack. The first step was to develop a mechanistic model for the PEM cell that determines the characteristic dependencies of the fuel cell operation. By grouping of terms, simple algebraic equations were determined for thermodynamic equilibrium potential, activation overvoltage, ohmic resistance, and

mass transport [42]. Next, the numerical parametric equations were evaluated for each term based on experimental data.

An example of this method is presented for the cathodic activation overpotential ($\eta_{\text{act, cathodic}}$), or simply the loss in voltage associated with irreversibilities losses at the cathode electrode. The activation overvoltage can be modeled by the empirically-based Tafel expression:

$$\eta_{\text{act, cathodic}} = 2.3 (RT)/(\alpha nF) \log(i_0/i) \quad (2.9)$$

where: R = universal gas constant

T = Temperature (K)

α = transfer coefficient

n = number of equivalents in the reaction

F = Faraday's constant

i_0 = exchange current density (amps)

i = current (amps)

The exchange current density is an indicator of the electrode reaction rate, a large value means that the reaction proceeds reversibly [32]. The kinetics of hydrogen oxidation at standard state depict an exchange current density of 50 amps/ft² while the exchange current density for the oxygen reduction reaction is in the range of 10⁻³ amps/ft². The result is the magnitude of the term " $\log(i_0/i)$ " in equation 2.9 is much greater for the oxygen reduction reaction and results in greater the potential losses. The exchange current density can be expressed as the following [42]:

$$i_0 = nFAK_0 [\exp(-\Delta F_E/RT)(C_{O_2}^*)^{(1-\alpha)}(C_{H_2}^*)^{(1-\alpha)}(C_{H_2O}^*)^{(\alpha)}] \quad (2.10)$$

where: A = cross-sectional surface area

K_0 = intrinsic rate constant

ΔF_E = standard free energy of activation for the reaction

$C_{O_2}^*, C_{H_2}^*, C_{H_2O}^*$ = effective concentrations of the species

Combining the two equations and grouping the constants, the equation for the cathodic activation overpotential can be expressed in the following parametric form [42]:

$$\eta_{act, cathodic} = \beta_1 + \beta_2 T + \beta_3 T \ln(C_{O_2}^*) + \beta_4 T \ln(i) \quad (2.11)$$

$$\text{where: } \beta_1 = (-\Delta F_E) / (\alpha n F)$$

$$\beta_2 = R / (\alpha n F) \ln[n F A K_0 (C_{H_2}^*)^{(1-\alpha)} (C_{H_2O}^*)^{(\alpha)}]$$

$$\beta_3 = R / (\alpha n F) (1-\alpha)$$

$$\beta_4 = -R / (\alpha n F)$$

The same operation is performed for the anodic activation overpotential ($\eta_{act, anodic}$) and the terms combined. A series of tests are completed and the constant terms evaluated.

The results for a Ballard Mark IV cell are as follows [43]:

$$\eta_{act, anodic} = -0.9154 + 0.00312T + 7.4 \times 10^{-5} \ln(C_{O_2}^*) - 0.000187T \ln(i) \quad (2.12)$$

The definition of activation overpotential originated with battery operation, and thus is defined so that a positive value results in increased charging voltage. The opposite is true for fuel cells where activation overpotential is negative, resulting in a loss of cell voltage. The above model has the proper trends, becoming less negative with increasing temperature and increasing oxygen concentration while becoming more negative as the current increases. The result is a simple model that generally predicts performance trends better than pure empirical-based models.

Amphlett utilized the above modeling approach to predict the results of a 5 kW PEM stack [44]. The model reasonably predicted the cell voltages in the stack, with the

largest deviations occurring at the cells closest to the ends of the stack. The deviations probably occur due to water, gas flow, and temperature variations. Amphlett acknowledges model limitations including not considering thermal gradients [44]. The model approach was further utilized to attempt to develop a transient response model. An energy balance approach was used to determine the change in average cell temperature within a 5 kW PEM fuel cell stack. An interesting result was the comparison of modeled heat transfer losses to actual losses. The actual losses were approximately 10 times the modeled losses, showing simple models of convective heat transfer losses are not acceptable [45]. A similar energy balance approach was utilized by Lee in developing a fuel cell stack model, but there was no mention of heat losses from the stack [36].

Another means of stack modeling is to utilize existing cell or stack data. This method is used when stack specific test data is not available. Numerous tests have been performed on single cells to determine the effect of temperature, pressure, and contaminants on general cell behavior. Examples for phosphoric acid cells are detailed in the Table 2-12 [31]. Once the performance, or polarization curve, is known for a set of conditions, the effect of altering those conditions can be approximated using the above equations.

System Models

A fuel cell system includes all the components required to produce useable electricity from the feedstock fuel. These components include the following:

- fuel vaporizer or conditioner
- fuel reformer (including cleanup devices)

- fuel cell stack
- coolant
- heat exchangers
- pumps, blowers, compressors, etc.
- power conditioners

Table 2-12: Equations for phosphoric acid cells.

Parameter	Equation	Comments
Pressure	$\Delta V(\text{mV}) = 146 \log (P_2/P_1)$	1 atm < P < 10 atm
Temperature	$\Delta V(\text{mV}) = 1.15 (T_2 - T_1)$	180 °C < T < 250 °C
Oxidant	$\Delta V(\text{mV}) = 148 \log (P_{O_2})_2 / (P_{O_2})_1$	0.04 < $P_{O_2} / P_{\text{total}}$ < 0.20
	$\Delta V(\text{mV}) = 96 \log (P_{O_2})_2 / (P_{O_2})_1$	0.20 < $P_{O_2} / P_{\text{total}}$ < 1.0
Fuel	$\Delta V(\text{mV}) = 96 \log (P_{H_2})_2 / (P_{H_2})_1$	
CO Poisoning	$\Delta V(\text{mV}) = -11.1 ([CO]_2 - [CO]_1)$	163 °C
	$\Delta V(\text{mV}) = -6.14 ([CO]_2 - [CO]_1)$	177 °C
	$\Delta V(\text{mV}) = -3.54 ([CO]_2 - [CO]_1)$	190 °C
	$\Delta V(\text{mV}) = -2.05 ([CO]_2 - [CO]_1)$	204 °C
	$\Delta V(\text{mV}) = -1.3 ([CO]_2 - [CO]_1)$	218 °C
Current Density	$\Delta V(\text{mV}) = -0.53 \Delta J$	J = 100-200 mA/cm ² , P = 8.2 atm
	$\Delta V(\text{mV}) = -0.39 \Delta J$	J = 200-650 mA/cm ² , P = 8.2 atm
	$\Delta V(\text{mV}) = -0.74 \Delta J$	J = 50-120 mA/cm ² , P = 8.2 atm
	$\Delta V(\text{mV}) = -0.45 \Delta J$	J = 120-215 mA/cm ² , P = 8.2 atm
Life Effects	$\Delta V(\text{mV}) = -3 \text{ mV} / 1000 \text{ hours}$	

State 2: Parameter at the desired state

State 1: Parameter at state where stack performance is known

Source: [31]

The system model must not only mimic the performance of each component, but the model must simulate the interactions between components. The most common fuel cell system, and a commercial fuel cell product, is the International Fuel Cell's 200 kW phosphoric acid system. There are only a handful of complete, liquid-fueled fuel cell systems in the world and very little data has been presented on their operation. The result is a fundamental lack of understanding of fuel cell system behavior. The minimal

number of systems combined with the lack of performance data and makes developing system models very difficult.

To this point, nearly all of the system models are inadequate. Many of the models are based on single-point operation, and are not capable of simulating the system performance at off-design conditions. The component efficiencies (such as turbo-compressors) are not based on actual equipment and are often overstated. Parasitic power requirements are typically vastly underestimated. Losses, such as heat transfer to the environment are mainly ignored. Component interaction and the resulting operational limitations are not included. The net effect of the model shortcomings is that system projected performance is almost always overstated.

Design Point Models

Design point models simulate the performance of a system at one operating condition, typically called the design point. The models are limited and are often used to compare in general different fuels, reformers, and stacks. Design point modeling is reasonable for power plant applications where operation is mostly at a design point, but falls considerably short of what is necessary for transportation applications. Even in hybrid arrangements, such as fuel cells and batteries, the power output from the fuel cell can change substantially and quickly. The fuel cell systems for the 40' bus program at Georgetown University have response times under 10 seconds and the control logic has the fuel cell power output attempting to follow the vehicle load. As a result, the fuel cell power output is constantly changing, and the system operates at its design point only a fraction of the time.

A.D. Little presented a design point system model in a report comparing different reformer technologies [8]. The modeling included the following variables:

- Fuels: methane, methanol, ethanol
- Reforming technologies: steam reforming(SR), autothermal (ATR), partial oxidation (POX)
- Fuel cell type: phosphoric acid fuel cell (PAFC), proton exchange membrane fuel cell (PEM)
- Operating pressure: atmospheric (1 atm absolute), pressurized (4 atm absolute)

Table 2-13 provides the important design point parameters for the different component choices. Not all possible combinations were studied, and Table 2-14 details nine case studies. Finally, the nine cases were analyzed at the design point and the results are shown in Table 2-15.

The projected efficiencies range from 27.4% to 37.5%. The systems with high efficiencies typically incorporate steam reforming because of its high hydrogen yield. The parasitic power levels, between 0.5-2.5 kW, are low compared to known systems where the parasitic power levels of systems can easily be greater than 20% (5 kW) for pressurized systems. Even low-pressure, methanol-fueled, steam reformed PAFC systems have typical design point parasitic power levels of 7-10% as compared to only 2% presented in this report when modeling a methane-fueled, steam reformed PAFC.

Amphlett presented a simulation of a diesel-fueled PEM fuel cell system [46]. The diesel fuel is steam reformed at high temperatures, resulting in high CO levels. The system design includes a membrane separator that allows hydrogen gas to pass through

the membrane and blocks all other reformation products. The separated hydrogen was sent to the fuel cell while the remaining reformat products were combusted to provide the necessary heat for the reforming process. The operating pressure and membrane temperature were adjusted to determine the effect on system performance. For pressures less than 250 psig the performance of the system dropped off drastically due to low diffusion rates of the hydrogen gas through the membrane. The highest projected net system efficiency was approximately 39.5%.

Table 2-13: System design point parameters

Parameter	PEM	PAFC	PAFC
Gross DC Output	25 kW	25 kW	25 kW
Current Density (A/ft ²)	400	320	300
Temperature (°C)	80	190	190
Pressure (atm abs.)	3	3	1
Fuel Utilization	80%	80%	80%
Oxygen Utilization	50%	50%	50%
Pump Efficiency	70%	70%	70%
Compressor Efficiency	70%	70%	n/a
Expander Efficiency	70%	70%	n/a

Source: [8]

Sutton presented a summary paper describing the electrochemical (fuel cell) engine development effort underway at General Motors [47]. Without providing specifics, the modeling results presented showed system efficiencies greater than 50%, especially at part load operating conditions.

Kinoshita and Landgrebe presented models relating power and energy to the weight of the system including fuel and fuel storage [48]. The relationship between various electrochemical parameters, such as cell voltage, and the optimum weight of the system was investigated. The optimum cell voltage for minimum system weight was in the range 0.67-0.70 volts. The report also compares the relationship between specific

Table 2-14: Design point case studies

Case	1	2	3	4	5	6	7	8	9
Fuel cell	PEM	PEM	PEM	PEM	PEM	PAFC	PAFC	PAFC	PAFC
Reformer	SR	ATR	POX	SR	SR	SR	ATR	ATR	POX
Fuel	Methane	Methane	Methane	Methanol	Ethanol	Methane	Methane	Methane	Methane
Pressure	3	3	3	3	3	3	1	1	1

Source: [8]

Table 2-15: Results of design point analysis [8]

Case	1	2	3	4	5	6	7	8	9
Fuel cell	PEM	PEM	PEM	PEM	PEM	PAFC	PAFC	PAFC	PAFC
Reformer	SR	ATR	POX	SR	SR	SR	SR	ATR	POX
Fuel	Methane	Methane	Methane	Methanol	Ethanol	Methane	Methane	Methane	Methane
Pressure	3	3	3	3	3	3	1	1	1
Results									
Gross Power	24.9	25.1	24.9	25.0	25.0	25.0	25.0	25.1	25.0
Parasitic	1.9	2.5	1.8	2.9	2.3	1.7	0.5	0.5	0.6
Fuel Flow (kg/hr)	17.17	36.03	35.13	17.28	19.11	17.93	17.60	40.00	38.97
Net Efficiency	30.7%	29.6%	28.6%	37.5%	29.7%	37.0%	35.5%	28.9%	27.4%

Source: [8]

power and specific energy and presents data versus model results. The specific power is highest at low specific energy conditions because the specific energy is highest when the fuel storage is large and the specific power is greatest at small fuel storage.

Kumar presented a thermodynamic review of fuel cell systems designed for vehicular applications [49]. The systems included a liquid and air-cooled PAFC, a PEM system, and a solid-oxide fuel cell system. The efficiencies, based on higher heating value, ranged from 39.4% for the liquid-cooled PAFC to 29.7% for the PEM. The PEM system had the lowest efficiency due to large parasitic power consumption (primarily associated with pressurization), 15% of gross power. The sensitivity of efficiency to fuel utilization, parasitic power, and heat loss were also investigated. The efficiency curve for the liquid-cooled PAFC engine increased as the fuel utilization increased (up to 90% fuel utilization).

Krumpelt presented a paper discussing fuel cell system integration [50]. The research showed the effects of thermal and chemical integration on system efficiency, including interaction between components. In addition, the comparison of efficiency and economics are presented. Very efficient systems are typically very complex and more expensive than simpler, less efficient systems.

Off-Design Models

Modeling of fuel cell systems at off-design points is limited. The reason for the limited modeling is most of the fuel cell systems that have been built were for power station or near-constant power applications. These systems typically operate at or near a design point, and the systems have been designed primarily for optimizing performance at that point. The transportation application, however, often requires a system to operate

at a variety of operating points. Because only a small number of fuel cell systems have been designed, built, and tested for the transportation application, minimal off-design modeling and test data are available.

One exception is the DOE/DOT/Georgetown University Fuel Cell Bus Program that is currently developing their second generation of fuel cell-powered transit buses. As part of the development of the first generation vehicles, two methanol-fueled, steam-reformed 25 kW phosphoric acid fuel cell "brassboard" systems were developed. One was air-cooled and the other was liquid-cooled. The goal of this phase of the project was to determine which system was best suited for the bus application. The system chosen would be scaled up to 50 kW and integrated into three 30' hybrid buses. Computer simulation of both systems were developed to aid the down-select process [51]. Based on limited data and design information, system models were developed to model design and off-design performance as well as limited transient capability. The results of the simulation correlated quite well with the available data, and the simulation was incorporated into an overall vehicle code known as HYBRID. The results of the fuel cell system model showed that the liquid-cooled system had significant performance advantages over the air-cooled system, primarily in the effective utilization of stack waste to vaporize the liquid methanol and water. The overall efficiency of the liquid-cooled system ranged from 35-40% at design power output to below 20% at lower power outputs. The system model showed dramatically different performance curves than previously presented, but the results show similar shapes to curves presented by International Fuel Cells for their 100 kW PAFC designed for

transportation applications [52]. The vehicle simulation results also showed the liquid-cooled system would better meet the vehicle performance requirements.

The results of the limited transient capabilities of the code showed the fuel processor to be the factor limiting the transient response of the system [53]. The system was incorporated into a hybrid arrangement with nickel-cadmium batteries. The control architecture was defined as battery-leading, meaning the batteries would follow the vehicle loads and the fuel cell system would respond depending on the battery state of charge, energy output, etc. Consequently, the system did not require fast transient response capabilities. The resulting system as designed took approximately 4 minutes to change from 25% to 100% of design power output. The analysis showed that the limiting rate factor was the rate of heat transfer into the reformer catalyst bed. As the power is increased, the flow rate of the fuel mix is also increased and thus the heat removal from the catalyst bed (endothermic reaction) for the reforming process is likewise increased. Increasing the rate of heat transfer into the bed is inherently slow, requiring raising the reformer wall temperatures to create larger temperature differences between the wall and the catalyst bed. The simulation showed that the time constant for the reformer response was on the order of 1-3 minutes, roughly the response of the system. If the power output changed faster than the four-minute rate, the reformer catalyst bed temperature would collapse and the local rate of reformation would slow, resulting in a reduced conversion percentage of the methanol to hydrogen. The modeling resulted in realistic system response, but will require more experimental detail to further verify and "tune".

The above system model was further expanded with the addition of new models for fuels, reforming process, and stack type [54]. The following is a list of current possible system choices:

- fuels: methanol, ethanol, methane, or hydrogen
- stack types: PAFC or PEM
- reformers: steam reformer, partial oxidation, autothermal

The models reasonably simulate design and off-design conditions but will require significantly more data to be able verify performance. A comparison of the various system choices showed that a low pressure, methanol-fueled, steam reformed phosphoric acid system has the highest projected system efficiency. Steam reforming optimizes the hydrogen yield, phosphoric acid has a high CO tolerance, and utilizing atmospheric pressure minimizes parasitic power losses.

Geyer presented a dynamic model of a methanol-fueled, steam-reformed PEM fuel cell system [55]. The modeling showed that the heat transfer within the reformer catalyst bed limits the transient response of the system. The model also showed problems with overheating the catalyst bed when the power output from the system drops sharply. The model further showed that there is a significant energy penalty associated with start-up. Almost 1200 seconds of operation were required to achieve 90% of steady-state system efficiency.

Efficiency

Introduction

Efficiency of fuel cell systems and components is difficult to define in a consistent manner. The variety of fuels, reformers, and stack types makes comparing

system efficiencies very difficult. In addition, changes to the system such as the number of cells in a stack can have dramatic changes on the efficiency of a system. Other thermodynamic properties such as operating temperature and pressure can also significantly alter the system efficiency. For example, Virji reported that the efficiency for a methane-fuelled, turbo-compressor PEM system increases from 25% and 33% efficiency with an increase in absolute operating pressure from 1.5 bars and 4 bars[56]. What is needed is a set of clear, appropriate definitions that allow for direct comparisons of systems and components.

Efficiency Definitions

Typically, overall efficiency is defined for electrical power systems as net electrical power out divided by the lower heating value of the total fuel used. This is also true for fuel cell systems, but there is not always a clear picture of what is the total fuel used or net power output. For example, for systems utilizing liquid hydrogen or pressurized hydrogen, the question arises whether to subtract the energy required to liquify or compress the hydrogen. In transportation applications, heat removal from fuel cell systems often occurs through the use of radiators. Does the power required to pump the coolant count against the fuel cell system efficiency? On the second generation of fuel cell buses developed at the Georgetown University, the coolant pumping requirements for the fuel cell system and the power electronics are between 2-4 kW, a substantial percentage (3-5%) of the average vehicle power requirement.

Thermodynamic efficiency

The ideal thermodynamic efficiency is a measure of maximum efficiency for the electrochemical reaction. The theoretical maximum useful electrical work for a cell

operating at constant temperature and pressure is the change in the Gibbs free energy.

Therefore, the thermodynamic efficiency is defined as follows [8, 32]:

$$\eta_{TH,ideal} = \Delta G_r / \Delta H_r = 1 - T \Delta S_r / \Delta H_r \quad (2.13)$$

where: ΔG_r = change in Gibbs free energy for the given reaction

ΔH_r = change in enthalpy for the given reaction

T = absolute temperature

ΔS_r = change in entropy for the given reaction

For the electrochemical combination of oxygen and hydrogen to form water at standard conditions, the ideal thermodynamic efficiency is approximately 83% [32]. The thermodynamic efficiency is useful to show that high temperatures are not required to theoretically achieve high efficiency. The loss in efficiency (below 100%) under reversible conditions occurs from heat transfer required for isothermal operation. The thermodynamic efficiency is determined by the operating temperature, operating pressure, and cell electrochemical reaction.

Voltage efficiency

The voltage efficiency compares the actual voltage to the theoretical open circuit voltage. The theoretical open circuit voltage is related to the Gibbs free energy change by the following equation [33]:

$$V_{ThOC} = \Delta G_r / nF \quad (2.14)$$

where: V_{ThOC} = theoretical open circuit voltage

The voltage efficiency is defined as follows [8]:

$$\eta_v = V / V_{ThOC} \quad (2.15)$$

The voltage efficiency is not constant for a cell operating at steady conditions, but varies with the current density. As the current draw increases, the losses within the cell increase and the voltage efficiency is lower due to a lower cell voltage.

Current efficiency

The current efficiency is a measure of the amount of the fuel (typically hydrogen) that passes into a cell that is consumed by the cell for the electrochemical reaction. The current efficiency is a direct measure of the fuel utilization factor, which is the fraction of hydrogen entering the anode electrode that is consumed by the electrochemical reaction. The current efficiency is defined as follows [8]:

$$\eta_I = I_{act} / I_F \quad (2.16)$$

where: I_{act} = actual current

I_F = current if all fuel was consumed in a electrochemical reaction

There are three possible scenarios for the fuel entering the anode electrode:

- consumed in the electrochemical reaction
- consumed in a side reaction
- passes through the cell

Fuel consumed by side reactions must be minimized because side reactions reduce efficiency and can cause damage by localized heating within the cells. Fuel passing through the cell may be utilized elsewhere (such as heat for fuel processor) and does not necessarily reduce overall system efficiency.

Electrochemical efficiency

The electrochemical efficiency is a measure of how effectively the cell or stack converts the fuel energy available into electrical energy. The electrochemical efficiency is the product of the thermodynamic, voltage, and current efficiencies [8].

$$\eta_E = \eta_{TH} \cdot \eta_V \cdot \eta_I \quad (2.17)$$

Heating Value Efficiency

The heating value efficiency is a measure of the lower heating value of the usable cell fuel to the overall heating value of the feed gas entering the anode. In the gas of a reformed fuel, unconverted fuel and other combustible species increase the heating value of the anode feed gas. The heating value efficiency is defined as follows [8]:

$$\eta_{HV} = H_{2,LHV} / (\text{Feed Gas})_{LHV} \quad (2.17)$$

For pure hydrogen gas as the anode feed gas, the heating value efficiency is 1.

Fuel Cell Efficiency

The fuel cell efficiency is a measure of the direct current electrical power produced by a cell or stack compared to the heating value of the anode fuel stream [8].

$$\eta_{FC} = \text{DC Power} / (\text{Feed Gas})_{HV} = \eta_{HV} \cdot \eta_E \quad (2.18)$$

The heating value is used is typically the higher heating value for power plant applications and the lower heating value for transportation applications. For transportation PEM systems, however, the higher heating value may be more accurate because the stack operates at only 80 °C, thus allowing the water to condense [8].

Fuel processor efficiency

The fuel processor efficiency is often defined as the ratio of the lower heating value of the reformer product to the lower heating value of the total fuel input. The equations is as follows [8]:

$$\eta_{FP} = (\text{Feed Gas})_{LHV} / (\text{Total Fuel Input})_{LHV} \quad (2.19)$$

This definition can be misleading because a processor that converts none of the primary fuel can have an efficiency of 100%. Said another way, an insulated pipe where no reforming process occurs has a fuel processor efficiency of approximately 100%. A clearer definition would include the heating value efficiency to compare the usable anode gas heating value to the total fuel heating value. This would be a measure of how efficiently the fuel processor converts the primary into hydrogen gas.

Gross system efficiency

The gross system efficiency is a ratio of the electrical power produced divided by the heating value of the total fuel input into the fuel cell engine [8]. The total fuel input includes the primary fuel flow into the fuel processor plus any additional fuel flow into the burners, etc.

$$\eta_{Gross} = \text{Gross Electrical Power} / (\text{Total Fuel Input})_{HV} \quad (2.20)$$

Net system efficiency

The net system efficiency accounts for all the parasitic losses within the system. The net power is the gross conditioned power minus the parasitic electrical power.

$$\eta_{Net} = \text{Net Electrical Power} / (\text{Total Fuel Input})_{HV} \quad (2.21)$$

The electrical power should be in usable form, thus any losses from DC-DC converters or AC inverters should also be subtracted from the gross electrical power.

Reported Efficiencies

There is a wide range of efficiency values reported in the literature. Some of the disparity is due to the wide range of possible components and fuels that can define a fuel cell system. Other variations occur from different authors stating different efficiencies such as cell efficiency versus net efficiency. Others are overly optimistic on the fuel cell performance. Table 2-16 lists a small fraction of the fuel cell efficiencies reported in the literature.

The wide variety of reported efficiencies highlights the uncertainties and inconsistencies with fuel cell engine modeling. In addition, as stated earlier, changes to the system parameters can dramatically alter the efficiency of a system. If more cells are added to the stack, for a given power output, the cell current density is reduced and the cell voltage increases (move to the left on the polarization curve of Figure 2-1). This would probably increase the design-point efficiency of the system, but the trade-off is an engine that would be heavier and more costly. Thus depending on the constraints (weight, volume, cost, etc.) different models would show different efficiencies.

There is not known to be available in the literature a detailed study of efficiency of a working system. Most studies and reports are based on simplifying assumptions such as constant component efficiencies, average parasitic power, ideal heat transfer, etc. As a consequence, one of the major goals of this research was to utilize the brassboard fuel cell engine to provide a detailed breakdown of the energy flow throughout the engine at design and off-design power levels. The effects of control, operating strategies, operation set points, and losses within the engine were analyzed.

This study therefore provides detailed information leading to a greater understanding of engine efficiency performance and interactions.

Emissions

The potential for extremely low emissions is one of the main reasons for the intense interest in fuel cell technology. Fuel cell engines have the capability to drastically reduce the emissions when utilized for transportation application, including classification as a zero-emission vehicle (ZEV) in the case of hydrogen-fueled engines. At this point, however, few complete fuel cell systems or engines have undergone emissions testing.

The regulated emissions of interest are oxides of nitrogen (NO_x), carbon monoxide (CO), and organic compounds. Different terms are used to describe organic compounds of interest, and historically the term non-methane hydrocarbons (NMHC) has been used. NMHC does not cover oxygenated hydrocarbons and aldehydes, which both play an important role in alcohol fuel emissions [1]. It is more appropriate to use non-methane organic gas (NMOG), which includes NMHC and oxygenated hydrocarbons and aldehydes. For heavy-duty vehicles, particulate matter is also a concern since they are typically associated with diesel engines. Carbon dioxide (CO_2) is not a regulated emission, but there is significant interest in minimizing its production due to its possible role in global climate change [1].

International Fuel Cells produces the commercially available PC25, a 200 kW natural gas-fueled phosphoric acid fuel cell system. Emissions tests were performed on unit sited at the South Coast Air Quality Management District headquarters in Diamond Bar, California. Table 2-17 details the results of the testing [62]:

Table 2-16: Reported fuel cell system efficiencies.

Author	Stack	Fuel	Design Point	Off-Design	Comments	Ref.
A.D. Little	Various	Various	27.4-37.5%	N/A		[8]
Blomen	PAFC	Methanol	59.56%	N/A	LHV	[32]
Blomen	PAFC	Natural Gas	41%	38-43%	Efficiency increases at low power	[32]
Blomen	Alkaline	Natural Gas	N/A	34-38%	Efficiency increases at low power	[32]
Amphlett	PEM	Diesel	38.5%	N/A	H ₂ membrane separator	[46]
Virji	PEM	Methane	25%	N/A	1.5 Bars operating pressure	[56]
Barbir	PEM	Methane	33%	N/A	4 Bars operating pressure	[56]
Oliveira	PEM	Hydrogen	50%	50-63%	Atmospheric pressure	[57]
Friedman	PEM	Hydrogen	50%	0-50%	0% at 15% Power Output	[58]
Fletcher	PAFC	Hydrogen	25-30%	10-45%	Maximum at 20% Power Output	[59]
Ogden	PEM	Methanol	38%	14-40%		[51]
		Hydrogen	101 mpeg ^a	N/A	Integrated into a vehicle	[12]
		Methanol	71 mpeg ^a	N/A		[12]
		Gasoline	69 mpeg ^a	N/A		[12]
Mark	PEM	Hydrogen	80 mpeg ^a	N/A	Integrated into a vehicle	[60]
		Methanol	69 mpeg ^a	N/A		[60]
		Gasoline	42-64 mpeg ^a	N/A		[60]
Arcadis	PEM	Methanol	41%	above 40%		[61]
	PEM	Methanol	32%	32-38%		[61]
	PAFC	Methanol	42%	28-42%	DOE/DOT Fuji fuel cell	[61]
	PAFC	Methanol	42%	31-42%	DOT IFC 100 kW unit	[61]
Kumar	PAFC	Methanol	30.1-39.4%	N/A	Higher heating value	[49]
	PEM	Methanol	29.7%	N/A	Higher heating value	[49]

^a mpeg: miles per energy equivalent of gasoline

Table 2-17: Results of PC25 emissions testing based on PPMv (15% O₂, Dry)

Contaminant	SCAQMD Standard	PC25 Emissions
Nitrous Oxides	3	0.45
Carbon monoxide	10	1.1
Non-methane hydrocarbons	250	0.03

Source: [62]

Table 2-18 details the comparison of the PC25 emissions to the average United States utility emissions [62].

Table 2-18: Comparison of PC25 emissions to the utility average on a pounds per megawatt-hour basis

Contaminant	Utility Average	PC25
Nitrous Oxides	7.65	0.016
Carbon monoxide	0.34	0.023
Reactive Organic Gases (ROG)	0.34	0.00004
Sulfur Oxides - SO _x	16.1	0
Particulates	0.46	0

Source: [62]

Table 2-17 shows dramatic reductions in fuel cell power plant emissions as compared to the utility average.

One of the few fuel cell systems designed for transportation to undergo emissions testing is one of the three DOE/DOT fuel cell/battery hybrid buses. The transit bus was tested at the West Virginia University Mobile Emissions Testing Laboratory, and Wimmer reported the results of the testing [63]. Table 2-19 compares the results of the emissions testing to other transit buses.

The nitrous oxides and particulate matter emissions for the fuel cell vehicle were significantly lower than other transit buses. The hydrocarbons (HC) and carbon monoxide (CO) were much higher than expected and similar to the levels of the other transit buses. One reason for high CO and HC levels was the fuel cell bus was a

prototype, and the fuel cell system was not optimized for low emissions. It is also possible that the stiff requirement for low weight, small volume, and fast transient response times required for the transportation application will result in higher emissions than those of fuel cell power plants (PC25).

Table 2-19: Comparison of transit bus emissions tested by West Virginia University

Bus Type	Buses tested	HC (g/mile)	CO (g/mile)	NO _x (g/mile)	PM (g/mile)
1996 Flyer Diesel	8	0.13	4.9	30.1	0.28
1994 Flyer Diesel	3	0.09	5.2	28.4	0.77
1998 Flexible Biodiesel	1	2.32	11.6	54.0	0.95
1998 Flexible Diesel	1	2.41	14.3	49.5	1.15
1996 Flyer Nat Gas	10	15.8	9.0	20.8	0.02
1992 B1A Nat Gas	1	6.02	4.0	20.6	0.00
1992 TMS Ethanol	5	8.9	37.1	13.4	0.63
1992 Flexible Methanol	5	37.5	25.1	11.6	0.39
Fuel Cell	1	0.23	7.32	0.01	<0.01

Fuel Chain Emissions

Hydrogen-fueled fuel cell systems do not produce any regulated tail-pipe emissions. The production of hydrogen fuel, however, does produce regulated emissions. Also, both methanol and hydrogen are produced almost entirely from natural gas. Therefore to properly analyze the emissions from various systems the emissions associated with the fuel chain need also to be considered. The analysis is beyond the scope of this dissertation, but information is provided for comparison purposes.

A.D. Little presented a comprehensive report of efficiency and emissions of transportation fuel chains [64]. For efficiency, the following stages of production were analyzed:

- extraction and processing
- transportation
- refinery/processing
- retail distribution
- refueling

The efficiency and emissions for each stage of production are listed. Table 2-20 provides a summary of the selected fuel chain efficiency and emissions levels. It is of interest to compare the emissions associated with hydrogen and methanol production from natural gas and coal. The CO₂ production is much higher for hydrogen than methanol, and the regulated emissions are comparable.

Table 2-20: Efficiency and emission levels of selected fuel chains

Energy Resource	Transportation Fuel	CO ₂ (g/KJ) ^a	SO _x (g/KJ) ^a	NO _x (g/KJ) ^a	CO (g/KJ) ^a	NMHC (g/KJ) ^a	CH ₄ (g/KJ) ^a	PM (g/KJ) ^a	Efficiency (%)
Petroleum	Gasoline	13555	25.3	37.7	15.6	27.1	8.0	12.8	84.1
Petroleum	Diesel	6119	11.9	23.9	11.8	11.6	7.2	3.8	91.4
Natural Gas	Methanol	21924	18.7	94.2	25.5	32.2	110.9	5.2	61.5
Natural Gas	Hydrogen	73234	22.2	83.3	20.1	21.3	95.9	5.3	71
Coal	Methanol	78422	23.6	43.8	10.8	13.6	458.2	5.5	59.7
Coal	Hydrogen	151647	91.0	95.1	14.1	5.0	508.3	15.8	53.8
Corn	Ethanol	83880	432.8	257.1	36.8	15.3	1.9	334.3	38.6
Renewables	Hydrogen	4183	16.7	25.3	1.5	0.1	0.1	2.6	24.6
U.S. Electricity	Hydrogen	229142	897.0	682.1	93.4	22.1	601.2	144.2	24.1

Source: [64]

^a: based on higher heating value

CHAPTER 3: FUEL CELL ENGINE DESCRIPTION

Introduction

This chapter describes in detail the University of Florida Fuel Cell Laboratory 25 kW brassboard fuel cell engine. The performance specification for the overall engine and major components are listed, and when available, comparison data for the transit bus 50kW fuel cell engine is provided.

Background

Fuel cell engines have the potential to produce electricity efficiently with few emissions. The downside historically has been the low power density, the high costs, and the severely limited availability. Until fairly recently, these limitations restricted their utility to a few specialized applications such as providing electrical power for space flights. However, in 1986, Los Alamos National Laboratory completed a study that concluded that fuel cell technology had progressed to a point that it was feasible to power a transit bus with a fuel cell/battery hybrid arrangement [2]. Based on the positive results of the feasibility study, the Department of Energy and the Department of Transportation initiated a program to develop three fuel cell/battery hybrid transit buses.

The first phase of the project was to develop the fuel cell power plant. Phosphoric acid fuel cells (PAFC) were chosen because of their modest operating temperature, tolerance to CO and CO₂, and the fairly advanced state of stack

development. The fuel chosen was methanol because it is a liquid fuel, easily steam reformed into hydrogen-rich gas at low temperatures, and can be manufactured from numerous feedstock fuels such as natural gas and coal. Modeling results showed that a 50 kW power plant would be able to provide the average vehicle power requirements for typical transit routes. Batteries would contribute the additional power needed for the vehicle peak power requirements, and would be recharged during periods of low vehicle power requirements.

As part of the downselect process, two groups of developers were chosen to develop 25 kW half-scale PAFC (brassboard) systems operating on methanol fuel. Brassboard is a term used to define a fully operational laboratory system. The system ultimately selected would then be scaled up to 50 KW and incorporated into three 30' transit buses. Energy Research Corporation (ERC) developed an air-cooled PAFC system. Fuji Corporation of Japan developed a liquid-cooled system based on Englehart Corporation fuel cell system designs. Both systems were designed and fabricated. In 1990, the results of system testing were reported [65, 66]. The Fuji liquid-cooled system was selected because of higher system efficiency, DC-DC converter design, and overall reliable operation. The main advantage of a liquid-cooled system is the waste heat produced in the stack can be used for fuel vaporization, resulting in higher overall efficiency.

During the downselect process, the University of Florida was contracted to develop overall engine models for both systems [51]. The resulting models were incorporated into overall vehicle models to help determine which system was better suited for the transit bus application. After the downselect process was completed, both

brassboard systems were subsequently transferred to the University of Florida for laboratory development. The air-cooled system was received in 1993, and its condition was such that operation was not practical. In 1995, the liquid-cooled system (referred to as the brassboard system) was received and incorporated into the University of Florida Fuel Cell Research and Training Laboratory.

The Fuji 25 kW, liquid-cooled PAFC brassboard system is the basis for the research reported in this dissertation. This system is unique as there are, still to this day, only a handful of known fully operational, liquid-fueled fuel cell systems. In addition, the brassboard system was designed for laboratory research, thus allowing access to all the components and subsystems. This is not possible on the three 50 kW systems designed for integration into the transit buses. The result is that the brassboard is an exceptional research tool that allows a rare, detailed insight into the behavior and performance of a fuel cell engine.

Fuel Cell System Description

The Fuji 25 kW PAFC system is a complete power plant designed to operate in a hybrid arrangement with a battery pack. The fuel utilized is methanol. The system has four methanol pumps, one de-ionized water pump, and a coolant pump. There are three blowers, one each for the stack, the reformer burner, and the startup burner. There are three corresponding exhaust lines for each blower. The fuel processor is a low temperature (260-280 °C) copper-zinc-oxide catalyst steam reformer. The stack is a phosphoric acid type, and is liquid-cooled. The electrical power produced is chopped in a DC-DC converter for hybrid (parallel) operation with a battery pack. Parasitic power is delivered from individual power supplies operated off wall power. A switchboard is

used to deliver the wall power to the necessary components. Automated control is achieved through a control computer and data acquisition system. The specifications for the brassboard fuel cell system are listed in Table 3-1.

Table 3-1: Brassboard fuel cell system specifications.

Fuel Cell Type	Phosphoric Acid
Stack Rated Power	25 kW
Chopper Rated Power	22.5 kW
Fuel	Commercial Grade Methanol
Water	De-ionized water
Methanol Consumption	11.3 kg/hr (rated power)
Water Consumption	9.5 kg/hr (rated power)
System Efficiency	36% (at rated power)
Chopper Efficiency	90%
Start-up Time	<45 minutes
Ambient Temperature	5-40 °C
Relative Humidity	0-90%
Inert Purge Gas	CO ₂ or N ₂

Source: [66]

A simple schematic of the brassboard system is shown in Figure 3-1. The overall brassboard configuration, including power electronics, is depicted in Figure 3-2.

Fuel Processor Subsystem

The fuel processor subsystem includes all the components required to convert methanol and water fuel mixture into a hydrogen rich gas. This subsystem includes the following components:

- methanol and water pumps P-01, P-02, P-03, P-05
- blower FAN-01
- HX-01: vaporizer heat exchanger (cold side)
- steam reformer
- fuel tanks

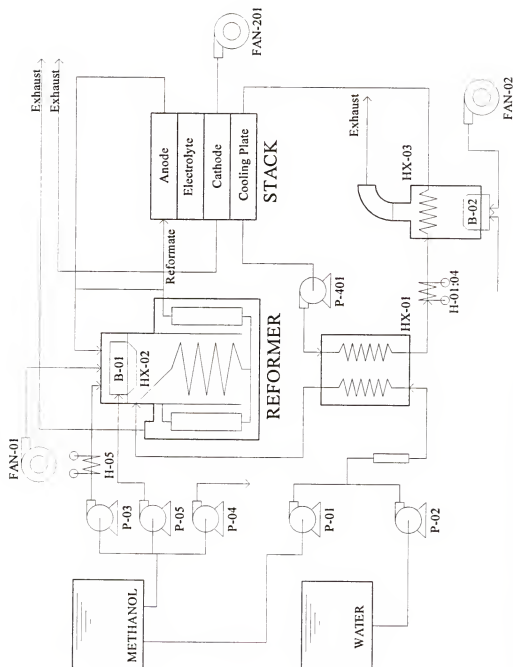


Figure 3-1: Schematic of the brassboard fuel cell engine.

Electronics Section

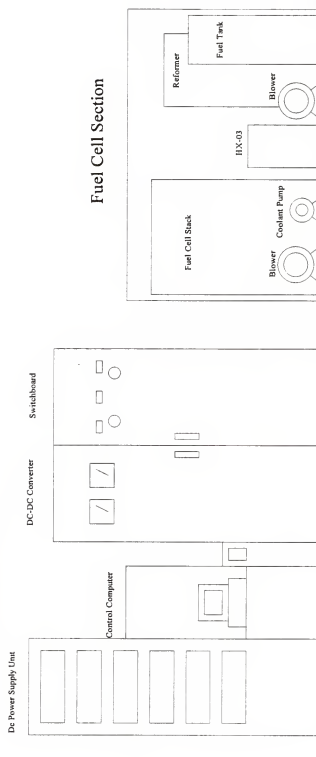


Figure 3-2: Configuration of entire brassboard fuel cell engine.

- piping, valving, filters, etc.
- heater H-05

The methanol and de-ionized water are stored in separate tanks. The primary methanol pump, P-01, and the water pump, P-02, are identical positive-displacement gear pumps. There is a linear relationship between pump volumetric flow rate and motor voltage, and by simple control algorithms the desired 1.5 steam-to-carbon ratio in the fuel mixture is maintained for various flow rates. The fuel mixture passes through a mixing section and into the HX-01, the vaporizer heat exchanger. HX-01 is a plate-type exchanger where energy is transferred from the fuel cell coolant to the fuel mix. In this way, excess heat from the fuel cell stack is not wasted but used to vaporize the fuel mixture. Plate-type heat exchangers are well suited for vaporizing mixtures because of the large surface area and turbulent flow which ensures good mixing in the two-phase region.

The vaporized fuel mixture leaves HX-01 and enters the steam reformer. The fuel mix leaves HX-01 at approximately 145-150 °C (coolant temperature), which is well below the nominal reformer catalyst bed temperature of 280 °C. The vaporized fuel mix temperature must be greater than 200-220 °C for the reforming reaction to occur and minimize carbon formation. To raise its temperature, the fuel mix first enters a superheater section in the reformer. A superheater section is necessary because if the fuel mix were to enter the catalyst bed at 150 °C, the first section of the catalyst bed would transfer heat to the fuel mix to raise its temperature rather than reforming the fuel mix. This in turn would reduce the effective size of the catalyst bed. The superheated fuel mix is then passed over the catalyst bed consisting of copper-zinc oxide pellets

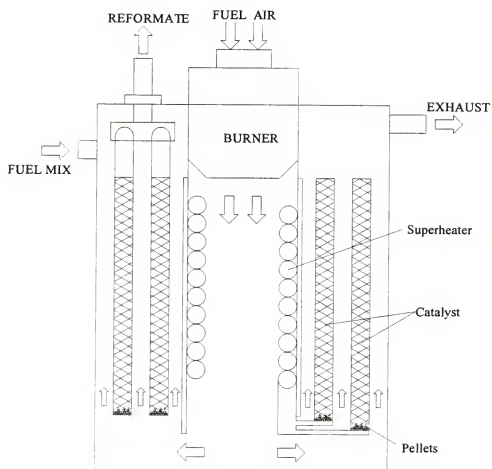
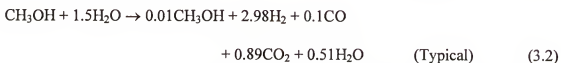


Figure 3-3: Typical methanol steam reformer cross-section.

where the reforming reaction occurs. A typical cross-section of a methanol steam reformer is shown in Figure 3-3 [66].

The following are the ideal and typical methanol steam reforming reactions (catalyst bed temperature of 280 °C):



The extra water (1.5 steam-to-carbon ratio) is utilized to minimize the CO formation and maximize the hydrogen production through the water-gas shift reaction. The equilibrium level of CO increases with increasing bed temperature. The reaction product from the reforming is called reformat.

Steam reforming of methanol is an endothermic reaction. Energy is supplied to superheat and reform the fuel mix by the hot combustion products from the reformer burner. The fuel for the reformer burner is supplied from two methanol pumps as well as the unreacted portion of the anode feed gas. Approximately 60-80% of the hydrogen produced during the reforming reaction is consumed at the stack anode with the residual hydrogen gas and other reformat constituents (collectively known as flue gas) utilized as the primary fuel for the reformer burner during normal operation. Pump P-03 is the methanol trim pump whose flow rate varies according to the reformer requirements. The P-03 methanol flow passes through an electric heater (H-05) to vaporize the methanol before it enters the reformer burner. By vaporizing the methanol, all the fuel combusted by the reformer burner during normal operation is in the gaseous form. Pump P-05 is a digital (on-off) solenoid pump that provides liquid methanol to the

reformer burner only during startup. The blower FAN-01 supplies the reformer burner air.

The specifications for the brassboard steam reformer are shown in Table 3-2 [66]. For comparison, the specifications for the 50 kW reformer installed on the hybrid transit bus are also listed.

Table 3-2: Brassboard steam reformer specifications.

Parameter	Brassboard Reformer	Bus Reformer
Output	for 25 kW stack	for 50 kW stack
Process	Steam reforming	Steam reforming
Methanol Conversion	>99%	>99%
Reforming Fuel	Methanol	Methanol
Steam-to-Carbon ratio	1.5	1.5
Catalyst	CuO + ZnO type	CuO + ZnO type
Size	1.64 ft dia x 2.63 ft	2.3 ft dia. x 3.3 ft
Weight	133 kg	200 kg

Source: [66]

The specifications are nearly identical except for size and weight. The reformer on the bus requires double the reforming capacity (fuel mix flow rate) but is only 50% heavier. One performance parameter for steam reformers is the flow rate of fuel per weight (or volume) of catalyst. This is an indication of the residence time for the reforming reaction. The fuel mixture in the brassboard reformer has a higher residence time which results in higher methanol conversion, longer lifetime, and more stable bed temperatures.

Fuel Cell Stack Subsystem

The fuel cell stack is where hydrogen and oxygen are electrochemically combined to form water and produce electricity. For the brassboard, phosphoric acid is

the stack electrolyte and platinum is the catalyst for both electrodes. The stack section includes the following components:

- fuel cell stack
- piping, valving, filters, etc.
- blower FAN-201

The stack consists of 88 individual cells connected in series. Each cell has an active area of 2000 cm^2 . Specifications for the brassboard fuel cell stack are presented in Table 3-3 [66]. Specifications for the bus fuel cell stack are also presented for comparison.

Table 3-3: Fuel cell stack specifications.

Parameter	Brassboard Stack	Bus Stack
Rated Power	25 kW	50 kW
Rated Current	480 amps	480 amps
Rated Voltage	52.8V	105 V (52.8V x 2)
Single Cell Performance	0.60V at 240 mA/cm^2	0.66V at 240 mA/cm^2
Pressure	Atmospheric	Atmospheric
Number of Cells	88	80 x 2 stacks
Cell Area	2000 cm^2	2000 cm^2

Source: [66]

The stack subsystem operation is simple, as there are few components and minimal moving parts. The reformate (hydrogen-rich gas) enters the stack anode electrode. The utilization of the hydrogen gas within the stack is typically between 60-80%. The remaining hydrogen, in addition to the non-hydrogen gases, leave the stack anode and are piped to the reformer burner. Excess air is delivered to the stack cathode electrode from blower F-201, where 40-50% of the oxygen is consumed by the cathode electrode. The electrical current produced by the stack is controlled by the step-up chopper (DC-DC converter). The cathode exhaust, partially oxygen depleted air and water produced by the electrochemical reaction, is vented to the atmosphere. The liquid-

coolant removes the excess heat produced by the stack by passing through coolant plates placed every 3-5 cells.

Coolant Loop

The liquid coolant removes excess heat energy from fuel cell stack and uses it to vaporize the liquid fuel mix. The remainder of the waste heat is removed from the engine by heat transfer to the environment through the startup heat exchanger. The coolant loop consists of the following components:

- coolant pump P-401
- HX-03 startup heat exchanger
- methanol pump P-04
- blower Fan-02
- heaters 01-04
- HX-01 vaporizer heat exchanger (hot side)
- coolant overflow tank
- startup burner B-02
- piping, valving, filters, etc.

The coolant passes through the fuel cell stack in cooling channels either removing or adding energy to the stack. The coolant leaves the stack and enters heaters H-01 and H-02, two resistive heaters placed in the coolant line. These heaters are operated when the fuel cell system is in idle mode, producing stack electrical power but the chopper output power is zero. The coolant then enters the vaporizer heat exchanger HX-01 where energy is transferred to vaporize the fuel mix. After exiting HX-01, the coolant enters the tubes of HX-03, the tube-fin startup heat exchanger.

Energy is typically added to the coolant during startup and low stack power output, while energy is removed from the coolant during high stack power operation and shutdown. Energy can be removed from the coolant by operating Fan-02 and blowing air across the fins of the heat exchanger. Energy can be added to the coolant by operating the burner B-02 and sending the combustion product across fins of the heat exchanger.

Power Electronics Subsystem

The power electronics include all the components required to convert the stack electrical power into useful power in a hybrid arrangement as well as providing the system parasitic power requirements (from wall power). The following is a list of power electronic components:

- step-up chopper (DC-DC converter)
- switchboard
- power supply unit

The power required by the various pumps, blowers, etc. within the brassboard system is supplied from wall power. The switchboard is used to distribute wall power to the necessary components. In addition, the switchboard provides the breakers, relays, fusing, control signals, indicator lamps, and resets associated with safe operation of the components off wall power. The initial requirements were specified by the manufacturer for the switchboard are the following:

- AC 200 V $\pm 10\%$, 3 phase, 3 wire 50/60 Hz, 2kVA
- AC 100 V $\pm 10\%$, single phase, 2 wire 50/60 Hz, 15kVA

The 15 kVA requirement, much greater than is necessary, made it difficult to supply power at AC 110 single phase. The switchboard was modified to replace the AC 100V, single phase requirement with AC 208, 3 phase power.

The power supply unit houses the power supplies, controllers, timers, and relays used to convert wall power to the necessary voltage and current required by the various pumps, blowers, igniters, etc. The power supply unit includes 10 power supplies. The control computer sends a voltage signal to the power supplies indicating the voltage level for the respective component. A variable voltage, variable frequency controller is used to control the speed of the coolant pump. In addition, the transformers and control circuitry for the two burner igniters are also housed in the power supply unit.

The step-up chopper allows the fuel cell system to operate in a hybrid arrangement as shown in Figure 3-4. The fuel cell system is operated in parallel with a lead acid, 180-volt nominal battery pack. The step-up chopper converts the fuel cell stack DC power to the voltage and current required from the given circuit. For the case of low load (high resistance in the load bank), part of the chopper output power will charge the battery pack. For the case of high load (low resistance in the load bank), the battery pack will discharge, and both the battery power and the chopper power will be dissipated in the load bank. The chopper constantly adjusts the voltage and current to maintain the system balance.

Control Subsystem

The control system consists of a personal computer and data acquisition input/output unit. The specifications are listed in Table 3-4.

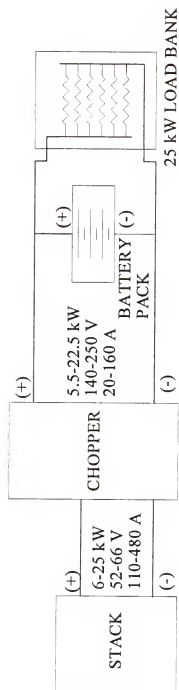


Figure 3-4: Fuel cell battery hybrid power arrangement.

Table 3-4: Control equipment specifications.

Component	Subcomponent	Description
CPU Unit	PC-9801UX21	16 bit personal computer Nihon Electric Co. i80286 3.5" floppy drive JIS keyboard
	Monitor	PCKD-854N
	Operating Software	Japanese MS-DOSV3.3
	Control Software	Floppy disc
Data Acq/Control Unit	Expansion Box	PC-BOX16
	A/D converter board	12 bit, 16 channel
	D/A converter board	two 12 bit, 4channel one 12 bit, 2 channel
	Relay board	two 8 channel
	Digital inputs	one 32 channel board

The control system and control logic is elementary. The control software is written in Japanese ladder logic, and it and the operating system software fit onto one 3.5" floppy disc. The control signals are limited to approximately 18 analog inputs, typically temperatures, and 32 digital inputs, typically component status signals. The data is not logged, as the computer does not have a hard drive. For data acquisition, a separate computer or strip chart recorder was required.

Fuel Cell Engine Operation

The following section briefly describes the fuel cell system operation. The start-up, normal operation, and various shutdowns are detailed.

Start-up

Start-up consists of all the steps required to move the engine from a cold, dormant state into a power generation mode. When the system is off, all the power electronics are shutdown. No pumps, blowers, etc. are operating. The various components are cooled to room temperature. The one exception is the fuel cell stack,

which must be maintained above 45°C to prevent the phosphoric acid electrolyte from freezing. The stack temperature is maintained by placing heating blankets under the stack insulation which are operated from 110 volt wall power. In addition, problems can occur if air leaks into parts the system, such as the reformer catalyst bed. To prevent this, a low-pressure CO₂ purge is utilized when the system is not operational.

Start-up mode 1 raises the temperature of the main components (specifically the catalysts) to their operating level. The stack operates at 150°C and the reformer catalyst bed operates between 250-300 °C. Methanol pump P-04 and blower FAN-02 provide fuel and air to start-up burner. The combustion product flows across the fins of heat exchanger HX-03. The coolant circulates through the tubes of HX-03 receiving energy from the combustion gas and then flows into the stack where it transfers energy to the stack to raise its temperature to 145 °C.

Operating burner B-01 raises the reformer bed catalyst temperature to between 200-280 °C. Methanol pumps P-03 and P-05 and blower FAN-01 provide the fuel and air for burner B-01, respectively. The combustion product flows across the walls of the catalyst bed, transferring energy into the bed. The heating results in temperature gradients within the catalyst bed. To minimize the catalyst bed temperature differences, the burner is operated for 5-10 minutes and then shutdown for 5-10 minutes, thus allowing the different bed temperatures to equalize. It takes approximately 25-30 minutes to complete mode 1.

In start-up mode 2, the methanol and water fuel mix is passed over the reformer bed catalyst and the mixture is reformed into a hydrogen rich gas known as reformat. Under normal operation, the reformat is piped to the stack anode electrode. In start-up

mode 2, the reformat flows through the bypass line directly to the reformer burner. This is done to allow the reforming process to stabilize and prevents poor-quality reformat (high CH_3OH , low H_2) from entering the stack. Pump P-05 is turned off, and reformat and methanol from P-03 are utilized as reformer burner fuel. The reformer catalyst bed temperature is increased and allowed to stabilize during this start-up mode. Start-up mode 2 takes between 2-9 minutes to complete.

In start-up mode 3, the reformat is passed through the stack anode electrode. Blower air from FAN-201 is sent through the cathode electrode. An open-circuit voltage check is performed to ensure hydrogen and oxygen are available to the stack electrodes. If the voltage is greater than approximately 0.8 volts per cell, internal heaters H-01 through H-04 are turned on to provide an electrical load for the fuel cell stack. The system is allowed to stabilize with the fuel cell stack producing approximately 6-6.5 kW. If all parameters (temperatures, voltages, etc.) remain within bounds, the system completes the start-up cycle. Start-up mode 3 takes between 2-4 minutes. The overall time for start-up is between 33-45 minutes.

Normal Operation

During normal operation, the fuel cell stack produces between 6-26 kW. As the stack current load decreases (resulting in lower power output), the individual cell voltages increase. If the cell voltage is too high, corrosion and other degrading factors are accelerated. Thus the minimum output from the stack is controlled to 6 kW to prevent high cell voltages.

Under normal conditions, the stack power is converted in the step-up chopper and dissipated by the load. There are situations where the load does not require power

from the chopper, but the fuel cell system is not intended to be shutdown. In this case, the chopper is taken off-line and heaters H-01 through H-04 dissipate the stack power. This is called the idle condition. The stack power output is controlled by a user-controlled 0-10 volt (representing 0-100%) signal inputted to the control computer. If the signal is below 2.5 volts (25% or 6 kW), the system enters idle mode.

The control logic for normal operation is fairly simple. The control computer attempts to maintain various system parameters within set limits. The parameters include temperatures, pressures, and voltages. The transient response of the system is slow, taking about 7 minutes to increase power from 6 kW to 25 kW. Another example of the control logic is how the system maintains the stack temperature by controlling the stack coolant inlet temperature. At 7 kW stack power output, the stack inlet coolant temperature is maintained between 145-155°C. If the coolant temperature drops to 145°C, methanol and air are added to the start-up burner to raise the coolant temperature using HX-03. At higher power outputs, if the stack coolant inlet temperature is too high, air is blown across HX-03 to remove energy and lower the coolant temperature.

Shutdown

There are the following three types of system shutdown: normal shutdown, emergency ES-1, and emergency ES-2. During a normal shutdown, the system enters the idle mode. The stack produces power, but the internal heaters H-01 through H-04 dissipate the stack power. The methanol flow rates to the two burners are minimized, and the system is allowed to slowly cool. The goal is to slowly lower the system temperatures before complete shutdown to minimize damage (typically catalyst

degradation) due to thermal gradients. Once the system has sufficiently cooled, all fuel flow is stopped and the blowers are operated for approximately 5 minutes to further cool the system. At this point, the CO₂ purge is activated, the system is shutdown, and wall power is turned off.

There are two types of emergency shutdown, ES-1 and ES-2. ES-1 occurs when operating parameters fall outside the acceptable range. Component overheating, loss of burner flame, and high ambient temperature are all examples of ES-1 shutdowns. The system components are still operational, and the goal is to cool the system as slowly as safe operation allows. ES-2 is a catastrophic emergency situation. Hydrogen gas leak, loss of wall power, and control computer failure are examples of ES-2 shutdowns. All the components are immediately turned off and CO₂ purge gas is activated. There is no control of temperatures within the system. Catalyst degradation can occur from thermal gradients and from purge gas being present with hot catalyst. The damage to the system is offset by the need for safety.

CHAPTER 4: EXPERIMENTAL METHOD

Instrumentation and Data Acquisition

Introduction

The objective of this research was to investigate and inventory the efficiency and emission characteristics of the brassboard 25 kW phosphoric acid fuel cell engine. Therefore a comprehensive understanding of the engine was clearly required. The existing control strategy had to be carefully defined. The various flows in and out of the system had to be analyzed, the performance of various subsystems scrutinized, and their interactions with other subsystems determined. To accomplish this goal, a comprehensive instrumentation and data acquisition system was utilized.

The existing control system does not have data logging capability, primarily because the control computer does not have a hard drive. There are 17-20 signals sent to the control computer that are used exclusively for control purposes. There are other signal sources, such as thermocouples, installed on the system but not tied into any control strategy. These signals are primarily used for debugging purposes. The limited data presented by Fuji characterizing the brassboard was primarily obtained by manually.

The initial instrumentation provided with the brassboard consisted primarily of control signals, other thermocouples, and current shunts. Additional instrumentation

such as thermocouples, voltage and current measurement, flow measurements, and pressures measurements were added to the system. A data acquisition system was procured and acquisition software was developed.

Control Signals and Strategy

The existing control strategy can be broken down into the following parts: the incoming signals detailing the state of the system; the analysis and control logic including parameter limits; and the resulting output changes to control components such as pumps and blowers. To understand the control strategy, all parts of the strategy had to be understood. The incoming signals had to be recorded and analyzed. The resultant control changes, such as pump voltages, also had to be recorded and analyzed. And finally, by comparing the incoming and outgoing control signals, the control strategy or logic was reversed engineered.

The incoming signals incorporate 17 analog signals and approximately 16-32 digital signals. The fuel cell system is an electrically noisy system and to prevent problems with the signals, the 17 analog signals pass through isolators. The isolators are necessary for the following reasons:

- to eliminate problems associated with electrical noise (spurious signals)
- to allows averaging of the input signal
- to convert the various transducers signals to a common 0-10 volt signal
- to provide isolation between the system and the control

The analog control signals include temperatures, stack voltage, and stack current. Table 4-1 lists the analog control signals. To properly understand the system operation, the control signals were datalogged. This was accomplished by tying into the 0-10 volt

isolator output signal. The data acquisition system required 16 analog input channels of 0-10 volts.

Table 4-1: Analog input control signals.

Designation	Description	Input	Output
TA-101	Reformer bottom catalyst bed temp.	0-500 °C	0-10 V
TCA-102	Reformer middle catalyst bed temp.	0-500 °C	0-10 V
TI-103	Reformer superheater temperature	0-500 °C	0-10 V
TA-104	Reformer top catalyst bed temp.	0-500 °C	0-10 V
TC-105	H-05 temperature	0-500 °C	0-10 V
TA-201	Start-up burner temperature	0-1000 °C	0-10 V
TA-202	Reformer burner temperature	0-1000 °C	0-10 V
TA-203	Reformer burner temperature	0-1000 °C	0-10 V
TA-205	HX-03 inlet surface temperature	0-500 °C	0-10 V
TA-206	Ambient air temperature	0-300 °C	0-10 V
TCA-401	Stack coolant inlet temperature	0-300 °C	0-10 V
TA-402	Stack coolant outlet temperature	0-300 °C	0-10 V
TCA-403	Stack temperature	0-300 °C	0-10 V
IFC-01	Stack current	0-60 mV	0-10 V
IFC-02	Stack current	0-60 mV	0-10 V
VFC-02	Stack voltage	0-100 V	0-10 V
VFC-02	Stack voltage	0-100 V	0-10 V
Power	Power level user input	0-10 V	

The digital signals are primarily status signals, such as limit switches within the fuel tank. The control system monitors these signals and shuts the down the system if there is a problem. If a problem occurs, the control system informs the user of the source of the problem. Therefore, it was not necessary to monitor the status signals.

The control system has as inputs the above signals, determines the state of the system, and responds by changing parameters within the system. The parameters that are altered include pump and blower voltages, solenoid valves are open/closed, and current load is increased or decreased. The values changed by the control logic were consequently logged in order to determine the control logic. Table 4-2 lists control

output signals that were monitored. Most of the digital outputs such as solenoid valves opening and closing are related to the above signals. For example, solenoid valve SV-04 opens when P-04 is operating, thus the status of SV-04 can be inferred from the P-04 voltage.

Table 4-2: Analog output control signals.

Designation	Description	Range
P-01	Main methanol pump voltage	0-30 V
P-02	De-ionized water pump	0-30 V
P-03	Reformer methanol trim pump	0-30V
P-04	Start-up burner methanol pump (on/off)	0-24 V
P-05	Reformer methanol start-up pump (on/off)	0-24 V
Fan-01	Reformer burner blower	0-100 V
Fan-02	Start-up Burner/HX-03 blower	0-100 V
Fan-201	Fuel cell stack blower	0-100 V
H-05	Heater H-05 voltage	0-100 V
SUC V	Step up chopper voltage	140-250 V
SUC I	Step up Chopper current	0-300 °C
TCA-401	Stack coolant inlet temperature	0-300 °C
VFC-02	Stack voltage	0-100 V

The requirements for interfacing the data acquisition system were more difficult in monitoring the output control signals. Typical data acquisition systems read 0-5 or 0-10 volt analog signals. To monitor 0-100 volt signals, voltage dividers or special equipment is necessary. In addition, many of the signals and power voltages are floating, therefore requiring special needs in channel-to-channel and channel-to-chassis isolation.

Once the data in Tables 4-1 and 4-2 have been logged, it was possible to determine the control system logic. For example, by comparing the voltage of P-03, the reformer burner trim pump, to the catalyst bed temperatures the control logic for pump

P-03 can be reversed engineered. By working through the various signals under different operating conditions, the component and overall control strategy was determined.

Temperature Measurement

To properly analyze the fuel cell system, other parameters in addition to control signals were required. The temperatures of various flows within the engine were needed to determine their thermodynamic states. Existing thermocouples were utilized and additional thermocouples were installed. A list of the required thermocouple data is shown in Table 4-3. The existing thermocouples are k-type thermocouples, which were chosen because of their wide temperature operating range (0-1370 °C).

Pressure Measurement

The brassboard fuel cell engine operates at approximately atmospheric pressure. The pressure drops within the engine are typically low. The three blowers deliver air with maximum outlet pressures of 10-12 inches of water (" of H₂O). The main methanol and water pumps (P-01 and P-02, respectively) have outlet pressures below 5 psi. The other fuel pumps, however, deliver methanol through burner spray nozzles. These pumps (P-03, P-04, and P-05) deliver fluid pressures up to 10 atmospheres. Pressure gauges were installed at the outlet of all methanol pumps, water pumps, and air blowers. Because many of the pumps and blowers typically operate at only a few discrete flow rates, retrieving some pressure data manually from gauges was acceptable.

Flow Measurement

It was critically important to measure the fluid flows in and out of the system.

There are four methanol pumps, one water pump, three air blowers, and three exhaust lines. The liquid flows were measured using Fluidyne 1240T fuel flow transducers. The

Table 4-3: Additional thermocouple data.

Description	Range
Ambient temperature	
Reformer burner air temperature	0-40 °C
HX-01 fuel outlet temperature	0-150 °C
Reformer fuel mix inlet temperature	0-150 °C
Reformate temperature (reformer exit)	0-300 °C
Reformer burner fuel temperature	0-200 °C
H-05 vaporizer exit temperature	0-150 °C
H-05 vaporizer temperature	0-150 °C
Reformer exhaust temperature	0-350 °C
HX-03 inlet surface temperature	0-300 °C
HX-03 outlet surface temperature	0-300 °C
HX-03 exhaust temperature	0-300 °C
HX-03 inlet coolant temperature	0-200 °C
HX-03 coolant inlet temperature	0-200 °C
H-01 coolant outlet temperature	0-200 °C
H-04 coolant outlet temperature	0-200 °C
Fuel tank surface temperature	0-100 °C
Reformer surface temperature 1	0-100 °C
Reformer surface temperature 2	0-100 °C
Fuel cell stack surface temperature	0-100 °C
Fuel cell cathode exhaust temperature	0-200 °C
Reformer burner temperature	0-1000 °C
Reformer catalyst temperature	0-400 °C
Reformer fuel inlet temperature	0-200 °C
Stack temperature	0-200 °C
Stack fuel outlet temperature	0-200 °C
Stack air outlet temperature	0-200 °C
Stack coolant inlet	0-200 °C

meter was calibrated using spare fuel pumps, and the results were in close agreement to the factory specifications.

Three of the pumps are magnetically-coupled, positive displacement gear pumps. The motor rpm is linear with the applied voltage. The positive displacement pump delivers a constant volume of fluid per revolution, assuming low to moderate outlet pressures. Therefore, the volumetric flow rate is approximately linear with the motor voltage. The fuel flow meter was connected to the methanol pumps P-01 and P-03 and calibration curves for the flow rate versus motor voltage. In this way, by measuring the pump voltages, the fuel flow rates were calculated. The results of the calibration tests were consistent and in agreement with curves provided by the brassboard manufacturer.

The other two fuel pumps, P-04 and P-05, are solenoid pumps. The pumps are digitally operated, either on at one speed or off. The fuel flow meter was connected and the flow rate for each pump was measured.

Air flow measurement was accomplished using a Superflow 4" and 6" air turbines. The air turbines are part of the Superflow SF-901 engine dynamometer. The turbines were modified to fit onto the inlet of the three air blowers. As air is drawn across the turbine impeller, a pulsed signal is outputted. By measuring the frequency, the volumetric airflow can be calculated.

The air turbine was connected individually to the three blowers. The system was operated at different power levels, and the air flow was measured and compared to the blower motor voltage. The frequency output from the air flow meter was a consistent and repeatable function of the blower motor voltage. By utilizing the manufacturer calibration curves for the air flow meter, the air flow rate for each blower can be inferred from the blower motor voltage.

The flow rates from the three exhaust lines were calculated. The reformer burner exhaust flow rate is the combustion product of burner B-01. HX-03 exhaust is either the flow rate of air from blower Fan-02 (cooling mode) or the combustion product of burner B-02 (heating mode). Finally, the stack cathode exhaust is the flow rate of air from Fan-201 corrected for the oxygen consumed at the cathode electrode and the water produced at the cathode electrode. Both the reduction in oxygen and the addition of water are directly related to the stack current.

Parasitic Power Measurement

The parasitic power consumption of fuel cell systems has a significant impact on system efficiency. For pressurized systems, the parasitic power can be 20-25% of the design power output. For low-pressure systems, the parasitic power can be 8-10% of the design power output, even a greater percentage at off-design (reduced) power levels

For the brassboard system, the parasitic power is delivered from 208 V, three phase wall power. The power is delivered from two circuits, one primarily for the coolant pump P-401 and the other primarily for the power supplies that deliver DC power to the pumps and blowers. The wall power is delivered to the switchboard where it is distributed throughout the engine.

The wall parasitic power was measured using Load Controls PPM-1 three phase power meter. The power meter connections include three clamp meters for current sensing and four alligator clips (including neutral) for voltage sensing. The connections were made at the input terminal strip within the switchboard. The full-scale power is selectable, and the power meter sent a 0-10V or 4-20 mA signal based on the percentage

of full power. Table 4-4 details the data for the air flow, fuel flow, and parasitic power meters.

Table 4-4: Additional brassboard data.

Description	Signal Type	Range
Fuel flow meter	Frequency	0-1000 Hz
Air flow meter	Frequency	0-500 Hz
Parasitic power meter	Analog	0-10 Volts

Gas and Liquid Analysis

Liquid reformat component analysis

The reformat composition has a strong bearing on the efficiency of the engine. The goal of the steam reformer is to convert the methanol-water mixture into a hydrogen rich gas. Hydrogen production is maximized when a high percentage (>99%) of the methanol has been consumed by the reforming reaction. Therefore, measuring the percent conversion of methanol is an indication of the performance level of the reformer. In addition, some reformat constituents such as carbon monoxide have a detrimental effect on the performance of the fuel cell stack. The reformat composition must be determined to properly analyze overall fuel cell engine performance.

A 1/4" copper tube was connected to the reformat line between the outlet of the reformer and the inlet of the stack anode electrode. The copper sampling tube was bent in a coil arrangement and placed in an ice-water bath. Valves in line were used to adjust the flow rate of reformat through the sample tube. As the reformat gas flowed through the tube, the water and methanol were condensed out of the stream and collected. The remaining dry constituents of the reformat gas were either vented to atmosphere or collected in sampling bags for analysis on the gas chromatograph.

By measuring the density of the water and methanol solution condensed from the reformat stream, the percent conversion of methanol was determined. The resulting fraction of methanol in the condensate is compared to the original fraction of methanol in the fuel mixture to determine the percent conversion. This is a typical method for analyzing the methanol conversion level. The brassboard steam reformer, however, is fully integrated into the fuel cell engine which makes it difficult to acquire enough water and methanol from the reformat to make an accurate density reading (without specialized equipment) without causing difficulties for the engine.

To overcome this problem, the testing of the reformat methanol and water was done by nuclear magnetic resonance (NMR) testing. Small liquid samples of only 3-5 milliliters are required. NMR testing is based on the premise that the overall spin of a charged nucleus generates a magnetic dipole along the spin axis. By comparing the NMR results of a known quantity to the condensed reformat sample, the level of unreacted methanol was determined. Initial testing showed very good accuracy, usually within $\pm 0.2\%$.

Gas reformat analysis

A gas chromatograph was used to determine the composition of the dry reformat gas. Sampling bags were used to collect the dry reformat at the outlet of the sampling tube. The SRI 8610C gas chromatograph (GC) was used to analyze the gas composition. The flame ionization detector (FID) is typically used for hydrocarbon analysis. By using the FID, low concentrations of 1 ppm can be measured. In addition, the GC utilizes a methanizer to catalytically reduce carbon monoxide and carbon dioxide to methane over a nickel-packed bed. Converting the CO and CO₂ to methane

allows very small concentrations of either gas to be measured by the FID. Numerous sample gases of known concentrations typical of methanol steam reformed reformat were used to calibrate the GC.

Emissions Testing

The brassboard fuel cell engine has the following three exhaust lines: stack cathode exhaust, the HX-03 exhaust, and the reformer exhaust. Previous engine testing showed that no detectable regulated emissions were present in the cathode exhaust [63]. This is expected since the only reactions that are occurring is the electrochemical reduction of oxygen at the cathode electrode and the production of water. When burner B-02 is operating, regulated emissions are detectable in the HX-03 exhaust. The flow rate of methanol and air are constant in the burner B-02, and the emissions are low [63]. The majority of the regulated emissions occur in the reformer exhaust. During start-up, both liquid and vaporized methanol is burned in burner B-01. During normal operation, varying levels of hydrogen rich gas combined with varying levels of vaporized methanol are burned in burner B-01. The air flow into the burner remains constant during operation. The emissions exiting the reformer are not constant, but vary with changing conditions within burner B-01.

The data for the fuel cell engine emissions is obtained from the following three sources: gas chromatograph analysis of exhaust samples; continuous emissions monitoring from COSA 6000 HC engine emission analyzer; and the fuel cell bus emissions testing. Sample ports were installed on the HX-03 exhaust and the reformer exhaust. Sample bags were used to acquire samples of the exhaust gas. The samples

were analyzed using the SRI 8610C gas chromatograph. These samples analyzed the CO, CO₂, O₂, N₂, CH₄, and higher hydrocarbon content of the exhaust gases.

The emissions from the fuel cell engine are not constant, even at steady-state power output [63]. Therefore, to better analyze the emissions, continuous monitoring is required. The COSA 6000 HC emission analyzer was connected to the exhaust sampling ports. The exhaust gas first passes through a drier (IMR 5000) to eliminate the high water content from the sample stream. The COSA 6000 HC analyzes the O₂, CO, NO, and NO₂ levels in the exhaust stream on a continuous basis. The results from the emission analyzer are compared to the GC results to provide verification of the results.

During the spring of 1997, the University of Florida was involved with the emission testing one of the three DOE/DOT fuel cell/battery hybrid buses. The 50 kW fuel cell engine is the same design and manufacturer for the 25 kW brassboard engine. The testing occurred at the West Virginia University Transportable Heavy Duty Vehicle Emissions Testing Laboratory. The laboratory includes a fully transportable chassis dynamometer, exhaust dilution tunnel, and real-time emission measurement equipment. Testing included fuel cell engine steady-state power output, fuel cell engine transient power output, and overall vehicle performance over defined routes such as the central business district (CBD). The results of the bus engine testing are included for comparison and with the data from the brassboard fuel cell engine.

Data Acquisition System

The goal of a data acquisition system was to record a signal or signals that represent physical parameters of interest. Computer-based data acquisition has become the primary method of data acquisition. Advantages of computer-based data acquisition

systems include the following: flexibility to add a variety of different sensors; the ability to manipulate and view data in real time; and the data can be recorded directly into a useable form such as a spreadsheet file.

The basic structure of any computer-based data acquisition system includes the following:

- sensing transducers that output a signal (voltage, current, etc.) that represents a physical parameter
- signal conditioning (such as amplification) to provide high-quality signals
- analog-to-digital conversion of input signals to digital bits that a computer can understand
- operator interface through software
- data reduction and analysis.

Computer-based systems have improved dramatically over the past years and much of the signal conditioning, multiplexing, and analog-to-digital conversion occurs with minimal effort. The software has also undergone significant improvements, allowing the user the ability to manipulate numerous signals in real time.

Hardware

The University of Florida developed the data acquisition system for the DOE/DOT fuel cell/battery hybrid bus program. The hardware requirements for the project included a portable system, interface with a laptop computer, flexibility to encompass a variety of transducers, and reasonable cost. The system chosen was the IOtech Daqbook 200 portable data acquisition unit. The Daqbook unit interfaces with the computer through the parallel port, making it easy to transfer between applications.

The Daqbook 200, with the use of expansion cards, can read a variety of transducers.

The system worked well for the bus application and was chosen for the brassboard system as well. Figure 4-1 incorporates the transducer signals to the brassboard schematic

The specifications for the Daqbook 200 are listed in Table 4-5.

Table 4-5: Specifications of the Daqbook 200.

Parameter	Specification
A/D resolution	16 bit
analog input channels	16
maximum channel capacity	256
Analog output channels	2
A/D output resolution	12 bit
High-speed digital inputs	16
Digital input/output lines	24
Programmable counters/frequency	5

The Daqbook 200 is the base unit that includes the above channels plus all the multiplexing and analog-to-digital conversion. To provide maximum flexibility, expansion cards and modules are available to interface with nearly any type of sensor. The required signals are listed in Tables 4-2, 4-3, 4-4 and 4-5. Table 4-6 lists the expansion cards included in the brassboard data acquisition system.

The IOtech data acquisition system is very powerful and flexible. Typically, to directly record the stack and chopper voltages would be difficult, requiring signal conditioning. The high voltages as well as problems associated with floating voltages would require the user to employ voltage dividers and isolation devices before the signal is recorded. Both devices add error and interface problems. However, IOtech the DBK 50 module allows direct connection to the signals which in turn improves accuracy and response time.

Software

The data acquisition software provides the user interface with the data acquisition system. The software should allow the user to view and manipulate the data in real-time and record the data directly into a usable form, such as a spreadsheet file. For the DOE/DOT fuel cell bus program, Labview software from National Instruments was chosen. For the brassboard data acquisition system, both Labview and IOtech's Daqview were used.

Labview from National Instruments is a general-purpose programming language, but includes libraries of functions and development tools designed specifically for data acquisition and instrument control. It is a graphical programming language rather than a text-based language. Icons are used to represent functions and "wires" are drawn between icons to represent interaction. Labview allows real-time manipulation of the data giving the user instant access to the state of the engine. In addition, graphical manipulation provides the user trends within the engine.

Daqview is the data acquisition software provided by the hardware manufacturer. As a result, interfacing the hardware and software is seamless. Daqview is written in Visual Basic, and the user manipulates the software through pull-down menus and point-and-click operations. Daqview is not as powerful as Labview, but due to the seamless interfacing it provided a greater throughput of signals. A large throughput of signals was necessary due to the large number of signals combined with the need to average numerous readings due to electrical noise. As a result, Labview was used to gain a better knowledge of the engine operation and Daqview was used to compile large sets of data.

Brassboard Test Plan

The goal of the test plan was to best utilize the data acquisition system to develop a comprehensive understanding of the fuel cell engine. The brassboard fuel cell engine was operated over a period of time in order to learn the basic engine behavior including how and when various pumps were operated; the effects of interaction between the diverse engine components within the engine; and basic efficiency numbers. Various characteristics of the control strategy and the engine performance were learned.

After the engine basics had been learned, the data acquisition system underwent a thorough debugging process. The accuracy of the data acquisition analog readings was determined. The data acquisition thermocouple values were compared to those achieved using various handheld multimeters. Poor responding thermocouples were replaced. The location of the power meter connections was verified. The wiring for the air flow meter was replaced and the frequency reading verified. The gas and liquid sampling system was improved and proper operating procedures to collect and sample the fluids were developed. Calibration tests were performed on the fuel pumps.

Once the integrity of the data acquisition system had been established, the fuel cell engine underwent further testing to determine the completeness and of the acquired data. Spreadsheet models were developed that analyzed various flow streams within the engine. Adiabatic combustion temperatures were calculated as an additional check to determine if the air and fuel flow rates were accurate. Energy balances were performed on numerous components to ensure signal accuracy. Finally the efficiency values were calculated to determine what engine operating points were necessary for evaluation. At

this point, more thermocouples and other sensors were installed to complete the data acquisition system.

The engine was then operated at a variety of steady-state power outputs providing the data that form the basis of the data for this dissertation. The minimum operational power output from the engine was 6.5 kW, or approximately 25% of design power. The maximum power output from the engine was limited by the fact that the engine aged, its performance degraded. A rule of thumb for phosphoric acid fuel cell systems is to not allow the cell voltage to drop below 0.6 V/cell. If the voltage drops too low, the system can undergo unstable operation, where increasing the current actually reduces the power output. For the brassboard engine, 0.6 V/cell was achieved at 18-20 kW output, or approximately 75-80% of original design power. The nominal steady state operational points chosen were the following: idle, 25%, 37.5%, 50%, 62.5%, and 75%. These data points should provide a comprehensive map of engine performance.

At each of the steady-state operating points, various thermodynamic (temperatures, pressures, flow rates, etc.) data was collected. The COSA emission analyzer was connected to the reformer exhaust and, at low power outputs, to the HX-03 exhaust. Reformate samples were taken at various power outputs. NMR testing was performed on the condensed methanol and water. Gas chromatograph testing was performed on the dry reformate. A power meter was connected to both 208 volt, three phase wall power connections for accurate measurement of all external energy inputs.

Start-up and shutdown tests were run. The control strategy, fuel use, and parasitic power consumption were monitored and the resulting energy penalty

associated with starting the system was analyzed. The emission levels were analyzed in both the HX-03 exhaust and the reformer burner exhaust.

Once the steady-state tests were complete, the system was operated in limited transients tests. The engine takes approximately 7 minutes to increase stack power output from 6 kW to 25 kW (25% to 100% of design power output). Because of this slow rate of power increase change, components within the engine operate in a quasi steady-state. Even though the system is changing stack power output slowly, there is an effect on control strategy and performance. The emission levels were also monitored.

Conclusion

A comprehensive data acquisition system was installed in the engine. The required thermodynamic parameters to understand the energy flow within the engine were available. A test plan was developed to ensure the comprehensive testing of the engine operation envelope. Liquid and gas sampling procedures were developed and incorporated to determine important performance criteria. The result of implementing the experimental method was that the information required to investigate the efficiency and emission concerns of the fuel cell engine was now available.

CHAPTER 5 RESULTS AND DISCUSSION

Introduction

This chapter presents the experimental results from the brassboard phosphoric acid fuel cell engine tests. The test results are discussed with emphasis on efficiency and emissions. The test program included steady-state power tests, limited transient tests, and start-up/shutdown tests. The results are typically presented on the basis of normalized power output (design power output is 25 kW) to allow comparison to other engines. The system was originally designed for 25 kW stack electrical power output but due to aging, degradation, etc. the system has been limited to approximately 20 kW stack electrical power output.

Steady-State Operation

The more significant results of the steady-state testing are presented in this section. The primary purpose of the tests was to quantify the efficiency and emission levels and to isolate the variables affecting the results.

Polarization Curves

The production of electricity occurs from the electrochemical combination of hydrogen and oxygen within the fuel cell stack. The typical method of comparing cells or stacks is the polarization curve, which graphs the voltage versus current. To allow comparison to other stacks, the polarization curve is often normalized with the volts per

cell (volts/cell) graphed versus the current density, often in mA/cm^2 . The polarization curve directly indicates how efficiently the cell or stack is converting hydrogen and oxygen into electricity and water. The higher the cell voltage, the more of the chemical energy that is converted into electrical energy; therefore the more efficient the process.

Figure 5-1 presents the polarization curve for the brassboard fuel cell engine stack. As expected, the shape of the polarization curve for the brassboard operating region is approximately linear. The stack power output is also included on the figure and ranges from 7-21 kW.

Figure 5-2 presents the normalized polarization curve. As a rule of thumb, it is safe to operate a phosphoric acid fuel cell engine at or above 0.6 volts/cell, and therefore the stack power output was limited to 21 kW. At below 0.6 volts/cell, the heat generation is increased and the knee in the polarization curve associated with mass diffusion limitations may be reached.

The average cell efficiency curve is also presented in Figure 5-2, and is defined as the electrical power output divided by the enthalpy of the electrochemical reaction (see efficiency section of literature review):

$$\eta_{\text{CELL}} = nFV/\Delta H_R \quad (5.1)$$

The cell efficiency ranges from 56% at low power to 47% at high power. The efficiency curve is lower at high power due primarily to resistance losses associated with higher currents. The cell efficiency is often stated as the overall fuel cell engine efficiency but this is improper since it only accounts for losses within the stack.

Figure 5-3 presents the available polarization data for the history of the brassboard engine. Fuji presented the 1989 data during engine acceptance tests.

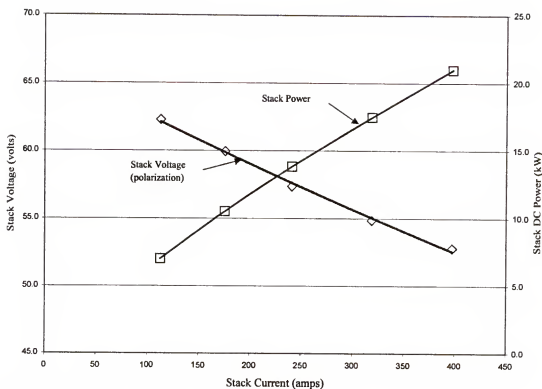


Figure 5-1: Brassboard fuel cell engine polarization curve and stack power output.

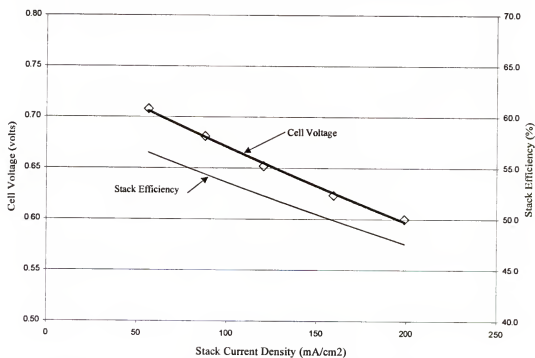


Figure 5-2: Brassboard fuel cell engine steady-state normalized polarization curve and stack efficiency curve.

H-Power Corporation presented the 1992 data during power source qualification testing. The 1999 data is the result of current steady-state testing and shows that the performance of the stack has degraded over the 10 years of operation. It generally takes perhaps 100 hours of operation for a new stack to achieve initial “steady-state” performance, and this may account for some of the reduced performance relative to the 1989 data. As 1989 data may have been acquired before true steady-state performance had been achieved. Other factors that could result in degraded performance include the following [38]:

- excessive operating conditions such as temperature, pressure, voltages, etc.
- the number and types (emergency, etc.) of startups and shutdowns
- operating with open-circuit conditions where the voltage is above 0.8 volts/cell (which leads to increased rate of corrosion)
- starvation of the stack of hydrogen or oxygen, resulting in deviations of cell voltages
- loss of electrolyte, resulting in increased resistance
- degradation of wet-proofing agent, resulting in cell flooding
- large quantities of unreformed methanol entering the stack, resulting in side reactions
- Fuel impurities such as sulfur entering the stack and reacting the the electrolyte

The generally accepted definition of cell or stack life is when the output voltage at rated current has decreased by 10%. If the 1989 data was achieved after the first 100 hours of

operation, the reduction in voltage is approaching 10%, meaning the brassboard fuel cell engine is approaching the end of its life.

The University of Florida received the brassboard fuel cell engine in 1995 and began operation in 1996. During the last four years, the engine has operated on fairly continuous basis. The polarization curves from 1996 and 1999 testing are presented in Figure 5-4. The polarization curve has remained reasonably constant during this time period, and at certain points, the 1999 data is better than the 1996 data. The polarization is not fixed, but can vary significantly with stack temperature, pressure, quality of reformat (anode gas), hydrogen utilization, etc. This can make comparisons of performance data very difficult. The variation in the polarization curve is especially evident for this engine at low power outputs (low current), since stack temperature can vary more significantly than at higher power levels. The variation in performance is shown in Figure 5-4 as the curves deviate at low currents and approach a common value at high current.

Figure 5-5 shows the effect on the cell voltage of changing stack temperature. At 25% of design power output, energy is periodically added to the fuel cell stack through the coolant flow to maintain its temperature. As a result, the stack temperature swings between 158 and 163°C. The stack voltage, in turn, varies from 62.0 to 62.75 volts. The higher stack temperature results in higher voltage and thus higher stack efficiency. The higher stack efficiency comes at the cost of consuming methanol within the startup burner. The effect on overall efficiency of adding the methanol is discussed later in this chapter.

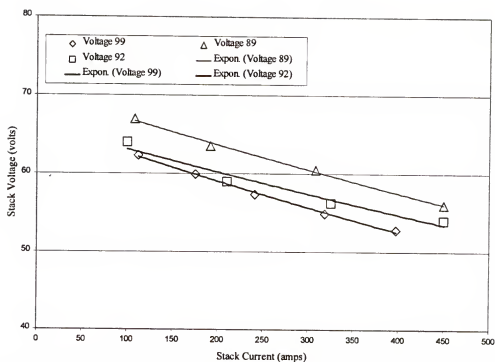


Figure 5-3: Brassboard fuel cell engine polarization curve history since manufacture.

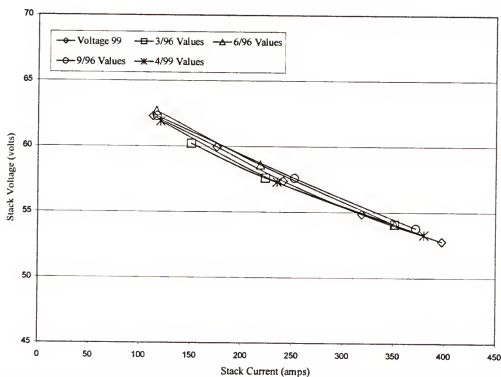


Figure 5-4: Brassboard fuel cell engine polarization curve history while at the University of Florida.

P-01 and P-02 Pump Control

Ideally, the flow of hydrogen into the fuel cell stack anode would be controlled directly. However, measurement of the flow rate of hydrogen gas within the reformat in real time is not practical. Thus the assumption is made that if the steam reformer is operating properly, the flow rate of primary methanol and water is a direct indication of the rate of hydrogen leaving the steam reformer (or entering the fuel cell stack anode). The pumps that control the primary flow of methanol and de-ionized water are P-01 and P-02.

The consumption of hydrogen gas within the stack is proportional to the stack current (I_{FC}). Therefore, the flow rates of the primary methanol and de-ionized water, which determine the flow rate of hydrogen gas, should be related to stack current. A analysis of P-01 and P-02 voltages (which indicate flow rate) as related to stack current resulted in the following linear control equations for representing steady-state operation:

$$P-01 \text{ (volts)} = 0.0469 * I_{FC} \text{ (amps)} + 4.32 \quad (5.2)$$

$$P-02 \text{ (volts)} = 0.0323 * I_{FC} \text{ (amps)} + 3.41 \quad (5.3)$$

Figure 5-6 graphs the actual P-01 and P-02 pump voltages relative to the calculated value. The calculated values are based on the actual voltage during steady-state power (current) operation. When the current is increasing, the actual pump voltage leads the calculated voltage, which indicates extra fuel is available. The increase in methanol flow is intentional and is accomplished to ensure that extra hydrogen is available during transients. The extra hydrogen is needed for two reasons: to ensure that the fuel cell stack anode electrode is not starved of hydrogen and to boost the heat transfer rate into the reformer catalyst bed. Previous modeling has shown that the transient response of

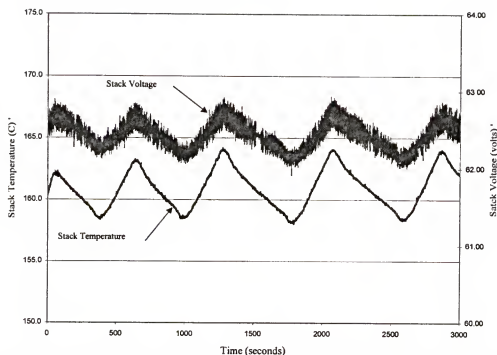


Figure 5-5: Relationship between stack temperature and stack voltage at 25% of design stack power output.

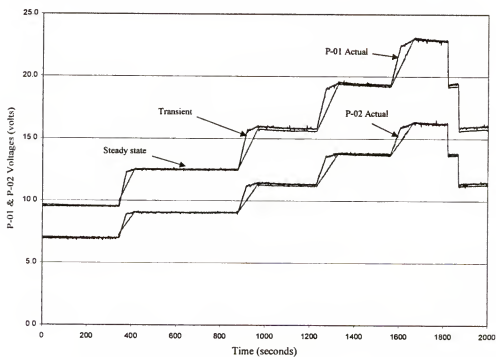


Figure 5-6: Graph of the actual P-01 and P-02 pump voltages versus calculated values.

the brassboard engine is limited by the heat transfer rate into the catalyst bed. The consequences of this boost in fuel flow are discussed in the transient operation section.

A fuel flow meter was utilized to determine the relationship between P-01 voltage and the volumetric flow rate. P-01 and P-02 are identical positive displacement gear pumps, which are designed such that the motor rpm is a function of the applied voltage. For most of the operational range the volumetric flow rate is a direct function of the motor rpm. The results of the P-01 flow rate testing are shown in Figure 5-7. The testing showed a linear relationship between pump motor voltage and flow rate, and compared closely with data provided by the manufacturer of the brassboard fuel cell engine as shown in the Operations Manual. The fuel flow meter manufacturer recommended not flowing water through the fuel meter and therefore the flow rate of the de-ionized water pump, P-02, was tested by weighing a sample collected during a known time period. The results again closely matched those presented by the manufacturer. In addition, the volumetric flow rate of pumps P-01 and P-02 were very similar as expected. The relationship between the mass flow rate and applied motor voltage was determined to be as shown in equations 5-4 and 5-5.

$$\text{P-01 Flow rate (g/min)} = 7.8553 * \text{P-01 V (volts)} - 15.677 \quad (5.4a)$$

$$= 0.3712 * I_{FC} \text{ (amps)} + 17.811 \quad (5.4b)$$

$$\text{P-02 Flow rate (g/min)} = 9.8626 * \text{P-02 V (volts)} - 19.683 \quad (5.5a)$$

$$= 0.3182 * I_{FC} \text{ (amps)} + 13.469 \quad (5.5b)$$

Both the pump voltage and the stack current are measured and recorded, so either of the above equations can be used to determine the flow rate of primary methanol and de-ionized water.

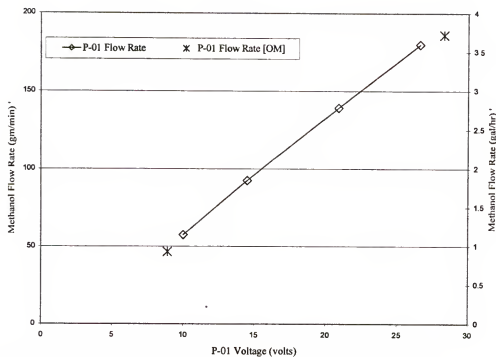


Figure 5-7: Results of pump P-01 methanol flow rate testing at 20°C.

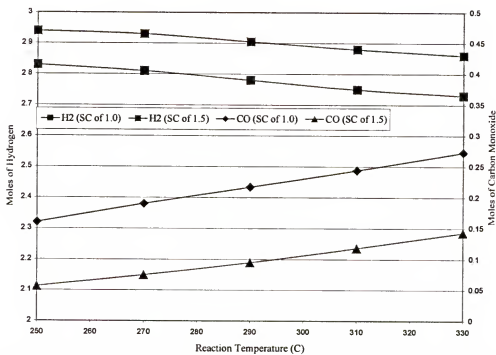


Figure 5-8: Calculated equilibrium mole values of CO and H₂ (per mole of methanol) for methanol steam reforming with steam-to-carbon ratios of 1.0 and 1.5.

The steam-to-carbon ratio (in this case, the ratio of moles of water to moles of methanol) is a design parameter for steam reformers. The ideal reaction for methanol steam reformers (a 1:1 steam-to-carbon ratio) is shown in equation 5-6.



Additional water is used to minimize the carbon monoxide and maximize the hydrogen yield from the reforming process. The advantage of using additional water is shown in Figure 5-8 which displays the results of an equilibrium analysis for methanol steam reforming with steam-to-carbon ratios of 1.0 and 1.5 over a temperature range of 250-330°C and atmospheric pressure. It is important to minimize the carbon monoxide production during the reforming process because it acts a catalyst poison within the fuel cell stack. The downside to using extra water is additional heat transfer requirements and lower partial pressure of hydrogen (excess moles of steam) in the fuel cell stack.

Typical steam-to-carbon ratios for methanol steam reformers range from 1.3-1.5, and manufacture documentation lists the brassboard steam-to-carbon ratio as 1.5. The results of pumps P-01 and P-02 flow meter testing are shown in Table 5-1.

Table 5-1: Results of P-01 and P-02 flow meter testing.

Current (amps)	P-01 Voltage	P-02 Voltage	P-01 Flow Rate (lb./hr)	P-02 Flow Rate (lb./hr)	Steam-to-carbon ratio
112	9.6	7.03	7.31	6.07	1.48
175	12.5	9.06	10.19	8.55	1.49
240	15.6	11.2	13.16	11.1	1.50
320	19.3	14.3	16.81	14.3	1.51
400	23.08	17.4	20.47	17.4	1.51

Reformate Quality

The control of the hydrogen entering the fuel cell stack anode is based on controlling the methanol flow rate entering the steam reformer. This control scheme

works if the composition of the reformat entering the stack anode electrode remains approximately constant.

An important performance criteria for methanol steam reformers designed for fuel cell applications is the percent conversion of methanol. If 5-10% or more of the methanol is unreacted in the reformer, damage can occur to the fuel cell stack due to side reactions at the anode electrode. In addition, the hydrogen production is considerably lower and fuel cell stack performance suffers. Equilibrium analysis shows extremely small fractions ($<0.01\%$) of methanol remaining in the reformat.

Equilibrium is typically not achievable in transportation reformers due to size and weight restrictions, but methanol conversions greater than 99% are achievable. The brassboard steam reformer specifications call for greater than 99% methanol conversion at all power levels. Initial acceptance testing of the fuel cell engine showed that greater than 99% methanol conversion was achieved at full power [Booz Allen & Hamilton, 1990 #56]. Testing at H-Power Corporation in 1992 showed greater than 99% conversion up to 75% of design power, but approximately 96-97% percent conversion at full power. The lower conversion indicated that the performance of the reformer had degraded, and the lower conversion percentage would be one reason for the lower stack voltage (Figure 5-3).

Reformer catalyst bed temperature

Maintaining the reformer catalyst bed temperature is critical to the performance of the reforming reaction. Methanol steam reforming is an endothermic reaction. Heat is typically supplied to the reformer catalyst bed by passing hot gas (combustion product) across the outside catalyst bed wall; heat conducts through the wall and into the bed. It

is important to maintain the temperature in all parts of the catalyst bed, and thermocouples were placed in three areas of the catalyst bed (bottom, middle, and top) to monitor the bed temperatures. Figures 5-9 through 5-12 present the catalyst bed temperatures for steady-state stack power outputs ranging from 25-62.5% of design power output.

For 25% and 37.5% (Figures 5-9 and 5-10) of design power, the curves oscillate because the reformer burner trim pump, P-03; is changing its methanol flow rate into the burner. The methanol flow rate changes in order to maintain the catalyst bed temperatures, and the control of P-03 is discussed later in this chapter. At 50% and 62.5% (Figures 5-11 and 5-12) of design power, the curves are relatively constant because the reformer heat transfer is in balance and the pump P-03 remains at its low flow rate.

Typically, low temperature methanol steam reformers require bed temperatures between 240 and 280 °C. The brassboard steam reformer operates at the upper end of the temperature limit, which maximizes the reaction rate. Below 240 °C and the reaction rate slows considerably, and above 300 °C the degradation of the catalyst increases. In addition, as the catalyst bed temperature increases so does the production of carbon monoxide. For all tests, the catalyst bed temperatures were observed to remain between 260 and 300 °C, which resulted in a high percentage of methanol conversion.

Reformate condensate analysis

To determine the quality of the reformate, liquid and gas analyses were utilized. A small portion of the reformate gas was removed from the system and passed through

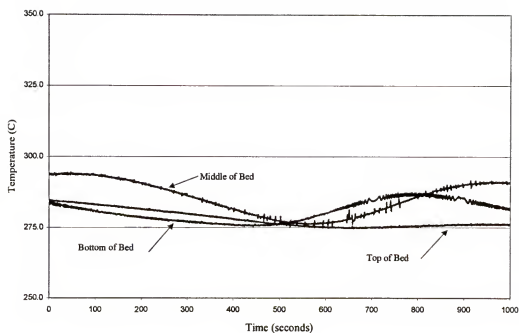


Figure 5-9: Reformer bed temperatures at 25% steady-state power output.

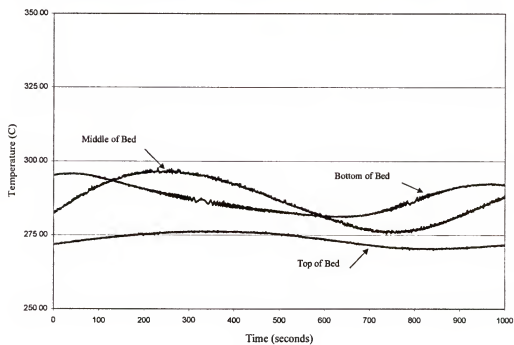


Figure 5-10: Reformer bed temperatures at 37.5% steady-state power output.

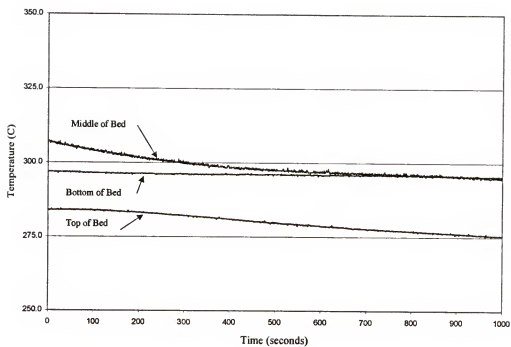


Figure 5-11: Reformer bed temperatures at 50% steady-state power output.

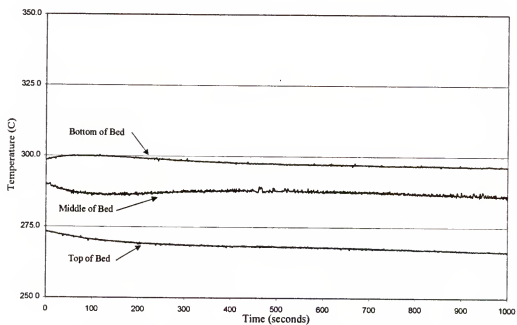


Figure 5-12: Reformer bed temperatures at 62.5% steady-state power output.

a copper coil immersed in a ice bath to condense the water and remaining methanol. The liquid sample was collected and then underwent Nuclear Magnetic Resonance (NMR) testing to determine the methanol content. To verify this procedure, 0.1 molar and 1.0 molar methanol solutions were created and tested using the NMR machine. The test results agreed with the known sample to within $\pm 10\%$. The accuracy is therefore approximately 0.1-0.2%, and therefore this method is quite sufficient to determine appropriate levels of methanol conversion. Table 5-2 lists the results of NMR testing.

Table 5-2: Results of liquid NMR testing.

Sample	NMR Results (molar)	Percent Conversion	Comments
0.1 Molar	0.11	n/a	Good accuracy
1.0 Molar	1.06	n/a	Good accuracy
Startup	3.4	95-96%	Low conversion due to low catalyst bed temperatures
25.0 %	0.121	>99.5%	Good conversion
37.5 %	0.388	>99.0%	Good conversion
50.0 %	1.25	>98.5%	Borderline conversion
62.5 %	2.54	$\approx 97\%$	Questionable conversion, approaching the maximum methanol flow rate
Shutdown/Idle	0.098	>99.5%	Good conversion due to low flow and high catalyst bed temperatures

n/a: not applicable

The percent conversion begins to drop off at 50% of design power. If more than 2-3% of the methanol is unreacted, damage to the fuel cell stack can occur through side reactions at the platinum electrode. Long term operation at above 62.5% of design power output could lead to accelerated degradation of the fuel cell stack anode electrode catalyst.

Reformate gas (non-condensable) analysis

A gas chromatograph was utilized to determine the dry reformate composition. The major constituents of the dry reformate gas are carbon monoxide (CO), carbon dioxide (CO₂), and hydrogen (H₂). The quantities of carbon monoxide and carbon dioxide are determined from the gas chromatograph analysis and the quantity of hydrogen is calculated from species balance. The quantity of hydrogen is calculated due to difficulties in detecting. The thermal conductivity detector (TCD) is used to analyze the levels (>1%) of the dry reformate constituents. The usual carrier gas is helium; however helium and hydrogen have similar thermal conductivities so hydrogen can not be accurately detected with the TCD using helium carrier gas. Nitrogen can be used as the carrier gas, but only with the TCD set to the low current selection which makes low level detection difficult. Thus, helium is used as the carrier gas and CO and CO₂ levels are measured, and hydrogen levels are calculated.

Known sample gas mixtures were procured to calibrate the gas chromatograph. The calibration gases consist primarily of low levels of carbon monoxide (1-4%) and carbon dioxide. Calibration files were developed and the gas chromatograph was shown to provide accurate and repeatable analysis.

A portion of the reformate that passed through the condensing coil was subsequently collected in sample bags. The gas samples were then fed to the gas chromatograph for analysis. The results of the gas analysis showed that CO levels were close but slightly above the calculated values. The reformer bed temperatures ranged from 280-310 °C along the centerline of the bed. However, the temperature of the catalyst bed close to the walls is higher, which may account for the slightly higher CO

levels since increased temperature favors increased CO production. Results of the gas chromatograph testing are shown in Table 5-3.

Table 5-3: Gas chromatograph results for the dry reformat.

Sample	CO levels	CO ₂ levels	H ₂ level (calc)
25.0 %	2.8-3.2 %	22.9-23.7 %	≈ 74%
37.5 %	2-75-2.85%	22.75-23%	≈ 74%
50.0 %	3.1%	23.5%	≈ 74%
62.5 %	2.65-2.75%	22.5-23.0%	≈ 74%

The fraction of hydrogen in the dry reformat remains constant because the water-gas shift reaction occurs quickly. The fraction of hydrogen gas in the overall reformat drops slightly with increasing power output due to the lower conversion of methanol.

Fuel Utilization

Fuel utilization refers to the fraction of the hydrogen gas entering the fuel cell stack anode electrode that is consumed to produce electrical power. There are many considerations when determining the fuel utilization. In most cases, low fuel utilization (<70 %) results in poor overall efficiency since a large fraction (>30%) of the hydrogen is not used to produce electrical power. High fuel utilization (>85 %) in systems that utilize a reformer can cause low cell voltages because of low hydrogen partial pressure. As the hydrogen flows across the anode electrode it is consumed and the its partial pressure drops. If the utilization is very high the partial pressure near the exit of the anode is very low and results in a significant drop in cell voltage.

In addition, most steam reformers are endothermic and much of the required energy comes from combusting the residual hydrogen. If the stack fuel utilization is too low, excess hydrogen is available to the reformer burner, and overheating of the bed can

occur. If the stack fuel utilization is too high, less hydrogen is available for the reformer burner and more methanol is directly used in the reformer burner. Typical system models use 80-85% for the fuel utilization of phosphoric acid fuel cell [69,71,70].

For the brassboard engine, equations 5-4a and 5-4b indicate the primary methanol flow rate for steady-state. Combining this information with the liquid and gas reformat analysis, the quantity of hydrogen delivered to the fuel cell stack anode can be determined. Figure 5-13 graphs the primary methanol flow rate as a function of fuel cell stack current. The curve is linear down to 115-120 amps, just as the equation 5.4b dictates. Below 115 amps, the primary methanol fuel flow rate is constant. This is part of the control strategy and is done to insure there is sufficient hydrogen available at the reformer burner. For the linear portion of the curve, the y-intercept is not zero but rather is considerably above zero. If the reformer is properly designed (catalyst bed temperatures, space gas velocity, etc.), the production of hydrogen is approximately proportional to the flow rate of methanol. The positive y-intercept means that the fuel utilization at low power is lower than at high power.

Figure 5-14 shows the hydrogen production rate, hydrogen consumed, and the fuel utilization for different stack currents. The effect of the offset on methanol flow is that hydrogen utilization is approximately 60% at low current and 80% at high current. From the fuel cell stack point of view, there is no reason that at low current the fuel cell can consume only 60% of the hydrogen. Typically, as long as the fuel utilization is approximately 80%, the effect on cell voltage is insignificant. The reason that the fuel utilization is lower at low current lies with the steam reformer. As discussed earlier, the

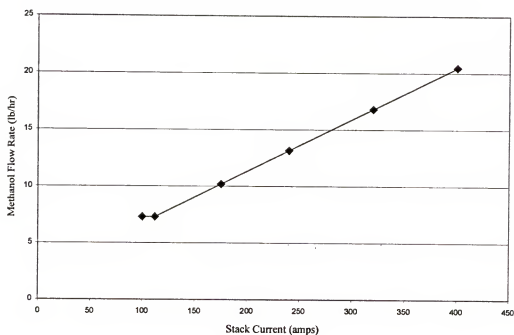


Figure 5-13: Graph of primary methanol fuel flow as a function of stack current.

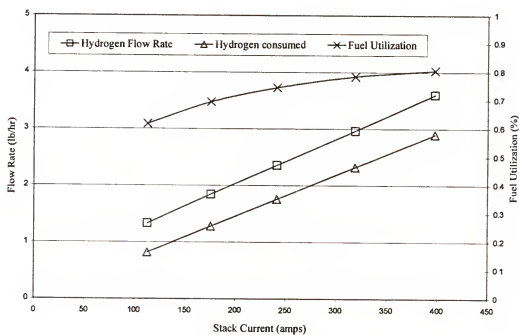


Figure 5-14: Fuel utilization as a function of the stack current.

residual hydrogen is sent to the reformer burner to provide heat energy for the endothermic reforming process. The reformer heat transfer requirements are the driving forces for the shape of the utilization curve at low power levels. Figure 5-15 shows the hydrogen production rate, the rate of hydrogen consumed, and the fuel utilization as a function of stack power output.

Stack Efficiency

The stack efficiency is defined as the stack power output divided by the lower heating value of the reformat entering the stack anode electrode. The lower heating value is used because in the transportation application it is not practical to redeem the energy associated with condensing the steam. Figure 5-16 graphs the stack efficiency versus percent of design power output. The average cell efficiency is also presented for comparison.

The effect of fuel utilization is shown in Figure 5-16. The shape of the stack efficiency curve is quite different from the cell efficiency curve; the cell efficiency is higher at low power while the stack efficiency is lower. The stack efficiency is lower at low power output because fuel utilization is lower which, in turn, is dictated by reformer heat transfer requirements.

Reformer Energy Balance

Modeling of the heat transfer within the steam reformer is complex. The flow of the methanol-water fuel mixture through the catalyst bed and the subsequent heat removal is very dynamic and changes with flow rates and temperatures of the bed. The catalyst bed is typically an annulus arrangement with hot combustion gas passing across the outside walls of the catalyst bed. In addition, the brassboard steam reformer is

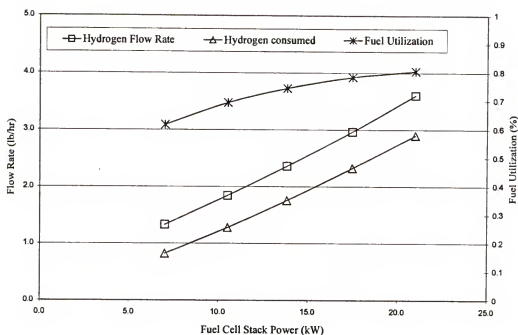


Figure 5-15: Brassboard fuel cell stack fuel utilization as a function of stack power output.

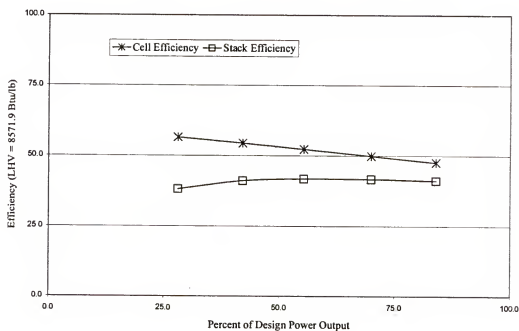


Figure 5-16: Stack and average cell efficiency as a function of percent of design power output.

moderately large and thus the mass has a large thermal capacity and has the ability to store large quantities of energy. The many space and time-dependent variables within the reformer makes detailed modeling beyond the scope of this dissertation.

To approximate the heat transfer within the reformer, a simple energy balance model is employed. The goal of the model is to determine if the heat transfer within the steam reformer is effectively accomplished. Simple overall energy considerations indicate that there should be sufficient energy for the reforming process at fuel utilizations greater than the 60% typically achieved by the brassboard engine at low power. In other words, there is more energy available from hydrogen combusted in Burner B-01 than should be necessary to provide the reformer with heat transfer required.

The amount of heat removed from the catalyst bed is approximately proportional to the primary methanol and de-ionized water mixture flow rate. The liquid methanol and water mixture flows through HX-01 plate-type heat exchanger (see Figure 3-1) where the coolant transfers waste heat from the stack to the fuel mix. For all flow rates, the vaporized fuel mix leaves HX-01 at 145-150 °C. The temperature drops 10-15 °C in the piping between HX-01 and the steam reformer fuel mix inlet. The drop in temperature is due to poor insulation of the line, and required CO₂ purge lines that tie-in. The vaporized (but slightly cooled) fuel enters the steam reformer and passes through the superheater section where it is heated to approximately the catalyst bed temperature. The superheated fuel mix then flows through the catalyst bed where the reforming process takes place. The reforming product gas (reformate) exits the reformer and enters the fuel cell stack anode. Figures 5-9 through 5-12 show that the reformer

bed temperatures are fairly constant and independent of fuel cell stack power output. The temperature of the reformat is approximately the catalyst bed temperature, and therefore approximately constant. Since the temperature of the fuel mix entering the steam reformer and the temperature and composition of the reformat exiting the reformer are similar, the heat removed from the catalyst bed is essentially proportional to the fuel mix flow rate.

Heat is supplied to the catalyst bed from the combustion products of burner B-01. The combustion products first pass over the reformer superheater coil, and then along the walls of the catalyst bed (see Figure 3-3). The fuel mix removes heat from the catalyst bed, and the combustion product transfers heat into the bed. The two flows are in a co-flow arrangement, because most of the steam reforming reaction occurs in the first part of the bed, and thus requires the highest rate of heat transfer. After passing across the catalyst container walls, the combustion product is exhausted to the atmosphere.

Fan-01 delivers air to reformer burner B-01. Although the motor is variable speed, during normal operation the delivered voltage is constant at 80 volts. The air flow testing showed that the airflow into the reformer burner is approximately constant during normal operation at 65 standard cubic feet per minute (scfm). The use of a constant air flow rate is key to some of the problems associated with supplying heat to the reformer catalyst bed. Constant air flow means that a constant flow rate of hydrogen is required for the burner just to raise the combustion temperature to the level of the catalyst bed (280-300 °C). At low power outputs, this quantity of hydrogen is a significant portion of the reformat hydrogen.

Residual reformat (primarily hydrogen gas) and vaporized methanol from P-03 are the fuels for burner B-01. The primary methanol flow rate and the fuel utilization factor determine the quantity of hydrogen available to the burner. Figures 5-14 and 5-15 display the hydrogen flow rate generated by the steam reformer and the hydrogen consumed by the stack. The difference is the hydrogen available for the reformer burner B-01. As expected, the utilization is much lower at low power outputs, primarily due to the constant air flow into the reformer burner.

The control of pump P-03 is discussed in a later section, but it typically operates at a low methanol flow rate of approximately 5-6 g/min. The methanol enters HX-05 (electric heater) where it is vaporized before entering the reformer burner (see Figure 3-1).

Burner B-01 combustion temperature

Because the airflow into burner B-01 is near constant, the combustion temperature is almost proportional to the fuel flow. There is a thermocouple positioned within the burner, but it is primarily used to indicate whether or not there is proper combustion. The flame front moves along the length of the burner based on the type and rate of the burner fuel (liquid methanol, vaporized methanol, hydrogen, or combination). As a result of the moving flame front, the burner thermocouple may be in front of or behind the flame and therefore not measuring the true combustion temperature. The 50 kW transit bus fuel cell system utilizes two thermocouples within the reformer burner to better estimate the combustion temperature. Figure 5-17 shows how the temperature readings change during a start-up cycle where the type (liquid methanol, vaporized methanol, and reformat) and quantity of the fuel flow changes.

The adiabatic combustion temperature was calculated for the steady-state operation and utilized for overall energy balance considerations. The adiabatic combustion temperature is a sensible parameter to use in the energy balance as the burner is inside the reformer, and therefore heat losses to the environment from the burner are minimized. In addition, emissions testing has shown near complete combustion of the fuel.

Figure 5-18 graphs the calculated adiabatic combustion temperature versus stack power output. Typical reformer burner thermocouple readings are also included. The burner thermocouple indicates a higher temperature than the adiabatic combustion calculation because of the non-uniform flame as well as the effect of dilution air. The temperature of the burner increases with stack power output due to increased flow of hydrogen-rich gas into the reformer burner.

Figure 5-18 shows the problem associated with constant air flow into the burner. At low power outputs, the adiabatic combustion temperature is only $\approx 380^{\circ}\text{C}$. The catalyst bed temperatures are $280\text{--}300^{\circ}\text{C}$. The temperature difference is small thus causing low heat transfer rates, and much of the energy of the combustion product is lost as exhaust. As the power increases, the combustion temperature increases to approximately 500°C and the heat transfer is therefore more efficient. The small temperature difference results in the lower fuel utilization at low power outputs.

Reformer exhaust temperature

The flow rate and adiabatic combustion temperature of the reformer burner product are known. To calculate the overall heat transfer rate, the exhaust or rejection temperature was monitored. Figure 5-19 graphs the reformer exhaust temperature and

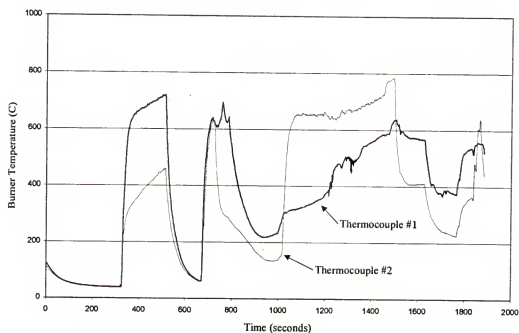


Figure 5-17: Reformer burner thermocouple readings during startup for the 50 kW fuel cell engine.

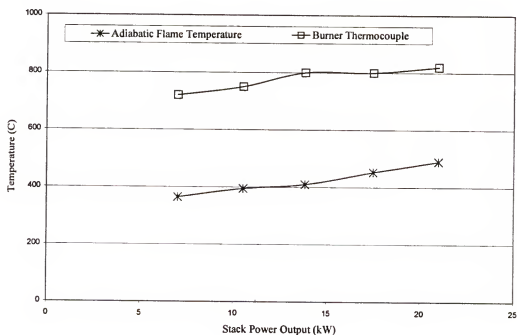


Figure 5-18: Reformer burner thermocouple readings and calculated adiabatic flame temperature as a function of stack power output.

stack power output as a function of time. The graph indicates as the stack power output changes from 25% to 75% of design power output, the exhaust temperature varies from 280 °C to 310 °C.

The exhaust temperature is approximately the same as the catalyst bed temperatures (Figures 5-9 through 5-12). In the case 25% design power output, the exhaust temperature is slightly below the bed temperatures. This indicates that for the given flow rate of air and fuel, the maximum heat is removed from the combustion product. It also indicates that the thermal capacity of the steam reformer is much greater than the required heat transfer.

Figure 5-20 graphs the heat removed by the reforming process, the overall heat transfer, and the excess heat transfer (difference between overall heat transfer and heat removed). The excess heat transfer is due primarily to losses to the environment and to thermal storage within the reformer that the simple heat transfer model cannot account for. The flow rate used for pump P-03 was average flow rate at each operating load. The pump increases the methanol flow rate when the catalyst bed temperature drops.

The graph is very informative. The excess heat transfer is mostly due to heat losses to the environment and because the reformer operates at basically the same temperature independent of power output, the losses should be approximately constant. This is shown by the simple model.

As discussed earlier, low hydrogen utilization by the fuel cell stack results in more hydrogen available at the reformer burner. Modeling shows that nearly all of the hydrogen delivered to the reformer burner at 25% of design power output is required to raise the temperature of the combustion product to 280 °C. Thus the 60% hydrogen

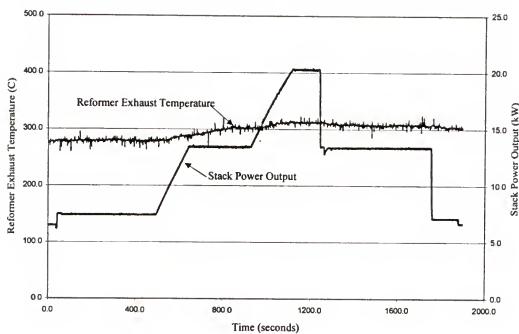


Figure 5-19: Graph of reformer exhaust temperature and stack power output as a function of time for power outputs between 25% and 75% of design power output (25kW).

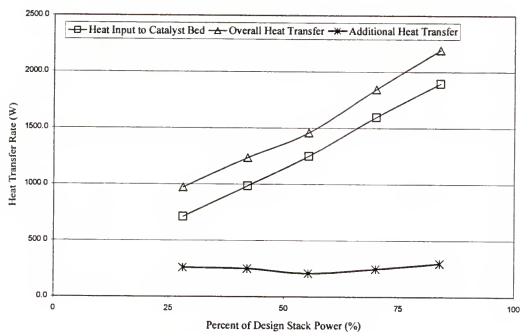


Figure 5-20: The overall heat transfer within the brassboard reformer.

utilization is still too high to provide the sufficient residual hydrogen for the required heat transfer. The additional energy comes from burning 9.1 g/min of methanol.

Reformer Burner Trim Pump P-03

During normal operation, the reformer burner trim pump P-03 is used to maintain the catalyst bed temperatures. Normally, the voltage applied to the pump motor is 5.0 volts, resulting in a flow rate approximately 5-6 grams/minute of methanol. The discharge from the methanol pump passes through a vaporizer heat exchanger, HX-05. The vaporized methanol then enters the reformer burner. If the catalyst bed temperatures fall, the applied voltage is increased and correspondingly the methanol output is increased.

Testing revealed that the middle reformer catalyst bed temperature, TCA-102 controls the P-03 applied voltage, and therefore the fuel flow rate. If the bed temperature falls below 284 °C, the applied voltage is increased according to the following equation:

$$\text{P-03 Applied Voltage (volts)} = 5.0 + [(TCA-102) - 284.0] * 0.8 \quad (5.7)$$

Figures 5-21 and 5-22 show the middle reformer bed temperature and the corresponding applied voltage for 25% and 37.5% of design power output, respectively. From Figures 5-22 and 5-23 (as well as Figures 5-9 through 5-12), controlling P-03 in this manner results in steady and controllable bed temperatures. Table 5-4 lists the primary fuel flow and the average P-03 fuel flow for different stack power outputs.

There is a loss in efficiency associated with using methanol in the reformer burner. The primary methanol fuel flow rate increases with increasing power output, as

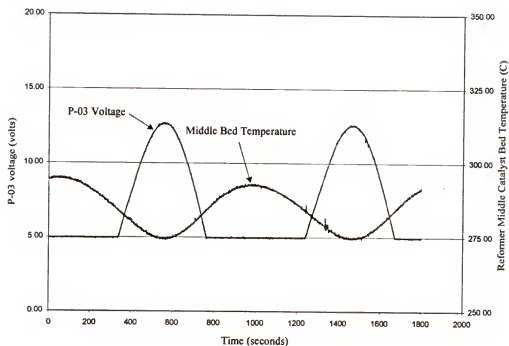


Figure 5-21: Relationship between the middle reformer bed temperature TCA-102 and the P-03 voltage at 25% of design power output.

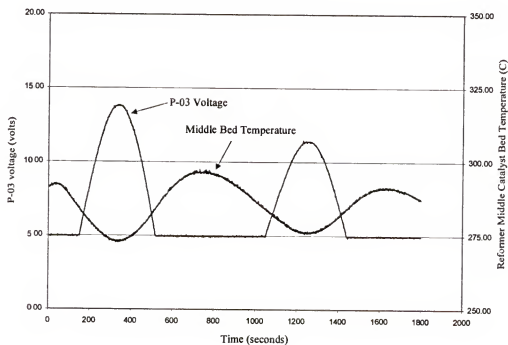


Figure 5-22: Relationship between the middle reformer bed temperature TCA-102 and the P-03 voltage at 37.5% of design power output.

expected. The P-03 methanol flow rate, however, decreases with increasing power output. The net result is that at low power outputs, the loss in efficiency due to fuel from pump P-03 is significant.

Table 5-4: Average methanol flow rates of pumps P-01 and P-03.

Stack Power Output (kW)	Primary Methanol Flow (g/min)	P-03 Methanol Flow (g/min)
7.02	55.3	9.1
10.52	77.0	8.4
13.83	99.5	5.25
17.49	127.1	5.25
20.98	154.7	5.25

HX-05 Vaporizer Heat Exchanger

In addition to the energy associated with the P-03 methanol flow, there are additional efficiency losses associated with the electrical energy used to operate HX-05, the vaporizer heat exchanger. The liquid methanol from pump P-03 enters HX-05 where it is vaporized before entering the reformer burner. The electrical energy used is not trivial, up to 775 watts. The voltage applied to the heating element within HX-05 is controlled by attempting to maintain the temperature (TC-105) at 125 °C. As the voltage applied to P-03 increases, the methanol flow rate through HX-05 increases and the temperature of HX-05 drops. The voltage applied to HX-05 is then increased, and the temperature recovers. Figure 5-23 shows the relationship between HX-05 temperature and HX-05 applied voltage to the P-03 applied voltage. Figure 5-24 shows similar trends but the power consumed by HX-05 replaces the voltage. The effect of the power consumption is discussed further in the section on parasitic power.

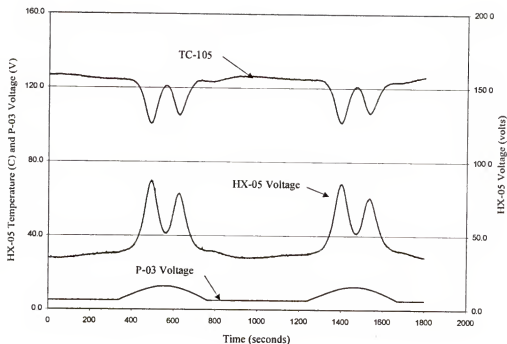


Figure 5-23: Graph of methanol vaporizer HX-05 temperature (TC-105) and voltage along with the pump P-03 voltage as a function of time at 25% power output.

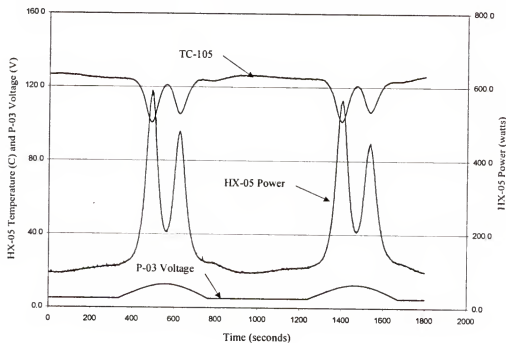


Figure 5-24: Graph of methanol vaporizer HX-05 temperature (TC-105) and power consumed along with the pump P-03 voltage as a function of time at 25% power output.

Fuel Cell Stack Energy Balance

The fuel cell stack is the component that combines the hydrogen and oxygen to form water and electricity. Although the process is efficient (as shown in Figure 5-2), considerable heat is produced during the electrochemical reaction. The efficiency for the brassboard fuel cell stack ranges from 56-47% (based on lower heating value) for 7-21 kW power output, respectively. Thus approximately 6 to 25 kW of waste heat (depending on stack power output) must be removed from the stack.

The operating temperature of the brassboard fuel cell stack varies from 160-190 °C. The higher the operating temperature, the more efficient the electrochemical reaction. The trade-off is that increased stack temperature results in increased rates of catalyst degradation and thus shorter life. Avoiding increased degradation limits the maximum stack temperature to approximately 200-210 °C. In addition, the stack temperature is not uniform, but varies across each cell and from cell-to-cell within the stack. Therefore, the maximum indicated stack temperature must be below the 200-210 °C limit.

At all equilibrium power outputs, the fuel cell stack produces more heat than is required by the stack to maintain its temperature. Thus a coolant (air, liquid, etc.) is used to remove heat from the stack. For liquid-fueled, liquid-cooled systems such as the brassboard engine, the stack waste heat is typically used to vaporize the fuel mixture, therefore reducing the heat input required by the reforming system. Utilizing the stack waste heat has the potential to increase the system efficiency (especially at high power outputs).

During steady-state power output, the fuel cell stack can be modeled using a simplified steady flow process. Fluid velocities are low, and elevation changes are minimal. The resulting first law relation is shown in equation 5-8. The results of the first law analysis are presented in Table 5-5.

$$Q_{\text{LOSS}} + Q_{\text{COOLANT}} + W_{\text{ELEC}} = m \cdot h_e - m \cdot h_i \quad (5-8)$$

where : Q_{LOSS} = heat transfer to the environment

Q_{COOLANT} = heat transfer to the coolant

W_{ELEC} = electrical work

m_e, m_i = mass flow rates of reactants at inlets and outlets of stack

h_i, h_e = enthalpy of reactants entering and leaving the stack

Table 5-5: Results of first law steady flow analysis for the fuel cell stack.

Stack Current (amps)	Stack Power (Watts)	Energy Released $= m \cdot h_e - m \cdot h_i$ (Watts)	Heat Transfer $= Q_{\text{LOSS}} + Q_{\text{COOLANT}}$ (Watts)
112.5	6980	11303	4323
175	10458	17583	7125
240	13794	24114	10320
320	17530	32152	14622
397	20766	39889	19123

The fuel cell stack is well insulated, and heat losses to the environment are difficult to model because of the numerous pipes and cables leaving the stack. Therefore, heat losses and the heat transferred to the cooling loop are grouped together.

Coolant Loop

The brassboard fuel cell engine utilizes a mineral oil coolant to remove heat from the fuel stack (except during startup). The coolant flows through coolant passages placed every five power producing cells within the stack. The stack waste heat removed

by the coolant is utilized to vaporize the methanol-water fuel mixture. The amount of heat required to vaporize the fuel mixture is considerable, greater than the heat input required to superheat and reform the fuel mixture. By utilizing the stack waste heat the system efficiency is improved.

Figure 3-1 is a simple schematic of the brassboard fuel cell engine. Included in the schematic is the coolant loop. The coolant leaves the coolant pump, P-401, and enters the vaporizer plate-type heat exchanger HX-01. Heat is transferred from the coolant to vaporize the fuel mixture. The coolant exits HX-01 and enters resistive heaters H-01:04. These heaters are used when the engine enters the idle mode. During idle, no electrical power leaves the fuel cell engine. The fuel cell stack still produces power, but four resistive heaters dissipate the stack power. Two of the heaters are placed in the coolant loop, and this helps maintain the coolant loop energy balance during idle.

After exiting heaters H-01:04, the coolant enters the startup tube-and-fin heat exchanger HX-03. The term startup heat exchanger is used because during startup, HX-03 is utilized to add heat to the coolant which in turn transfers the heat to the fuel cell stack to raise the its temperature to operating levels (145 °C). During normal operation, heat can be added or removed from the coolant by HX-03. To remove heat, air from fan F-02 is blown across the fins of HX-03. To add heat to the coolant, air and fuel are combusted in burner B-02 and the combustion product is passed across the fins transferring heat to the coolant. In this way, HX-03 is used to control the coolant temperature and thus the stack temperature.

Upon exiting HX-03, the coolant enters the stack and flows through passages placed every five cells. This arrangement is shown in Figure 2-3. The coolant removes the waste heat from the fuel cell stack. After exiting the stack, the coolant enters the coolant pump P-401 to complete the loop.

The coolant maintains the stack temperature. There is no single, easily defined value for the stack temperature. The stack temperature varies across each cell, and also varies from cell to cell. The coolant enters the stack at typically 150 °C for all power output levels. The heat transfer rate from the stack to the coolant increases with power output (see Table 5-5), so the average stack temperature increases with power output. A thermocouple was placed near the middle of the stack and has been defined as the nominal stack temperature. Figure 5-25 shows the nominal stack temperature as a function of the power output.

Coolant Loop Energy Balance

Heat can be added or removed from the coolant in the following locations within the loop (see Figure 3-3):

- heat is removed from the coolant and transferred to the fuel mix (HX-01)
- heat is added to the coolant by H-01:04 (only during idle operation)
- heat is removed from the stack and added to the coolant
- heat is added or removed by HX-03
- heat is lost to the environment (stack heat losses are included in this term)

HX-01 vaporizer heat exchanger

The thermal capacity of the coolant is much greater than the heat required to vaporize the maximum fuel flow. In addition, plate-type heat exchangers are well suited

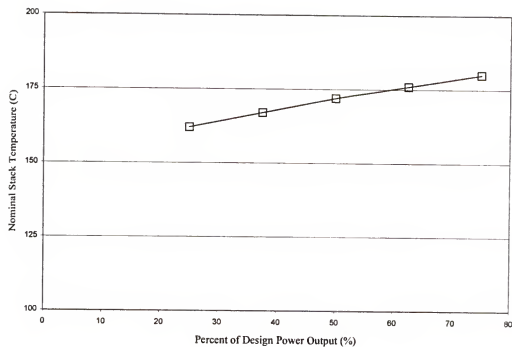


Figure 5-25: Nominal stack temperature as a function of the percent of design power output.

for the vaporizing application due to large surface area and resultant turbulent flow conditions. As a result, vaporization is complete and the superheated fuel mix exit temperature approaches the coolant inlet temperature (counter-flow arrangement). The fuel mix leaves the vaporizer at between 145-160 °C, depending on stack operating conditions. The inlet and outlet temperatures of the fuel mix are approximately constant, so the heat transfer requirements are primarily a function of fuel mixture flow rate.

Figure 5-26 graphs the heat transfer rate and the heat transfer rate normalized as a function of stack current. As expected, the heat transfer rate is essentially a linear function of stack current, primarily because the flow rate of primary methanol is a linear function of stack current. The normalized heat transfer rate represents the required heat transfer rate per unit of stack current. This curve is not constant since the hydrogen utilization by the fuel cell stack is not constant. As shown in Figure 5-14, the stack uses a lower percentage of the available hydrogen at low stack currents which results in a higher relative fuel flow rate at low stack currents, thus requiring higher rates of heat transfer at low current outputs.

Stack Waste Heat

The heat produced by the stack is a product of the stack current and the voltage losses within the stack. As the stack current increases, the consumption of hydrogen increases and so does the heat produced. As the stack current increases, the electrochemical reaction losses also increase, resulting in a lower stack voltage. This means more of the reaction enthalpy is converted to heat rather than electrical power.

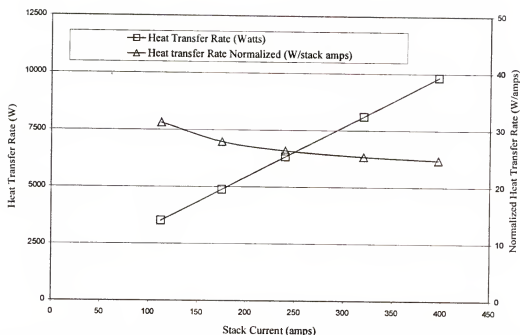


Figure 5-26: Graph of heat transfer requirements of the vaporizer heat exchanger HX-01. HX-01 transfers heat from the coolant to vaporize the fuel mixture.

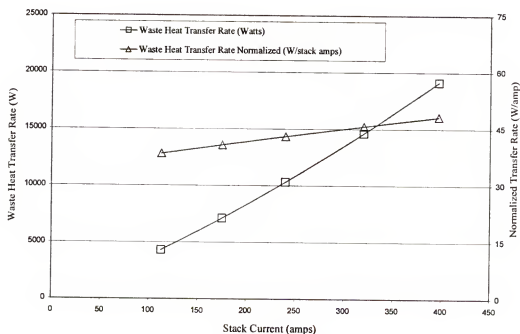


Figure 5-27: Graph of stack waste heat transfer to the coolant as a function of the stack current. The normalized waste heat transfer rate is also included.

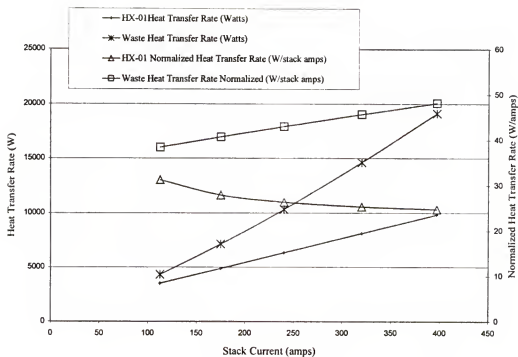


Figure 5-28: Graph of the heat transfer rate and the normalized heat transfer rate for HX-01 and the fuel cell stack.

Table 5-5 lists the stack waste heat ($Q_{\text{LOSS}} + Q_{\text{COOLANT}}$) and Figure 5-27 graphs the waste heat rate and the normalized waste heat rate. The cell losses are also a function of the stack current, thus the waste heat produced is a second order function of the stack current. The normalized stack waste heat transfer rate is a linear function of stack current because it is purely a function of the cell losses. As shown in Figure 5-1, the engine operates in the linear portion of the polarization curve, meaning the cell losses are linear with stack current.

The importance of the two normalized curves is shown in Figure 5-28 which combines Figures 5-26 and 5-27. At low stack current, the waste heat available is approximately the heat required for vaporization. Full vaporization of the fuel mixture is essential for proper reformer operation (including no permanent catalyst degradation). Once losses to the environment are factored in (which can be very large from HX-03), the net result is at low stack current the startup burner B-01 is utilized to maintain the coolant temperature. The methanol used in the burner directly lowers the system efficiency.

Startup burner/HX-03 operation

The tube-and-fin heat exchanger, HX-03, and associated components (burner, fuel pump P-04, fan F-02, etc.) are used to control the temperature of the coolant entering the stack. In doing so, HX-03 controls the stack temperature. The nominal stack temperature is shown in Figure 5-25.

Table 5-6 shows the results of the energy balance for the coolant loop. The additional heat transfer represents the heat available to offset losses to the environment. Testing has shown that the coolant loop is in thermal balance at approximately 50% of

design power output. This indicates losses to the environment at approximately 4000 watts. For lower power outputs, energy must be added to the coolant to maintain engine temperatures.

Table 5-6: Results of energy balance for the coolant loop.

Stack Current (amps)	Stack Heat Transfer $= Q_{\text{LOSS}} + Q_{\text{COOLANT}}$ (Watts)	HX-01 Heat Transfer (Watts)	Additional heat transfer (Watts)
112.5	4323	3516	807
175	7125	4885	2240
240	10320	6329	3991
320	14622	8109	6513
397	19123	9826	9297

When adding heat to the coolant, the burner is operated in an on/off arrangement. As the temperature of the coolant entering the stack drops below 145.0°C, fan F-02 blows air through B-02 to clear any residual methanol from the chamber. Ignitor I-02 (see Figure 3-3) is lit and methanol pump P-04 delivers methanol to the burner chamber. The combustion product flows across the fins of HX-03 and heat is transferred to the coolant. The stack coolant inlet temperature increases, and the flow of methanol is stopped when the temperature reaches 155 °C. At this point the air flow is continued for 60 seconds to clear the combustion chamber. After 60 seconds, the air flow rate is substantially reduced (<10 scfm) to provide a small purge flow.

Figure 5-29 graphs the stack coolant inlet temperature, fan F-02 voltage, and pump P-04 voltage as a function of time for 25% steady-state power output. When the F-02 voltage is first increased to approximately 50 volts to clear the combustion chamber, the stack coolant inlet temperature drops quickly because significant heat is removed from the coolant as the air flows across fins of HX-03. The air flow precedes

the fuel flow by 30 seconds. The fuel flow begins and combustion is achieved. At this point, the ignitor is turned off and the fan voltage is increased to 66 volts (174 ft³/min). The fuel flow continues for 4-5 minutes, raising the stack coolant inlet temperature. Once the stack coolant inlet temperature reaches 155 °C, the fuel flow is stopped but the air flow continues for 60 seconds. During this 60 second period, the stack inlet temperature drops sharply because of the high volume of low-temperature air passing across the fins of HX-03. After 5-10 minutes the process begins again.

Pump P-04 fuel flow rate is 89.5 g/min. Testing has shown that pump P-04 is operated approximately 38% of the time at 25% stack power output, resulting in an average of 34.0 g/min methanol flow rate. This is a considerable quantity of methanol since at 25% power output the primary methanol flow rate is only 55.3 g/min.

Figure 5-30 shows the same graph as Figure 5-29 but for a stack power of 37.5% of design power output. The graph shows that the burner is used less frequently than for the 25% case. The production of stack waste heat rises faster with increased power output than does the requirement for increased heat transfer in the vaporizer HX-01. This results in less heat input in HX-03, and testing indicates that the burner is used 17.5% of the time resulting in an average flow of 15.7 g/min.

At approximately 50% of design power output, the coolant loop is in balance. The stack waste heat produced nearly matches the heat input requirements of HX-01 and the heat losses to the environment. Figure 5-31 graphs the stack coolant inlet temperature, fan F-02 voltage, and pump P-04 for 50% of design power output. The curves are flat, indicating that the parameters are constant and the coolant loop is in balance. Pump P-04 is not turned on, so there is no methanol flow.

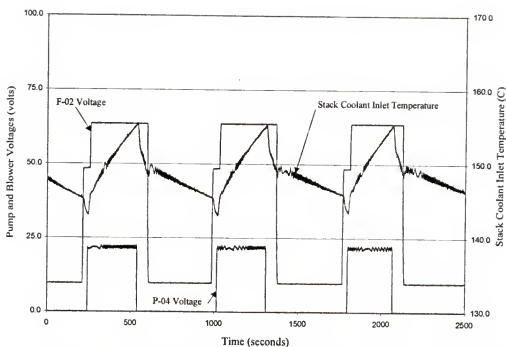


Figure 5-29: Stack coolant inlet temperature and F-02 and P-02 operation for 25% of design power output.

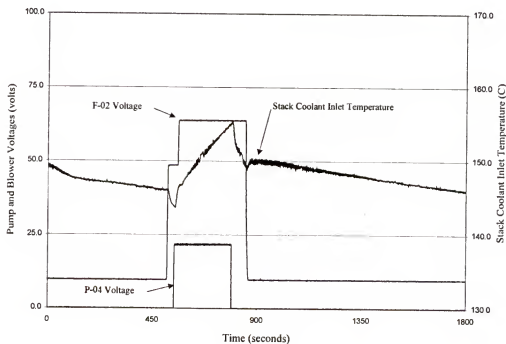


Figure 5-30: Stack coolant inlet temperature and F-02 and P-02 operation for 37.5% of design power output.

For stack power output levels above 50% of design power output, the voltage delivered to fan F-02 is increased to remove heat from the coolant loop. The relationship between F-02 voltage and the stack coolant inlet temperature (TCA-401) is depicted in algorithm 5-9.

$$\text{F-02 Voltage} = 10 + 5 \times [\text{TCA-401}(\text{°C}) - 150] \quad (5-9)$$

Operation using this simple control algorithm attempts to maintain the stack coolant inlet temperature at 150 °C by increasing the fan voltage to increase air flow across the fins of HX-03 to remove additional heat from the coolant. Figure 5-32 graphs the stack coolant inlet temperature, fan F-02 voltage, and P-04 voltage for 62.5% of design stack power output. The stack coolant inlet temperature is rising, indicating that the stack waste heat is greater than the heat transferred in HX-01 and losses to the environment. Towards the end of the graph the stack coolant inlet temperature is beginning to flatten out as the coolant loop is beginning to balance.

Startup burner methanol flow rate

Comparison of the Figures 5-26 through 5-32 indicate some interesting points directly related to efficiency. Figures 5-26 through 5-28 show that more heat is produced in the stack than is required to vaporize the fuel mix. However, Figure 5-29 shows that considerable methanol flow rate is required to maintain the energy balance within the coolant loop. There are many reasons for the extensive use of methanol at the low power outputs. One reason for the high methanol flow rate into burner B-02 at low power is that the low fuel utilization (as little as 60% of hydrogen is consumed by the stack) results in increased heat transfer from the coolant in the vaporizer HX-01. The

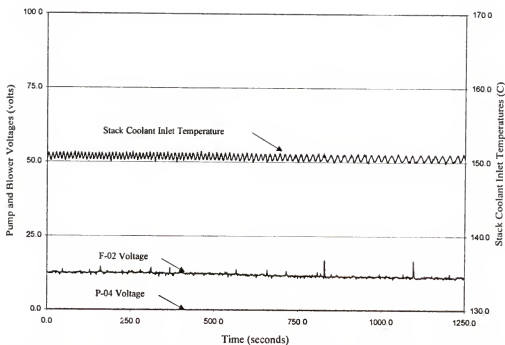


Figure 5-31: Stack coolant inlet temperature and F-02 and P-04 operation for 50% of stack design power output.

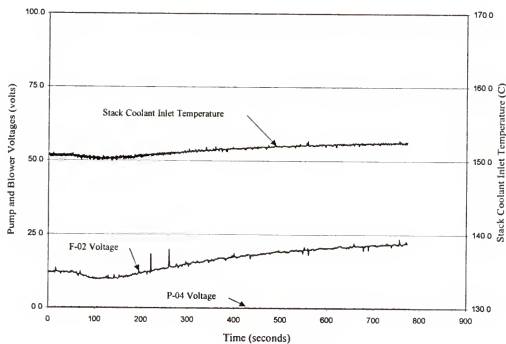


Figure 5-32: Stack coolant inlet temperature and F-02 and P-04 operation for 62.5% of stack design power output.

startup heat exchanger (HX-03) is a relatively large (510 mm x 330 mm x 350 mm) heat exchanger that is not insulated. Because it is a tube and fin arrangement, the heat transfer area is enormous (19.3 m^2). The outside shell is not insulated so as to allow easier heat removal from the coolant at high power outputs, but results in a significant detriment at low power outputs. The on/off operation combined with the control strategy for fan F-02 results in a high volume of air being blown across the fins of the exchanger before and after heating has occurred. The result is much of the heat transferred into the coolant is subsequently removed by this air flow. And finally, the overall air-fuel mixture is very lean, resulting in an adiabatic combustion temperature of only $\approx 275^\circ\text{C}$. The coolant operating temperature is between 145 and 160°C , and thus much of the energy associated with the combusting the methanol is lost in the exhaust stream. This inefficient use of the P-04 methanol flow rate results in a significant overall efficiency penalty at low power outputs.

Total Methanol Flow Rate

There are three pumps that deliver methanol to the brassboard engine during steady-state operation. P-01 is the primary fuel pump that delivers the methanol for the fuel mixture that enters the steam reformer. P-03 is the methanol trim pump that is used to maintain the steam reformer catalyst bed temperatures. P-04 is the startup burner pump that is used to maintain the temperature of the fuel cell stack.

Figure 5-33 shows the instantaneous methanol flow rate for 25%, 37.5%, 50%, and 62.5% of design power output. For the 50% and 62.5% cases, the total methanol flow rate is constant. The majority of the methanol is from the primary methanol pump P-01 whose flow rate is dependent on the stack current, and therefore approximately

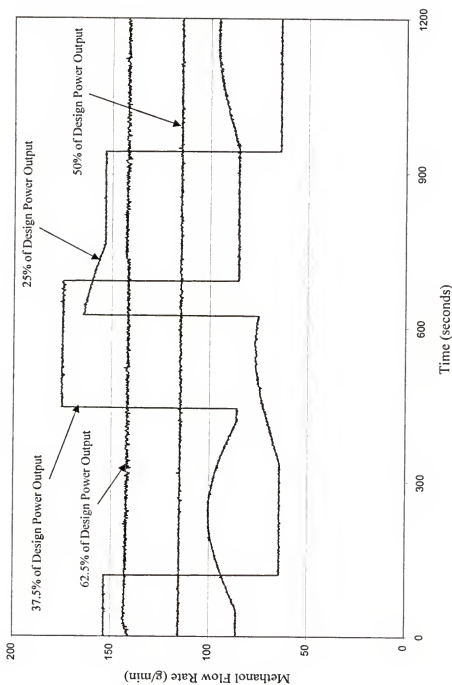


Figure 5-33: Graph of the total methanol flow rate as a function of time for 25%, 37.5%, 50%, and 62.5% of the design power output.

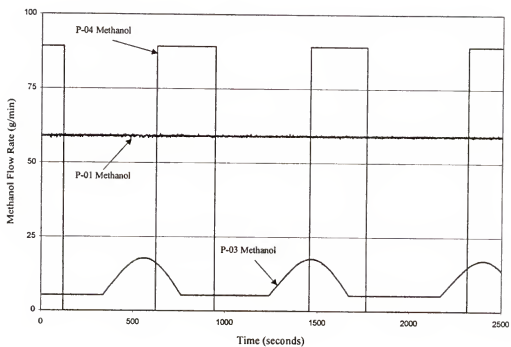


Figure 5-34: Instantaneous methanol flow rate for the three fuel pumps during steady state operation at 25% of design power output.

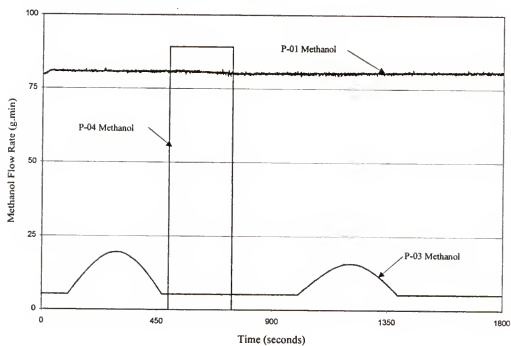


Figure 5-35: Instantaneous methanol flow rate for the three fuel pumps during steady state operation at 37.5% of design power output.

constant for the steady-state case. The methanol flow rate of pump P-03 remains constant at its lowest flow rate of 5-6 g/min. Methanol pump P-04 does not typically operate at or above 50% of design power output.

The 25% and 37.5% cases are quite different. The total methanol flow rate changes dramatically, principally due to the operation of the startup burner pump P-04. Figures 5-34 and 5-35 show the instantaneous methanol flow rates for each pump for the 25% and 37.5% cases, respectively. Figure 5-34 clearly indicates the quantity of methanol (pumps P-03 and P-04) used to maintain the engine temperatures. Even pump P-03 low flow rate of 5-6 g/min is approximately 10% of the primary methanol flow rate. The obvious result of the additional methanol is a significant drop in overall efficiency. Figure 5-35 shows that pump P-04 is used less for the 37.5% case than the 25% case, but still adds a significant amount of methanol to the total flow rate. The effect of pump P-03 is still substantial but relatively less than the 25% case because the primary flow of methanol is increased (80 g/min versus 59 g/min).

Table 5-7 lists the average methanol flow rates for the different pumps at the various power outputs. The average total flow rate of methanol and the percent contribution of each pump are also included in the table.

Table 5-7: Methanol flow rates for each pump during steady-state operation.

Power	P-01 (g/min)	% of Total	P-03 (g/min)	% of Total	P-04 (g/min)	% of Total	Total (g/min)
25%	59.0	57.8	9.1	8.9	34.0	33.3	102.1
37.5%	80.2	76.9	8.4	8.1	15.7	15.0	104.3
50%	109.5	95.4	5.25	4.6	0.0	0.0	114.75
62.5%	136.8	96.3	5.25	3.7	0.0	0.0	142.05
75%	164.4	96.9	5.25	3.1	0.0	0.0	169.65

It is difficult to develop an average for pump P-04 because it is operated in an on/off fashion. The engine was allowed to reach steady-state and then operated for 1-2 hours to allow the pump to cycle multiple times. The average flow rate was determined by averaging numerous engine tests.

The most striking values in Table 5-7 are the total flow rate for the 25%, 37.5%, and the 50% of the design power output. The total flow rates for 25% and 37.5% cases are nearly identical. This highlights the significance of the methanol flow rate associated with P-04. The power output is nearly doubled for the 50% case as compared to the 25% case, but the 50% case only requires 10% higher methanol flow rate. The data clearly shows that the brassboard engine should be operated above 50% of design power output or a significant efficiency penalty occurs.

Average System Efficiency

The average system efficiency is defined as the stack power output divided by the lower heating value of the total methanol flow rate. The system efficiency shows clearly the effects of the auxiliary flows of methanol. Figure 5-36 graphs the system efficiency as a function of percent of design power output. Also included are the cell efficiency and the stack efficiency for comparison.

The small difference in system efficiency and stack efficiency at power outputs greater than 50% of design is due to the methanol flow rate from P-03 (5.25 g/min). At low power outputs, the efficiency drops dramatically due to the additional flows of methanol. The shape of the three efficiency curves is different: the system efficiency is much lower at low power outputs, the stack efficiency is almost constant, while the cell

efficiency is higher at low power outputs. This highlights the need to define and use the appropriate efficiency definition.

Power Conditioning

Fuel cell stacks deliver direct current electrical energy. As earlier discussed, the nominal cell voltage is determined by the number of cells and the stack current is determined by the cell area. The electrical power often requires conditioning such as DC-DC chopping, DC-AC inverting, etc. The brassboard fuel cell engine was designed to be integrated into a fuel cell/battery parallel hybrid arrangement. The interface between the fuel cell stack and the battery pack is a DC-DC converter.

The voltage output from the fuel cell stack is approximately 50-65 volts. The goal of the hybrid arrangement is to allow the batteries to discharge thus providing additional current during periods of high vehicle power demand, and to charge and store energy during periods of low vehicle power demand. As such, the battery voltage can swing substantially, up to 80 volts on the fuel cell transit bus. For the brassboard engine, the step-up chopper converts the fuel cell stack electrical power to a voltage between 140 and 250 volts. Currently, the chopper interfaces with fifteen 12 volt lead acid batteries giving a nominal battery voltage of 180 volts.

Tests were run to determine the efficiency of the step-up chopper for different power inputs (stack power outputs) and for output voltages between 180-200 volts. Figure 5-37 shows the results of the testing. The efficiency is good, ranging from 94.5% to 96.5%. The slightly lower efficiency at high power could be related to the higher current in and out of the chopper. This is not a true efficiency, however, since there are fans and a few small power supplies within the step-up chopper that are operated off

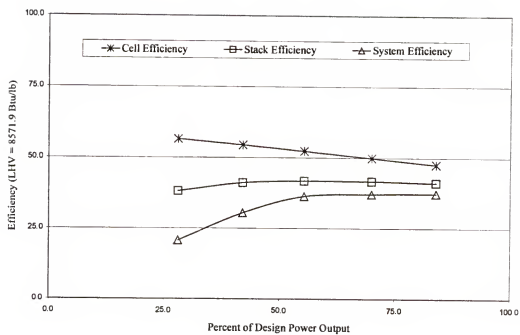


Figure 5-36: Brassboard fuel cell engine system efficiency as a function of power output. The cell efficiency and stack efficiency are also included.

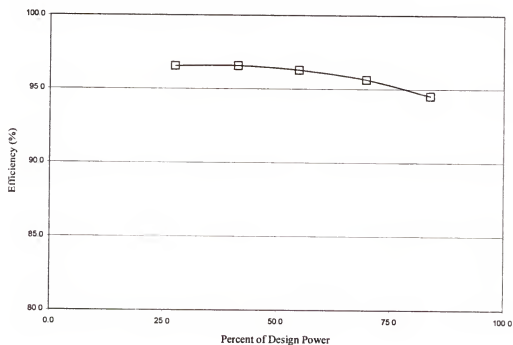


Figure 5-37: DC-DC converter efficiency (power output/power input) as a function of the percent of design power output.

wall power. It was not practical to measure these currents individually and the electrical power used is accounted for in the overall parasitic power measurements.

Figure 5-38 shows the overall engine efficiency, defined as usable power output divided by the lower heating value of the total methanol flow rate. Also included are the cell, stack, and system efficiency curves. The overall engine efficiency has a similar shape to the system efficiency as the step-up chopper efficiency is fairly constant.

Parasitic Power Consumption

The term parasitic power is used to define the electrical power used to operate ancillary various components to operate. These components include fans, blowers, pumps, power supplies, solenoid valves, etc. The quantity of electrical power typically is substantial and has a strong effect on the net efficiency of the system.

The parasitic power for the brassboard engine is delivered from wall power. Two 208V, three phase circuits deliver electrical power to the switchboard where it is distributed to the appropriate component or power supplies. The various power supplies deliver DC power to the engine components and are controlled remotely through a 0-10 volt signal from the control computer. Some components, such as the step-up chopper cooling fans, receive switched power directly from the wall. The control computer also plugs directly into 110 AC wall power.

One of the two 208, three phase wall circuits delivers power primarily for the coolant pump P-401. The coolant pump operates from a variable voltage, variable frequency controller, but operates at one speed during normal operation. As such, the power consumption is approximately constant once the coolant reaches operating

temperature. The average power consumption during normal operation is approximately 760 watts.

The other 208V, three phase line is distributed to provide 110V AC, single phase power to the various power supplies. The parasitic power consumption of this circuit is dependent upon the state of the system. The states of the various blowers, pumps, heaters, etc. directly determine the parasitic power consumed. Approximately 300 watts of electrical power is used to energize all the electrical switchgear, power supplies, etc.

Figures 5-39 through 5-42 show parasitic power curves for 25%, 37.5%, 50%, and 62.5% percent of design power outputs. Figures 5-39 and 5-40 show a varying parasitic power consumption because of the various pumps, blowers, and heaters that are turning on/off or higher/lower based on changing methanol flow rates within the engine. For the 50% and 62.5% case, the parasitic power curves are flat indicating the engine is in balance. The parasitic power for the 62.5% case is slightly higher than the 50% because of the higher power consumed by fan F-02 to move more air across HX-03 to remove heat from the coolant loop.

Figure 5-43 shows the important parameters that produce the shape of the parasitic power curve for 25% of design power output. When the coolant temperature drops, the blower F-02 turns on to provide air for burner B-01. The fan voltage is graphed on Figure 5-43 and this component turning on causes the square wave shape of the parasitic power curve. When the reformer catalyst bed temperature drops, the P-03 methanol flow rate increases. The power consumed by the pump is minimal (below 20 watts), but the electrical power input to the vaporizer HX-05 is substantial. As the

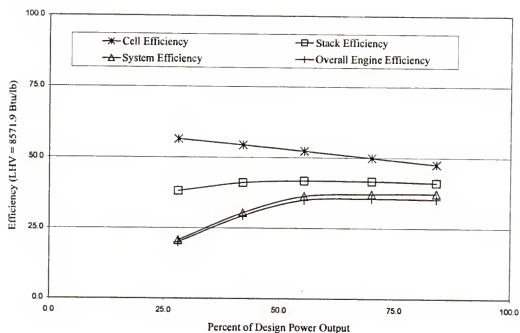


Figure 5-38: Overall engine efficiency as a function of design power output. The cell, stack, and system efficiency curves are presented for comparison.

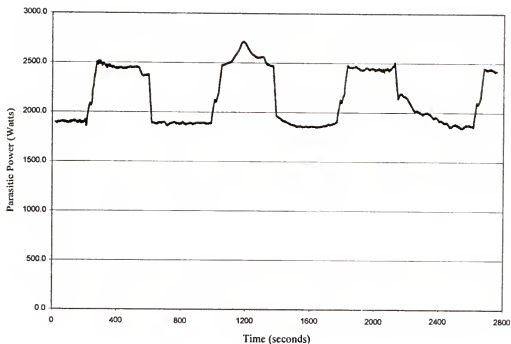


Figure 5-39: Typical total parasitic power consumption curve for 25% of design power output.

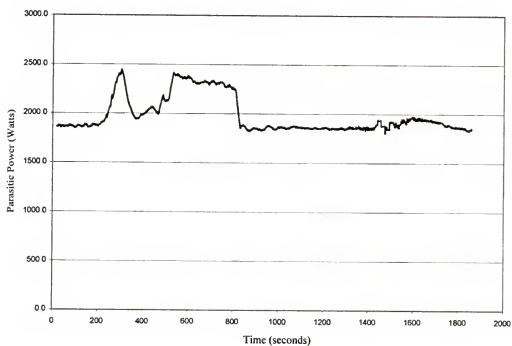


Figure 5-40: Typical total parasitic power consumption curve for 37.5% of design power output.

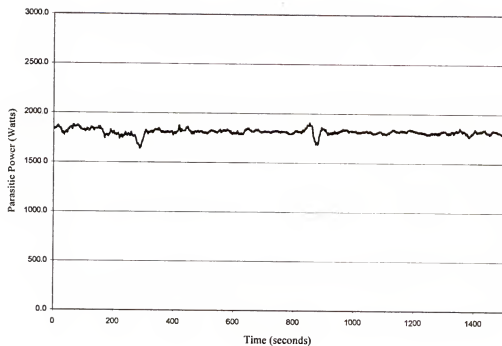


Figure 5-41: Typical total parasitic power consumption curve for 50% of design power output.

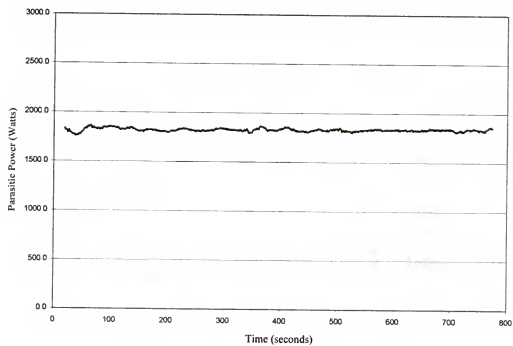


Figure 5-42: Typical total parasitic power consumption curve for 62.5% of design power output.

voltage of HX-05 increases, the power consumed also increases. The peak power use of HX-05 in this graph is approximately 450 watts. Thus, the shape of the parasitic power curves for 25% and 37.5% of design power output are caused by the need to add heat to the engine to maintain its temperatures. At 50% of the design power output and above, heat must be removed from the system to maintain temperatures.

Net Overall Engine Efficiency

The net overall engine efficiency is defined as the net power output (usable power minus parasitic power) divided by the heating value of the total average methanol flow rate. This efficiency gives the truest indication of the performance of the brassboard fuel cell engine. Figure 5-44 graphs the net overall efficiency as a function of design power output. The efficiency is only 13.6% at 25% of the design power output, and increases to 32% at 75% of the design power output. Other efficiency curves are also presented for comparison. It is clear that using the cell or stack efficiency as a performance indicator is very misleading for a liquid-fueled fuel cell system.

The curve for the instantaneous net overall engine efficiency at 25% of design power is shown in Figure 5-45. The curve has a square wave shape similar to the total methanol flow rate. The efficiency varies from 8.0% to 22.5%. The instantaneous efficiency falls to only 8.0% because when the fuel flow rate increases (P-03 and P-04) the parasitic power losses also increase (F-02 and H-05). The result is that the engine, at times, operates very inefficiently. It should also be noted that the efficiencies shown do not reflect energy usage during startup shutdown, both of which will lower the daily efficiency.

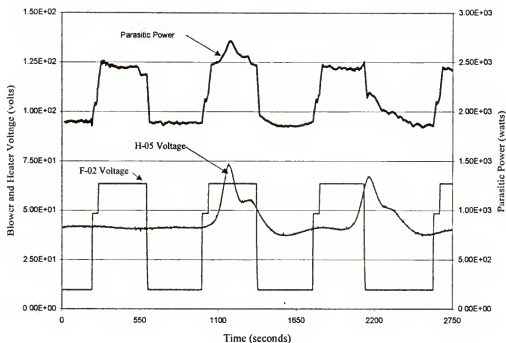


Figure 5-43: Important parameters that determine the shape of the parasitic power curve as a function of time for the 25% power output case.

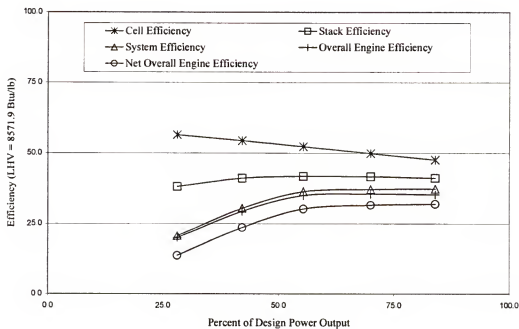


Figure 5-44: Net overall engine efficiency curve for the brassboard engine. Also included are the cell, stack system, overall efficiencies.

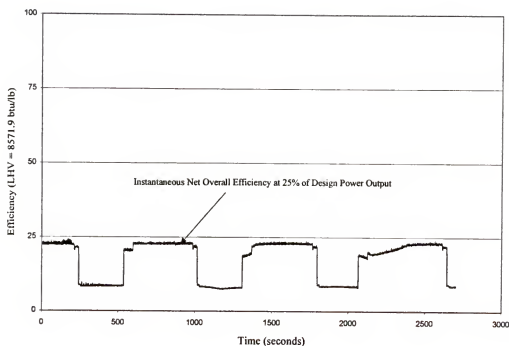


Figure 5-45: Instantaneous net overall efficiency for 25% of design power output.

Conclusions

The tested brassboard fuel cell engine efficiency is well below most of the published values for fuel cell efficiencies. There are many reasons for this, including that the brassboard engine performance has degraded. But the primary reason is that current practice typically overestimates the performance of fuel cell systems and engines, especially in the off-design condition. Another important reason is that the brassboard engine was designed to maximize the design point efficiency and not enough effort was put forth into optimizing the off-design condition.

Part of the reason for off-design low efficiency is a lack of fundamental understanding of fuel cell engine performance. The causes of this low efficiency are not fuel cell stack or reformer performance, but rather the inefficient use of waste heat and burner fuel throughout the engine. This results, especially at low power outputs, in considerable auxiliary flow rates of methanol and increased parasitic power consumption.

Transient Operation

Introduction

The brassboard fuel cell engine was designed to operate with batteries in a hybrid arrangement. The hybrid architecture is referred to as battery leading, which means that the output of the fuel cell engine is dependent upon the state of the batteries and in addition to vehicle power requirements. The goal of this architecture is to maintain the battery state-of-charge within a small range, such as 70-75%. When the battery state-of-charge drops to the low end of the range, the fuel cell ramps up power

output. When the battery state-of-charge reaches the upper limit, the fuel cell engine ramps down.

This architecture allows the fuel cell engine power output to remain constant for relatively long periods of time, thus minimizing power transients and allows the fuel cell engine to change power outputs very slowly. The brassboard fuel cell engine requires approximately 7 minutes to increase from 25% to 100% of design power output (≈ 2.5 kW/min). The 50 kW transit bus fuel engine (same manufacturer, similar design) requires 3 minutes to increase from 25% to 100% of design power output (≈ 12.0 kW/min). The brassboard fuel cell engine decreases power output essentially instantaneously according to control input.

One problem with this architecture is that a large portion of the fuel cell power output charges batteries with the stored energy subsequently released through the battery discharge, thus incurring an additional charge-discharge efficiency penalty. For the next generation of fuel cell/battery hybrid buses, fuel cell leading architecture is employed. Under this architecture, the fuel cell engine attempts to follow the vehicle power requirements, therefore minimizing the current in and out of the batteries. To accomplish this task, the fuel engine transient response is approximately 20 kW/second, a considerable improvement over the brassboard response.

Transient Performance

Because of the slow transient response, the brassboard engine operates in a quasi-steady-state as it alters the power output. The control strategy remains primarily the same as the steady state case, with one exception. The flow rate of primary methanol and de-ionized water is increased above normal levels during increases in

power output. Equation 5-2 and 5-3 show the relationship between stack current and P-01 and P-02 voltage for steady-state operation. Figure 5-6 graphs the calculated pump voltages versus the actual voltages, and shows that the voltage (thus the flow rate) increases faster during transients.

Figure 5-46 clearly shows the increased methanol flow rate during an increase in power output from 25 to 50% of design power output. The extra flow rate of methanol and de-ionized water is used primarily for two reasons. The first is to insure that there is sufficient hydrogen available at the fuel cell stack anode electrode. Starving the stack of hydrogen results in very low partial pressure of the hydrogen which causes the cell voltage to collapse. As the cell voltage collapses, most of the chemical energy is converted to heat and severe degradation of the platinum catalyst can occur.

The other reason is that modeling has shown that the transient response of the fuel cell engine is limited by the rate of heat transfer into the reformer catalyst bed. As the flow rates of methanol and water increase, more heat is removed internally from the bed. During transients, the additional flow of methanol results in extra hydrogen available for use as reformer burner fuel. This extra fuel raises the burner temperature which helps transfer additional heat into the bed as is shown in Figure 5-47. As the flow rate of P-01 methanol increases, the middle and upper bed temperatures decrease. With the additional flow rate of methanol (over steady-state), the heat transfer into the bed increases and the temperatures recover. The increased methanol flow occurs only when power is increasing, and the additional methanol flow rate averages ≈ 10 g/min.

The difficulty with this scheme is that control of the bed temperatures is very difficult. If transient operation continues, the catalyst bed temperatures continue rise

and continued operation above 300-310°C will result in degradation of the reformer catalyst bed. Figure 5-48 shows the catalyst bed temperatures as a function of time for repeated transients between 25% and 50% of the design power output. These curves are quite different from the steady-state bed temperature curves (Figures 5-9 through 5-12). The middle bed temperature reaches 340°C, well above the maximum desired bed temperatures.

Figure 5-49 also shows the effect of transients on reformer bed temperatures. The engine was operated at 50% of design power output. The power output was then changed between 37.5% and 62.5% of design power. The bed temperatures increase and begin to oscillate, showing the effects of the additional primary methanol flow rate of ≈ 10 g/min.

A secondary effect on efficiency during transients is that the cell voltage deviates from steady-state polarization. This occurs because of the difference between stack temperature during transients versus steady-state. At 50% steady-state power, the recorded stack temperature is approximately 171°C. During an up-transient from low power, when the power output equals 50% of the design power, the stack temperature is only 164-165°C. This results in lower stack voltage and therefore higher stack current to achieve the desired power output. Increased stack current increases P-01 methanol flow and therefore lowers efficiency. This loss in efficiency is partially offset during down transients when the stack temperature is higher than the steady-state case, resulting in increased stack voltage.

It is difficult to determine the entire nature of the effect of transients on engine efficiency due to the off-on nature of component operation which makes it difficult

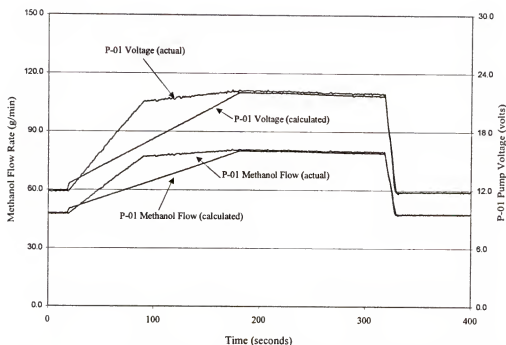


Figure 5-46: P-01 voltage and P-01 methanol flow rate for an up-transient from 25% to 50% of design power output.

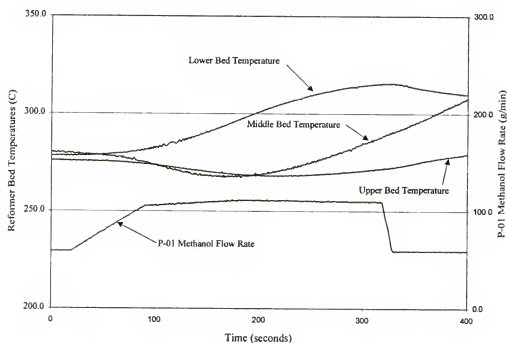


Figure 5-47: Reformer bed temperatures and P-01 methanol flow rate as a function of time during an up-transient from 25% to 50% of design power output.

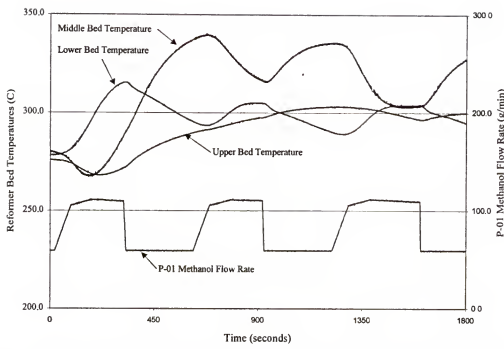


Figure 5-48: Reformer bed temperatures as a function of time for repeated transients between 25% and 50% of design power output.

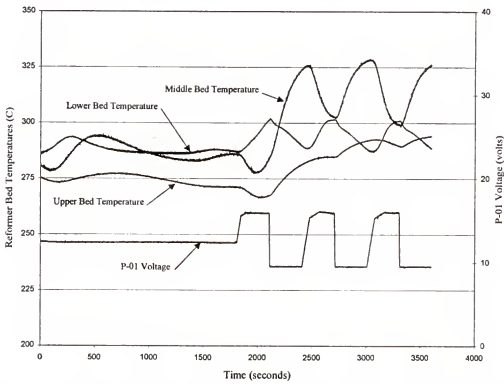


Figure 5-49: Comparison of reformer bed temperatures for steady-state 50% of design power and transient operation between 37.5% and 62.5% of design power output.

to achieve repeatable tests. If the power output increases occur above 50% power, the engine loses efficiency because of the 10 g/min increase in P-01 methanol flow. If the transients occur below 50% power output, the 10 g/min increase in P-01 flow is offset by reduction in P-03 reformer trim pump flow methanol flow. The effect of transient operation is dependent on the state of the system, the power levels at the beginning of the transients, and the frequency of the transients. However, if the system is operated within a battery leading hybrid arrangement, the effect of transients on efficiency is minimal primarily because of the slow transient response of the engine.

Startup and Shutdown

Introduction

The energy associated with starting and shutting down the brassboard fuel cell engine is significant. The effect of this energy consumption on efficiency is especially significant for transportation applications where engines may be started and shutdown daily, or even more often. The stack operates at 160 to 190 °C and the catalyst bed operates at 280 to 300 °C. The goal of the start-up is to increase the temperature of the various components close to the operating temperature within a short period of time. Currently, the brassboard requires 35-45 minutes to start. The goal of shutting down the system is to lower the engine temperature in a manner that minimizes thermal stresses on the various catalysts within the engine. The brassboard requires approximately 30 minutes to shutdown.

Engine Startup

The temperature of the fuel cell stack is raised by combusting methanol from P-04 in burner B-01. The combustion product is passed across the fins of HX-03 where

heat is transferred to the coolant. The coolant exits HX-03 and enters the fuel cell stack, where heat is transferred to the cells. Pump P-04 operates almost continuously during startup.

The temperature of the reformer catalyst bed is raised by adding liquid methanol (P-05) and vaporized methanol (P-03) to the reformer burner. The combustion product flows across the walls of the catalyst bed, transferring heat into the bed. The heat is not transferred uniformly, so the burner is turned off periodically to allow hotter parts of the bed to transfer heat to cooler parts, e.g. to “equalize” the temperature.

Once the catalyst bed has reached operating temperatures, the primary fuel mix (methanol and de-ionized water) is started. The reforming product (reformate or hydrogen rich gas) is not passed to the stack, but instead is bypassed back to the reformer burner. This is done to insure the engine has time to stabilize and to insure that only high quality (high methanol conversion) reformate enters the stack. After a short period of time (2-7 minutes typically), the reformate is flows through the stack and an open-circuit test is performed. If the system passes the open circuit test (>0.8 volts/cell), the engine startup has completed.

Startup methanol consumption

The methanol consumption during startup is substantial. Pump P-04 methanol flow rate is 89.2 g/min and the pump operates nearly continuously during startup. The average methanol consumption for startup is 135-145 g/min or a total of 5.0-5.5 kg of methanol (≈ 1.5 gallons). This methanol consumption is equivalent to operating the brassboard at 50% of design power output for approximately 45 minutes, so it can have

a drastic effect on daily average engine efficiency for the transportation application, depending on start frequency and duty cycle.

Figure 5-50 graphs the methanol flow rate of the different pumps. Pump P-04 provides the energy to reach start temperatures for the fuel cell stack section of the engine. Pumps P-01, P-03, and P-05 provide the energy to reach start temperatures for the reformer section of the engine. The methanol input for the fuel cell stack section is approximately 2/3 of the total methanol input. One reason is that the startup burner/HX-03 arrangement is not an efficient setup (as explained during steady-state discussion). The combustion temperature is low due to excessive air flow so approximately half the lower heating value of the methanol is lost to the exhaust stream. HX-03 is not insulated so heat losses to the environment are large. For these reasons, the methanol consumption is substantial. Figure 5-51 graphs the total methanol flow rate versus time for startup. This curve indicates the extent of methanol use when compared with the methanol consumption at a steady 62.5% power output of 142 g/min, approximately the average methanol consumption during startup.

Startup parasitic power consumption

The parasitic power consumption during startup is also substantial. Many of the pumps, blowers, electric heaters, etc. are operating near maximum levels. The average parasitic power draw during startup is 2870 watts, higher than any other operation point.

Figure 5-52 graphs the parasitic power draw versus time for startup. Figure 5-53 provides the important components that determine the shape of the parasitic power curve. The dominant factor is the voltage of the vaporizer H-05. This electric heater is used to vaporize the P-03 methanol flow rate into the reformer burner. During startup,

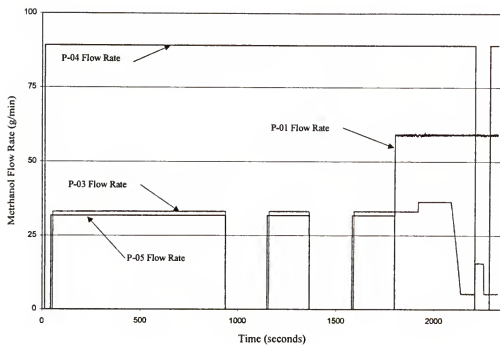


Figure 5-50: Various methanol flow rates as a function of time

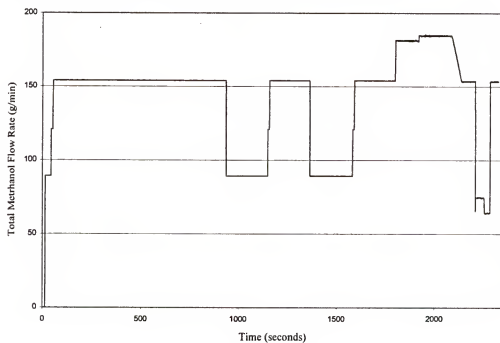


Figure 5-51: Total methanol flow rate during startup as a function of time. Start begins at time equal zero.

this pump is operating at close to maximum output, and the electric power draw of the heater is up to 775 watts. In addition, the reformer burner blower (fan F-01) and the startup blower (fan F-02) are operating at close to maximum capacity during the entire startup. The result is a high parasitic power penalty is associated with startup.

Reformer catalyst bed temperatures

One of the main difficulties in starting the brassboard engine is heating the reformer catalyst bed in a quick and uniform method. The rate of temperature increase of the catalyst must be limited to minimize thermal stresses and therefore catalyst degradation. The conduction time lag associated with transferring heat into a packed bed of catalyst also makes it difficult to control temperatures due to poor. In addition, heat is not added in a uniform manner. Under normal operation, the majority of the reforming process is occurring in the first 50% of the bed length. This means most of the heat removed is in this part of the bed. The combustion gas flows in a co-flow arrangement with the fuel mixture, and thus most of the heat is transferred into the first part of the bed (highest temperature difference).

A problem occurs during startup when heat is added to the bed, but no reforming (heat removal) is occurring. The first third of the catalyst bed heats up quite quickly while other parts lag behind. To offset this, the burner is turned on and off periodically to allow the bed temperatures to begin to equalize. The time requirement for startup does not allow the bed to properly equalize and results in large temperature variations throughout the bed.

For the catalyst bed to operate properly, all parts of the bed need to be above 220°C. It is difficult during startup to achieve this temperature without much higher

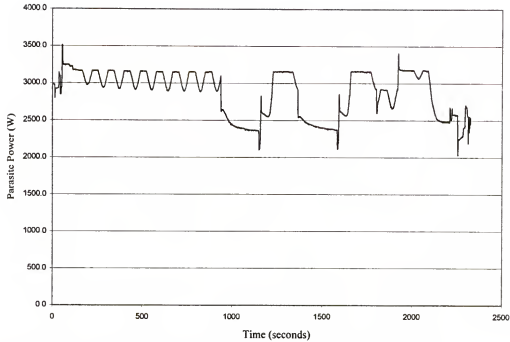


Figure 5-52: Instantaneous parasitic power consumption during startup.

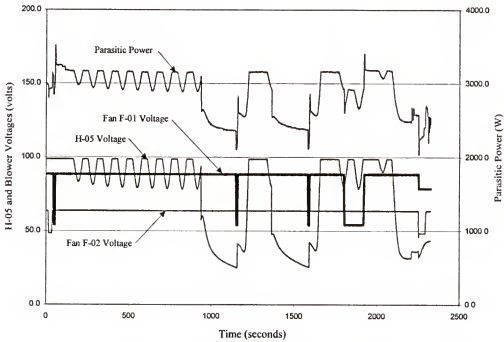


Figure 5-53: Instantaneous parasitic power and important component voltages for startup.

temperatures occurring in some parts of the bed. Thus the fuel mixture flows through the catalyst bed when the upper part of the bed is only $\approx 190^{\circ}\text{C}$. This limits the conversion of methanol, and causes problems with the reformer burner losing its flame due to poor fuel composition (low hydrogen and high methanol and water content).

Figure 5-54 shows the catalyst bed temperatures during a typical brassboard startup. P-01 is the primary methanol fuel pump, and its voltage curve is added to indicated when the methanol and de-ionized water fuel mixture passes over the catalyst bed.

Figure 5-55 shows the same curves when the reformer catalyst bed is overheated during startup. The fuel mixture is flowing through the catalyst bed and the reformat is bypassed directly to the reformer burner for too long. This results in dramatic increases in bed temperatures because of the high combustion temperatures. Temperature excursions above 400°C can occur which result in degradation of the reformer catalyst.

Engine Shutdown

Shutdown of the brassboard engine takes approximately 30 minutes. During this time, the engine operates in idle mode as the temperature of the stack is lowered to 130°C . At this point, blowers F-01 and F-02 operate to blow air through the reformer and HX-03, respectively for 5 minutes to further lower the engine temperatures. The goal of shutting the system down is to minimize thermal stresses and degradation of the stack performance.

Shutdown methanol consumption

The methanol consumption is minimized during shutdown. Because the engine is in idle mode, pumps P-01 and P-03 deliver the minimum methanol flow rate. Pump

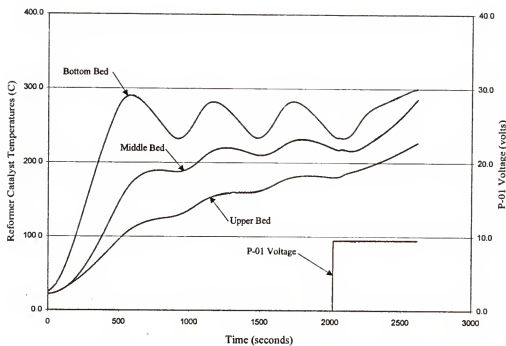


Figure 5-54: Reformer bed temperature profiles during normal startup.

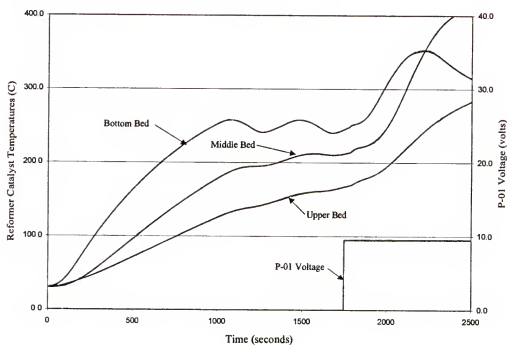


Figure 5-55: Reformer bed temperature profiles during startup where the catalyst bed is overheated.

P-04 is turned off. The result is that 63-64 g/min of methanol are consumed. The length of time for shutdown varies slightly with the engine temperature, but it typically takes 25 minutes. The methanol consumption is 1.75-1.85 kg of methanol. This is approximately 1/3 the methanol consumed for startup.

Shutdown parasitic power consumption

The parasitic power consumption during shutdown is substantial. As during start-up, many of the pumps and blowers are operating at full capacity to remove heat from the engine. The average parasitic power consumption during shutdown is 2.35-2.40 kW. Figure 5-56 shows the parasitic power curve for shutdown versus time. The engine during shutdown is slowly cooling, and thus the parasitic power is approximately constant. The step-down in parasitic power occurs when the brassboard fuel cell stack stops producing power and various pumps, blowers, heaters, etc. stop operating.

Conclusion

The efficiency penalty associated with methanol consumption and parasitic power usage during startup and shutdown are significant. This is especially true for the transportation application where, for example, a city bus is started and shutdown daily. The effect on efficiency is considerable, and should be taken into account when comparing different propulsion technologies. For transit buses that, on average for a 18 hour day, operate at power levels between 25-50% of design power output, the efficiency can be lowered by 5-7% due to startup and shutdown energy usage.

An interesting calculation is to determine the length of time an engine would need to operate to achieve 90% of its steady-state performance including the energy

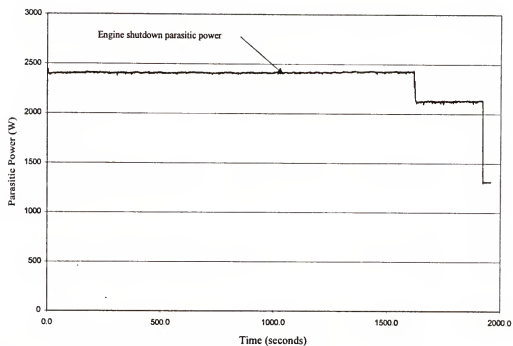


Figure 5-56: Parasitic power consumption curve for engine shutdown.

required for startup and shutdown. Table 5-8 presents the time required to achieve 90% of the steady state efficiency when startup and shutdown energy costs are accounted for. The results further indicate the efficiency penalty associated with operating at low power outputs.

Table 5-8: Time to achieve 90% of steady-state efficiency if startup/shutdown included.

% of Design Power	Power output (Watts)	Fuel Rate (g/min)	Net Power (kW)	Time required (hours)
25%	7016	102.1	4625	6.75
37.5%	10518	104.3	8179	3.75
50%	13826	114.75	11493	2.75
62.5%	17486	142.05	14875	2.75
75%	20982	169.95	17957	1.75

Aging Considerations

Introduction

The performance of the brassboard fuel cell engine has degraded over time. Originally designed as a 25 kW fuel cell engine, the maximum power output was probably closer to 30 kW. Ten years later, the maximum power output is approximately 21 kW. This is not terrible degradation considering the brassboard engine was a prototype and has been extensively used as a research and learning tool.

The reduction in catalyst performance and the loss of stack electrolyte are the primary causes of the engine performance degradation. When the reformer catalyst is deactivated, the conversion percentage of fuel mix to hydrogen rich gas is lowered. Platinum catalyst is used in the anode and cathode electrode. As the catalyst ages, the platinum becomes sintered resulting in less catalyst area. Corrosion of the support carbon also causes loss of platinum. Loss of phosphoric acid electrolyte reduces fuel cell stack performance by increasing the resistance to ion transfer.

Reformer Degradation

Table 5-2 details the degradation of the reformer catalysts. The degradation has not been severe, but has resulted in lower conversions of methanol at higher power outputs. It appears that all parts of the catalyst bed are still reforming, just at a reduced rate. This is shown by the controllable reformer bed temperatures. If a portion of the bed had severely degraded, the temperature would be higher than other parts of the bed. This is because heat would be added to the bed but little or no heat would be removed due to the lack of the reforming reaction.

The 50 kW fuel cell engine installed in the bus currently at the University of Florida has a steam reformer with a portion of the bed that has been severely degraded. Figure 5-57 shows the problems associated with the catalyst bed temperatures of a damaged reformer. The bottom bed temperature is rapidly increasing because no reforming (heat removal) is taking place. The middle bed temperature, where most of the reforming is occurring, is dropping. The result is further overheating and degradation of the catalyst bed to maintain operating temperatures.

The catalyst used by the steam reformer is not expensive. Replacement is not difficult if access has been incorporated into the reformer design. Replacement and reduction of the catalyst is the solution for this degradation.

Stack Degradation

Degradation of the stack platinum catalysts results in lower cell voltage. This means that a greater percentage of the reaction enthalpy is converted to heat rather than electrical power. The degradation is evident in Figure 5-3 which shows the reduction in

the polarization curve over time. The reduction in voltage is not all due to stack degradation, as reformer degradation also leads to lower stack voltage.

The stack currently is one of the most expensive components of a fuel cell engine. Most stacks are hand-assembled, and replacements are difficult if not impossible on many engines to obtain. Therefore, the life of an engine is typically determined by the life of the fuel cell stack.

The degradation in brassboard fuel cell engine performance is reasonable for its ten year life. Its substantial performance is due to many reasons, but primarily two main reasons. The first is that the brassboard was designed with additional margin, such as additional reformer catalyst. Weight was not a problem, so additional catalyst was added. The other is the environment and accessibility. The brassboard has an open layout which provides easy access to many components which makes debugging of problems much easier.

The principal result of the brassboard degradation is that the stack produces a lower cell voltage. This means for a given power output, the stack must now produce a higher current than when new. Figure 5-58 shows the curve of the stack current for a given power output in 1989 (new) and 1999. As expected, the current is lower for the 1989 data. The flow rate of primary methanol is a function of stack current (equation 5.2). Therefore, when the system was new, less primary methanol was required for a given power level.

The result of lower cell voltage is that more waste heat is produced in the fuel cell stack. Because the brassboard uses methanol very inefficiently to add heat to the coolant, the increase in primary methanol flow (pump P-01) is offset by a reduction in

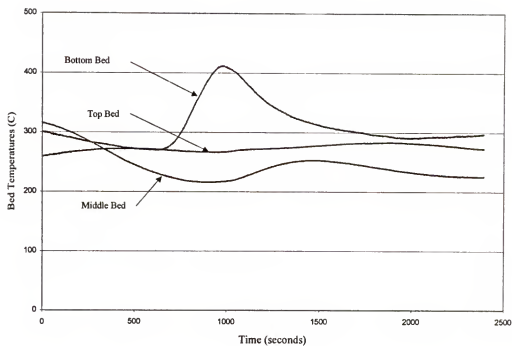


Figure 5-57: Catalyst bed temperatures for the 50 kW bus fuel cell engine. The bottom bed has been severely damaged resulting in high bed temperatures.

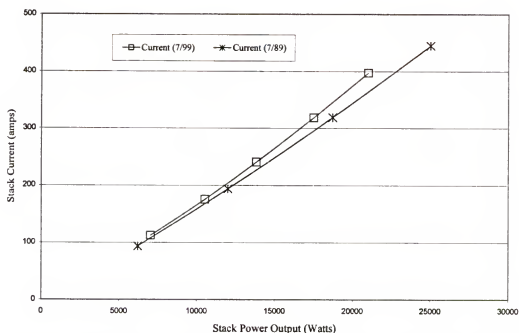


Figure 5-58: Graph showing the increased stack current due to brassboard degradation.

startup burner methanol (P-04) at low power outputs. This is clearly shown in Figure 5-59 which graphs the system efficiency from acceptance testing (1989) and current steady state tests (1999). The system efficiency is actually higher now in certain operating areas (≈ 40 to 50% of design power output). This occurs because the additional stack waste heat produced reduces P-04 methanol more than the increase in P-01 methanol. It should be noted that at high power outputs the system efficiency now is lower (42% versus 37%). This is because the additional waste heat produced by the stack is not useful since there is excess heat available within the engine.

Conclusion

The performance of the brassboard has held up well during the last ten years. As expected, the performance has degraded close to 10% at high power outputs. The fact that the system efficiency is higher at some operating points currently than when the engine was new is not a positive sign. Rather this fact strongly emphasizes how inefficiently the engine uses the auxiliary methanol.

Emissions

Introduction

The electrochemical combination of hydrogen and oxygen to form water and electricity results in zero regulated emissions. Because of this, fuel cells are often referred to as zero-emission devices. Fuel cell engines that operate on a liquid hydrocarbon fuel or alcohol, however, are not zero emission devices. Emissions occur from the burning of the primary fuel as well as residual reformat. Fuel cell engines that utilize pure hydrogen indirectly produce emissions from the manufacture of hydrogen.

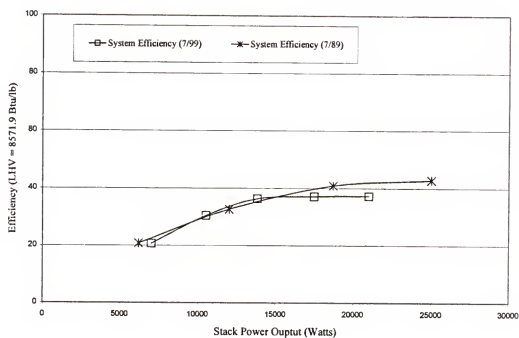


Figure 5-59: System efficiency curves for the brassboard engine when new (1989) and after 10 years of operation (1999).

In the United States, virtually all hydrogen is manufactured from natural gas and the process produces emissions.

The emission levels from fuel cell engines has the capability to be very low. The low temperature, low pressure burning processes in a properly designed system should achieve very low emissions levels. If additional clean-up devices such as catalytic converters are employed, the levels could drop to near background.

To determine the level of regulated emissions from a fuel cell engine data from multiple sources are used. The brassboard emissions are tested utilizing a COSA engine emission analyzer and a SRI gas chromatograph. For added information, the results of the fuel cell bus emissions testing are also included, which tested the 50 kW fuel cell engine version of the brassboard engine. The bus testing was completed by the West Virginia (WVU) Emissions Testing Laboratory over a 30 day period in March-April 1997. The University of Florida was involved in developing the data acquisition system for the vehicle as well as data reduction of the emissions test results. In addition, comparisons are made to limited data provided by Fuji Electric, the brassboard manufacturer.

Emissions Testing

The brassboard engine has three exhaust ports. The stack cathode exhaust consists of partially oxygen-depleted air heavily saturated with water vapor. Testing at WVU showed no regulated emissions from this port, as expected. The HX-03 heat exchanger exhaust port consists of either air (cooling) or combustion product (heating). The burner B-02 is operated in an on/off fashion, with a constant flow of liquid

methanol and constant flow of air. Thus the emissions level are either zero or a repeatable level based on B-02 status.

The main sources of emissions occur from the reformer exhaust port. The burner B-01 is always operating during power production, and combusts a variety of fuels, including liquid methanol, vaporized methanol, and stack flue gas. The stack flue gas is the same as reformat but with 60-80% of the hydrogen removed.

The brassboard engine exhausts were analyzed for carbon monoxide (CO) and oxides of nitrogen (NO_x) using the COSA engine emissions analyzer and the SRI gas chromatograph. Carbon dioxide (CO₂), although not a regulated emission, was also measured using the gas chromatograph as were hydrocarbon (HC) levels. Testing at WVU showed that during normal operation, the HC concentration trends were similar to the CO concentration trends. In other words, when CO increased, so did the hydrocarbons. Therefore, the CO level is also used as an indicator of the HV level.

The emissions testing at WVU was complete. The CO, NO_x, HC, and particulate matter (PM) levels were measured using exhaust dilution tunnel and real-time emission measuring equipment. In addition, methanol levels were measured using impingers and gas chromatograph analysis. The aldehyde levels were also measured. The alcohols and aldehydes were combined and reported as organic material hydrocarbon equivalent (OMHCE).

Steady-State Brassboard Testing

Emissions during the steady state power output testing were analyzed using the COSA engine emission analyzer (COSA) and the SRI gas chromatograph (GC). Gas sampling ports were installed on the reformer and HX-03 exhaust ports. Gas sampling

bags were employed to collect samples of exhaust gas for GC analyses. This testing occurred over many months to learn the expected levels of emissions at different operating levels.

The COSA was then connected, at different times, to the two exhaust ports to allow continuous monitoring of the exhaust stream. Emission levels were recorded by computer and when combined with the existing data acquisition system allowed clear insight into the level and causes of emissions.

Reformer exhaust port

Carbon monoxide levels in the reformer burner exhaust come from two primary sources. The primary fuel flow for the reformer burner is stack flue gas which is approximately 4% CO. In addition, small quantities of methanol from the reformer burner methanol trim pump P-03 are combusted.

Figures 5-60 through 5-63 show the CO levels for 25%, 37.5%, 50%, and 62.5% of design power output for the reformer burner exhaust port as measured by the COSA. The CO levels agree closely with those determined by the GC analysis. For the 50% and 62.5% cases (Figures 5-62 and 5-63 respectively), the CO levels are fairly constant and at a low level (below 30 parts per million or ppm). The 25% and 37.5% cases (Figures 5-62 and 5-63 respectively) are not constant but depend on the output from the methanol trim pump P-03. As the methanol flow rate is increased, the CO levels decrease. There is a definite trend of higher average CO levels with decreasing power output.

The air flow into the burner is constant, so the combustion temperature is dependent on the amount of fuel. As the power output increases, the total heating value

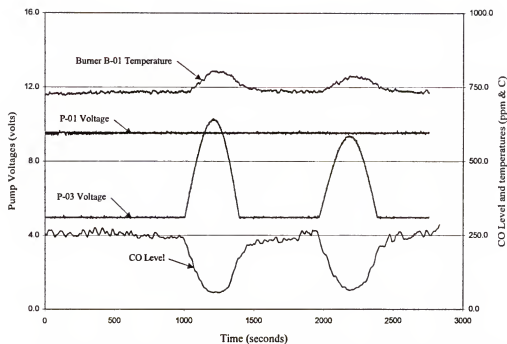


Figure 5-60: Carbon monoxide levels for the brassboard engine operating at 25% of design power output.

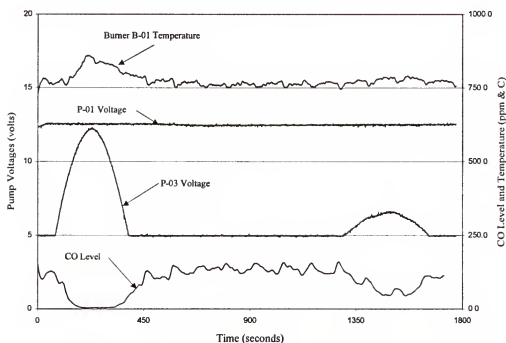


Figure 5-61: Carbon monoxide levels for the brassboard engine operating at 37.5% of design power output.

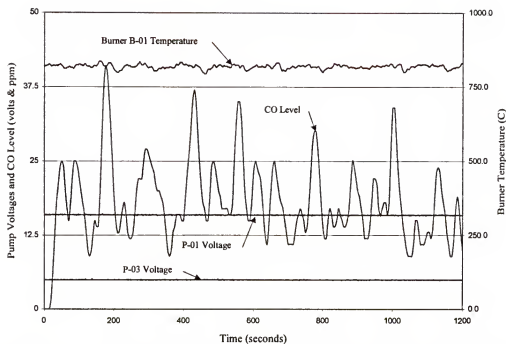


Figure 5-62: Carbon monoxide levels for the brassboard engine operating at 50% of design power output.

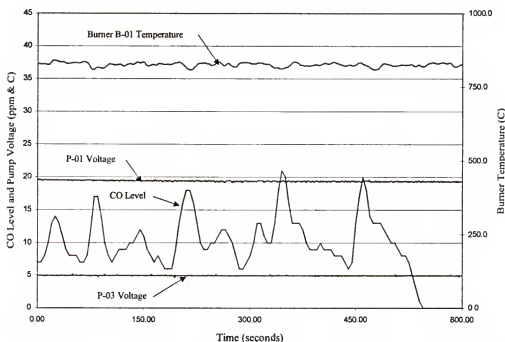


Figure 5-63: Carbon monoxide levels for the brassboard engine operating at 62.5% of design power output.

of the fuel delivered to the burner increases (more hydrogen gas). The result is that the burner thermocouple reading increases as the power output increases. It also increases as the P-03 methanol output increases. There is a direct correlation between the burner thermocouple reading and the CO level, and as the thermocouple reading increases, the level of CO decreases.

The reduction in CO may be caused by a number of factors. The position of the flame within the burner can may allow for better atomization of the P-03 methanol at different fuel flow rates. The temperature of the flame increases with additional fuel, resulting in faster reaction rates. The faster reaction rates will result in more complete combustion of the CO.

Transit bus emission testing showed a similar decrease in CO levels as the reformer trim pump increased methanol output. Figure 5-64 shows the result of testing the bus fuel cell engine at 24.5 kW output (50% of design power output). As the trim pump output increased, the CO levels decreased. The bus testing showed higher emission levels at higher power outputs as compared to lower levels with the brassboard. This is probably because the reformer burner blower on the vehicle changes air flow rate with power output, therefore changing burner temperature, etc.

The hydrocarbon levels of exhaust streams were not detectable with the GC. Gas chromatograph testing of the reformat showed levels of approximately 100 ppm, primarily from contaminants in the methanol. The residual reformat is the primary fuel for the reformer burner, and testing of the exhaust gas showed no detectable levels of HC. Bus testing showed low HC levels with similar curve shapes to CO. The HC curve for 50% of design power output for the bus engine is also shown in Figure 5-64.

Nitrous oxides were not detected by the COSA. This is similar to the results from WVU which showed NO_x levels equal to background. Particulate matter levels were very low during testing at WVU. Comparison to other transit buses showed levels at least 20-30 times lower than other liquid-fueled vehicles (similar levels to natural gas buses).

HX-03 Exhaust

HX-03 exhaust consists of either air when used for cooling or combustion product when HX-03 is used for heating. Below 50% power output, burner B-01 is used to add heat to the coolant. The burner is operated in an on/off fashion, as previously described. Figure 5-65 shows the curve of CO for the HX-03 exhaust port. The shape of the CO curve is expected, increasing as ignition first occurs and then dropping off to approximately 20 ppm until the methanol flow is stopped. The 20 ppm level agrees very closely with the results of GC testing.

The curve is similar whenever the burner is turned on (see startup emission results), and the total emission levels are dependent upon how often the burner is used. At low power outputs the burner is used more often, decreasing steadily until 50% of design power output is reached and the burner is no longer operated.

Total emission levels

Table 5-9 lists the CO data for the various power outputs and all exhaust ports. The flow rate of combustion product is approximately constant for each exhaust port, and so the parts per million (ppm) reading is directly related to the CO level. The table clearly shows that the CO levels are considerably higher at low power output, with the

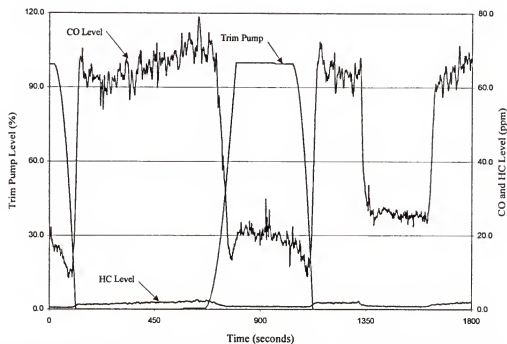


Figure 5-64: Graph of the CO and HC levels for the 50 kW bus fuel cell engine.

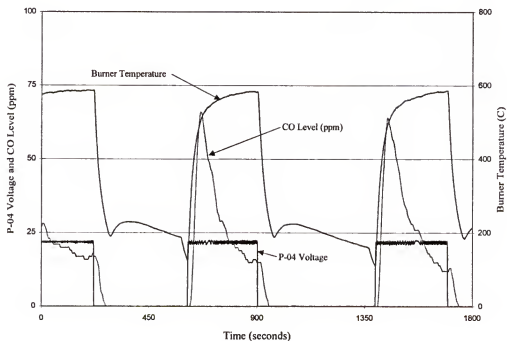


Figure 5-65: Graph of the CO level for the HX-03 exhaust port at 25% of design power output.

total grams of CO at 25% of design power output equaling 25 times the amount at 62.5%. The data is similar to data presented by Fuji during acceptance testing of the brassboard engine. The Fuji testing was probably instantaneous data whereas University of Florida (UF) data is a time average. Table 5-10 compares Fuji data with recent brassboard testing. Also included is Fuji HC data.

Table 5-9: Carbon Monoxide (CO) levels for the brassboard fuel cell engine.

Power Level	Reformer CO (average ppm)	Reformer CO (g/hr)	HX-03 CO (average ppm)	HX-03 CO (g/hr)	Total CO (g/hr)
25%	210.4	26.7	12.8	4.81	31.51
37.5%	94.9	12.24	5.98	2.22	14.46
50%	18.27	2.40	0.0	0.0	2.4
62.5%	9.42	1.26	0.0	0.0	1.26

Table 5-10: Comparison of emission testing of brassboard engine by the University of Florida (UF) and Fuji.

Power Level	UF Ref. CO (average ppm)	Fuji Ref. CO (ppm)	UF HX-03 CO (average ppm)	Fuji HX-03 CO (ppm)	Fuji Total HC (ppm)
25%	210.4	140	12.8	10	8
37.5%	94.9		5.98		
40%		150		40	8
50%	18.27	20	0.0	nil	nil
62.5%	9.42		0.0		
75%		20		nil	nil
100%		30		nil	nil

Emission results are often stated in normalized terms such as (g/bhphr).

Normalizing the emission levels allows more accurate comparison of different engine operating conditions. In the case of the brassboard, normalizing the levels to power output further details the emission penalty associated with low power output operation. Table 5-11 lists the normalized CO levels based on gross and net engine power output. Based on net power output, the CO levels at 25% of design power output are approximately 80 times the value at 62.5%. The trends show the CO level decreasing

with increasing power output, so it would be expected the normalized CO levels would drop further with increasing power output. Table 5-11 further highlights the emission penalty associated with low power operation.

Table 5-11: Carbon Monoxide (CO) levels for the brassboard fuel cell engine.

Power Level	Reformer CO (g/hr)	HX-03 CO (g/hr)	Total CO (g/hr)	CO level (g/hphr _{gross})	CO level (g/hphr _{net})
25%	26.7	4.81	31.51	6.02	9.14
37.5%	12.24	2.22	14.46	1.84	2.37
50%	2.40	0.0	2.4	0.233	0.280
62.5%	1.26	0.0	1.26	0.0967	0.114

Startup/Shutdown/Idle Operation

Startup and shutdown emissions for the brassboard engine are important primarily because the time required (37.5 and 30 minutes, respectively) are lengthy. During startup, liquid and vaporized methanol are combusted in the reformer burner. Liquid methanol is combusted in the startup burner nearly continuously. During idle operation, internal heaters are used to dissipate stack electrical power, and as such the startup burner is not used. Also during idle, the reformer burner operates with additional hydrogen as compared to the 25% of design power output resulting in higher flame temperatures. During shutdown, the startup burner is not used. The reformer burner emissions are similar to the idle condition.

Startup Process

During startup, the reformer burner initially combusts liquid and vaporized methanol (mode 1). Once the reformer catalyst bed has reached its operating temperature, the liquid methanol flow to the reformer burner is stopped. The fuel mixture flows through the reformer and the reformat is bypassed directly to the

reformer burner, providing a high flow rate of hydrogen into the burner (mode 2). Eventually, the reformat flows though the stack where 60-80% of the hydrogen is consumed and the residual gas (stack flue gas) returns to the reformer burner. To show the CO level, two curves have been used. The first curve shows when the liquid and vaporized methanol flow is used as reformer burner fuel. The second curve shows when the fuel mixture is the primary reformer burner fuel.

Figure 5-66 shows the reformer burner exhaust CO levels during mode 1. During this mode the reformer burner is operated in an on/off fashion. When operating the burner, the fuel flow and air flow are constant. The CO level rises to approximately 600 ppm where it remains until the burner shuts down. This is repeated three times during mode 1 for this startup, which is typical. During mode 1, approximately 30-31 grams of CO are created.

Figure 5-67 shows the CO level during mode 2 of startup. The CO level changes dramatically during this mode as the fuel flow rate and air flow rate (indicated by F-01 voltage) are changing. The burner thermocouple temperature quickly rises to above 1000 °C and the CO drops. Towards the end of the startup mode 2, the air flow to the burner is reduced and part of the hydrogen gas within the reformat is consumed by the stack. The burner thermocouple temperature is reduced, and the CO level begins to increase and then levels off. Considerably less CO is produced during this mode of startup, with only 1.9-2.0 grams. The total CO produced for the reformer burner during startup was approximately 33 grams.

Although difficult to quantify according to individual specie, the GC testing showed significant quantities of HC during mode 1. Similar results were obtained for

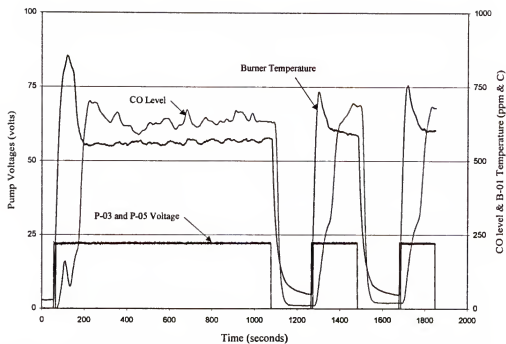


Figure 5-66: Startup CO levels for the reformer burner exhaust during mode 1.

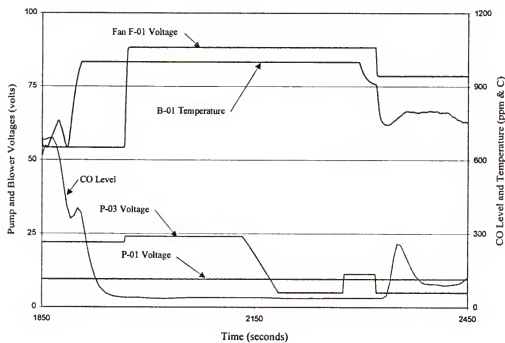


Figure 5-67: Startup CO levels for the reformer burner exhaust during mode 2.

the bus emissions. This is due to contaminants within the methanol that are not combusting when entering the reformer burner in liquid form. The NO_x and PM were again very low levels.

The startup burner operates almost continuously during startup. Figure 5-68 shows the CO level for the HX-03 exhaust during startup. The CO levels are similar to Figure 5-65, the HX-03 exhaust during 25% of design power output. The total mass of the CO produced in the HX-03 exhaust during startup is 5.5 grams.

This total mass of CO produced during startup for all exhaust lines is approximately 38.5 grams. This is a considerable amount when compared to the g/hr produced at 62.5% of design power output. This mass of CO is equivalent to producing 455 kW-hours of electricity (net) at 62.5%. This highlights the considerable CO produced during startup. The results of bus testing showed the HC produced during startup was the equivalent of approximately 400 kW-hours of electricity (net) at 100% of design power. Both the CO and HC produced during startup are a significant part of the emissions produced during a typical transit bus daily route.

Shutdown

The emissions from shutting down the engine are substantially less than startup. HX-03 does not operate, and additional hydrogen is available for the reformer burner. The higher reformer burner flame temperature results in lower levels of emissions than at 25% or 37.5 % of design power.

Figure 5-69 shows the CO levels during shutdown from the reformer burner exhaust port. As the engine cools, more hydrogen is available to the reformer burner. The burner temperature therefore climbs slowly from 810 to 840 °C. The CO level

drops from 50 ppm to 5 ppm during this period. Once the fuel cell stack has sufficiently cooled, the fuel flow is stopped. The CO level increases to approximately 450 ppm. The increase in CO is probably due to residual vaporized methanol exiting HX-05 and entering the reformer burner after the flame has been extinguished. The methanol breaks down resulting in CO production. The total CO produced during shutdown is 4.5 grams, with 3 grams occurring in the last 5 minutes after the burner flame is out.

Bus testing showed similar levels of CO during shutdown. In addition, very low levels of HC were produced because no liquid methanol was combusted. NO_x and PM levels were also very low if detectable at all.

Idle condition

The idle condition is standby operation where the power produced by the stack is dissipated in engine heaters. The brassboard is not designed to operate in this condition for long periods or it will overheat. It is primarily a transitional state, such as from startup to power producing. The startup burner does not operate because the heaters provide energy to the coolant. The reformer burner temperature is high because of additional hydrogen available, just as during shutdown. Shutdown, is in fact, idle operation with lowering engine temperatures.

Figure 5-70 shows the CO levels during idle operation. The average CO level is approximately 95 ppm, which is approximately the same as 37.5% of design power output. The CO is produced at 12 grams an hour, which means that substantial CO is produced for zero net power output. For every minute idling, the system could operate at 62.5% of power output for 120 minutes, which is equivalent to 30 kW-hr of

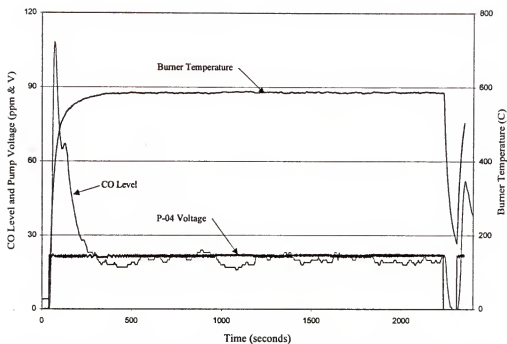


Figure 5-68: Carbon monoxide level for the HX-03 exhaust port during startup.

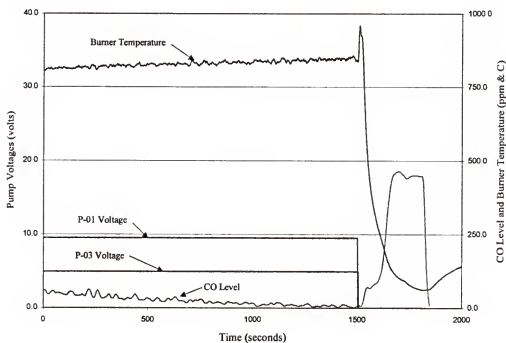


Figure 5-69: Carbon monoxide levels for the reformer exhaust port during shutdown.

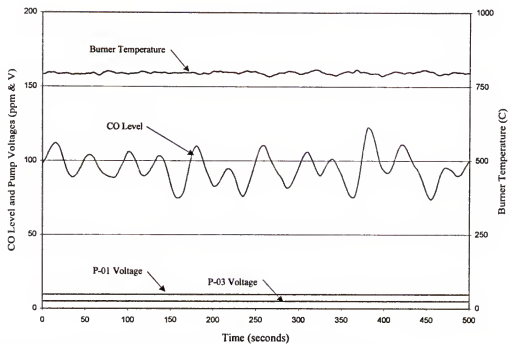


Figure 5-70: Carbon monoxide levels for the idle condition.

electricity (net). Testing of the 50 kW fuel cell engine resulted in approximately double the CO during idle as the brassboard (10 kW stack output versus 6.25 kW stack output).

Conclusions

Emissions testing of the brassboard was successfully completed utilizing the COSA engine emission analyzer and the GC. The CO and NO_x levels were directly recorded by the COSA. The CO levels were verified using the GC. Hydrocarbon levels were quantified, and comparisons to the bus 50 kW emissions testing showed similar patterns to HC production.

Emission levels for the brassboard fuel cell engine are low at high power outputs. The engine has been optimized for the design point (25 kW stack output), and as a result the emission levels are substantially higher at low power outputs. In addition, the emission levels for startup and shutdown are significant, and would substantially increase emission level averages even for an 18 hour daily transit bus schedule.

Carbon monoxide is the most prevalent of the regulated emissions. Testing of the 50 kW fuel cell engine resulted in CO levels similar to that of new diesel buses and considerably above expected levels. The bus 50 kW engine testing also showed, however that PM and NO_x levels were very low. COSA testing of the brassboard verified the low levels of NO_x. Hydrocarbons were detected for the brassboard at similar operating conditions as high HC levels on the bus fuel cell engine.

CHAPTER 6 CONCLUSIONS AND RECOMMENDATIONS

Conclusions

The brassboard fuel cell engine operated extremely well during testing. It started reliably and performed strongly throughout the numerous different tests performed over a two year period. The results were consistent and predictable, and comparison of the past four years of testing at the University of Florida showed the engine performance had minimal degradation. The existing control strategy was simple and limited but effective, and the numerous components, even after ten years of operation, worked as they were designed.

The laboratory layout of the brassboard engine was beneficial. Most fuel cell engines are packaged very tightly to allow integration into a vehicle, thus minimizing access to many of the components. The open layout of the brassboard engine is favorable for many reasons. Components are easily accessed which allows easy removal and repair. Data acquisition transducers were freely installed resulting in a better understanding of performance. Finally, the stand-alone nature of the engine allowed for flexibility tests without any vehicle constraints.

The data acquisition system installed worked well. The system was adaptable allowing more and more signals to be added until a complete performance map of the engine was developed. The real-time viewing of the data in a usable form such as graphs led to a critical insight into the engine performance. The data acquisition system

was also invaluable in aiding the debugging process when the engine had difficulties. The immense amount of acquired data allowed quick pinpointing of the problem area and led to quick and successful resolutions.

The extensive testing resulted in a clear understanding of a complete fuel cell engine efficiency through utilization of the brassboard, thus achieving one of the primary goals of this research. A variety of efficiency definitions were employed to document step-by-step the causes of efficiency losses. The losses associated with the electrochemical conversion process, the fuel reforming process, the auxiliary fuel flows, power conditioning, and parasitic power consumption were defined. The result was a net overall engine efficiency that ranged from 13.6% at low power outputs to 32% at higher power outputs.

The net overall engine efficiency for the brassboard is well below most published values for fuel cell systems. There are many reasons for this including that most published data is based on overly optimistic models. Also, the testing of the brassboard was complete, accounting for losses often ignored, such as the power consumed by the control computer and auxiliary subsystems. The testing was completed over a range of power outputs resulting in a map of efficiency rather than the design point efficiency as often shown in the literature.

More was achieved than just determining the efficiency of the brassboard engine. Great effort was put forth to characterize and develop a fundamental understanding of the root causes of fuel cell engine performance characteristics. Often the fuel cell stack receives most of the design effort, and it is indeed the single most important component in the engine. What this testing showed, however, was that

components and control strategies can substantially alter the engine performance. It is this lack of fundamental understanding of engine behavior that often results in engines that perform well below expectations.

Constant air flow into the reformer burner, for example, resulted in poor utilization of the available energy at low power outputs, resulting in increased fuel usage. The amount of energy lost in the exhaust is approximately constant but is much greater at low power in relative terms. Changing the air flow would allow more of the energy to be utilized by the catalyst bed and less of the energy to leave in the exhaust stream. Another example is the startup burner heat exchanger. It is not insulated because at high power output the lack of insulation aids the removal of excess heat from the engine. However, at low power when less excess heat is available, the large convective heat losses result in dramatically increased methanol consumption. The methanol consumed by the startup burner at 25% of design power output is approximately 60% of the primary fuel flow. The problem, once understood, can be solved by many means such as bypassing the heat exchanger at low power to avoid the large convective losses.

The simple steps outlined above would significantly improve the engine performance at low power outputs. As shown in Figure 5-28, the fuel cell stack produces more waste heat than is required to vaporize the fuel mixture, even at low power outputs. The net result is that it may be possible through the use of the bypass valve and appropriate insulation to eliminate the fuel for the startup burner during normal operation. Eliminating the P-04 methanol flow rate would increase the efficiency at 25% of design power output by as much as 40%, quite significant.

Startup and shutdown performance was also analyzed. The quantity of both methanol and electricity consumed during startup and shutdown is significant, and strongly impacts the engine efficiency. Table 5-8 shows that it takes 2-7 hours of operation (depending upon power level) to achieve 90% of the steady-state efficiency. Considering that the steady-state efficiency is already lower than expected or hoped for, this further reduction is very costly.

Fuel cell systems or engines are often referred to as zero emission vehicles. Although it is true that electrochemically combining hydrogen and oxygen to form water and electricity does not produce regulated emissions, an engine operating on methanol typically will produce emissions. The extent to which the engine produces emissions is dependant on component selection, control strategy, etc. For the brassboard engine, the primary concern is the level of CO. The CO emissions levels at high power output are low, typically on the order of 5-20 ppm at the design point, which corresponds to CO levels of $<0.25 \text{ g/hphr}_{\text{NET}}$. Problems occur, however, at the low power outputs. The CO level at 25% of design power output is approximately 40-80 times those of the high power outputs on a normalized basis, and 20-25 times the high power output case in grams per hour. This is due to many factors, including burner design, flame temperatures, burner air flow rates, etc. The net result is that the engine must not be operated at low power outputs for significant time periods to perform with low emissions.

In conclusion, a major goal of this research was to begin to develop a fundamental understanding of a complete fuel cell engine. This was accomplished by developing a comprehensive data acquisition system in conjunction with the unique 25

kW brassboard, methanol-fueled, liquid-cooled, phosphoric acid fuel cell engine. The efficiency losses were documented including losses associated with the interaction between components. Finally, the levels of emissions were investigated as well as the sources of emissions and the reasons of the emissions production.

Recommendations

The brassboard fuel cell engine is approaching the end of its useful life. It still, however, can be used as a valuable research and teaching tool. The shortage of available fuel cell hardware will not end any time soon as more and more researchers are interested in this field of study. Because of this, it is imperative that the brassboard is maintained in working order to both teach and demonstrate fuel cell technology as well as conduct appropriate research.

The usefulness of the brassboard in developing the fundamental understanding of fuel cell engine behavior highlights the need for more laboratory style testing. Currently, the few engines manufactured are typically very compact to allow installation in vehicles, severely hindering their use as research tools. As such, more emphasis should be given to developing laboratory engines.

The results from the testing highlight the limitations of existing models and their architecture. Currently no existing generic model would come close to mimicking the brassboard engine behavior. The models are based on overly optimistic and simple representations with little or no control strategy or component interaction. Thus, for the fuel cell engines to further develop, intense interest and scrutiny in the modeling area is required.

REFERENCES

1. J. Mark, J.M. Ohi, and D.V. Hudson, *Fuel Savings and Emissions Reductions from Light-duty Fuel Cell Vehicles*, Golden, CO: National Renewable Energy Laboratory, 36-37, 1994.
2. Murray, H.S., et al., *DOT Fuel-Cell-Powered Bus Feasibility Study: Final Report*, Los Alamos, NM: Los Alamos National Laboratory, p. 349, 1986.
3. Prater, K., The Renaissance of the Solid Polymer Fuel Cell, *Journal of Power Sources*, 29, 239-250, 1990.
4. Directed Technologies, *Technology Development Goals for Automotive Fuel Cell Power Systems*, Cambridge, MA: U.S. Department of Energy: Office of Transportation Technologies, 20-35, 1994.
5. Pentastar Electronics Inc., *Direct-Hydrogen-Fueled Proton-Exchange-Membrane Fuel Cell System for Transportation Applications: Conceptual Design*, Huntsville, AL: U.S. Department of Energy: Office of Transportation Technologies, 1997.
6. Little, A.D., Hydrogen Storage for Transportation Fuel Cells, in *SAE Toptec: Fuel Cells for Transportation*, Diamond Bar, CA, 1-30, 1993.
7. Little, A.D., *Multi-Fuel Reformers for Fuel Cells Used in Transportation: Assessment of Hydrogen Storage Technologies*, Cambridge, MA: U.S. Department of Energy: Office of Transportation Technologies, p.174, 1995.
8. Little, A.D., *Multi-fuel Reformers for Fuel Cells Used in Transportation: Phase I Final report*, Cambridge, MA: U.S. Department of Energy: Office of Transportation Technologies, p.122, 1994.
9. Cengel, Y.A. and M.A. Boles, *Thermodynamics: An Engineering Approach*. 2nd ed, New York, NY: McGraw-Hill, Inc, p. 987, 1994.
10. Raman, V., The Hydrogen Fuel Option for Fuel Cell Vehicle Fleets, Detroit, MI: *SAE International Congress and Exposition*, 1-7, 1999.

11. Ford Motor Company, *Direct-Hydrogen-Fueled Proton-Exchange-Membrane Fuel Cell System for Transportation Applications: Hydrogen Infrastructure*, Dearborn, MI: U.S. Department of Energy: Office of Transportation Technologies, 1997.
12. Ogden, J.M., M.M. Steinbugler, and T.G. Kreutz, A comparison of hydrogen, methanol, and gasoline as fuels for fuel vehicles: implications for vehicle design and infrastructure development, *Journal of Power Sources*, 79, 143-168, 1998.
13. Roan, V.P., Comparison of several alternative fuels for fuel cell vehicle applications, Piscataway, NJ: *Proceedings of the 1994 29th Intersociety Energy Conversion Engineering Conference*, 1083-1089, 1994.
14. Teagan, W.P., J. Bentley, and B. Barnett, Cost reductions of fuel cells for transport applications: fuel processing options, *Journal of Power Sources*, 71, 80-85, 1998.
15. Mitchell, W.L., M. Hagan, and S.K. Prabhu, *Gasoline Fuel Cell Power Systems for Transportation Applications: A Bridge to the Future of Energy*, Detroit, MI: SAE Technical Paper Series, 1-7, 1999.
16. Voecks, G.E., Onboard Production of Hydrogen for Vehicular Systems. Boulder, CO: *Proceedings: Renewable Fuels and Advanced Power Sources for Transportation Workshop*, 139-144, 1982.
17. Amphlett, J.C. and M.J. Evans, Hydrogen Production by the Catalytic Steam Reforming of Methanol Part 1: Thermodynamic, *The Canadian Journal of Chemical Engineering*, 59, 720-727, 1981.
18. Amphlett, J.C., *et al.*, Hydrogen Production by the Catalytic Steam Reforming of Methanol. Part 2: Kinetics of Methanol Decomposition Using Girdler G66B Catalyst, *The Canadian Journal of Chemical Engineering*, 63, 605-611, 1985.
19. Amphlett, J.C., *et al.*, Production of Hydrogen Rich-Gas by Steam Reforming of Methanol Over Copper Oxide--Zinc Oxide Catalysts, Piscataway, NJ: *Proceedings of the 20th Intersociety Energy Conversion Engineering Conference*, 2, p. 2.772, 780, 1985.
20. Amphlett, J.C., R.F. Mann, and R.D. Weir, Hydrogen Production by the Catalytic Steam Reforming of Methanol. Part 3: Kinetics of Methanol Decomposition Using C18HC Catalyst, *The Canadian Journal of Chemical Engineering*, 66, 950-956, 1988.
21. Ganser, B. and B. Holein, *Hydrogen From Methanol: Fuel Cells in Mobile Systems*, Institute of Energy Process Engineering (IEV), 117-127, 1992.

22. Bentley, J., B.M. Barnett, and S. Hynek, Multi-Fuel Reformer and Hydrogen Storage, Tucson, AZ: *1992 Fuel Cell Program and Abstracts*, 456-460, 1992.
23. Amphlett, J.C., *et al.*, Methanol, Diesel Oil, and Ethanol as Liquid Sources of Hydrogen for PEM Fuel Cells. Piscataway, NJ: *Proceedings of the 1994 28th Intersociety Energy Conversion Engineering Conference*, 1221-1226, 1993.
24. Ledjeff-Hey, K., *et al.*, Compact Hydrogen Production Systems for Solid Polymer Fuel Cells, *Journal of Power Sources*, 71, 199-207, 1998.
25. Peppley, B.A., *et al.*, Hydrogen Generation for Fuel-Cell Power Systems by High Pressure Catalytic Methanol-Steam Reforming. Piscataway, NJ: *Proceedings of the 1997 32nd Intersociety Energy Conversion Engineering Conference*, 1, 831-836, 1997.
26. Cheng, Y.-L., L.D. Chen, and J.P. Seaba, Thermodynamic Analysis of Fuel Processing. Detroit, MI: *SAE International Congress and Exposition*, 1-5, 1999.
27. Springer, T.E., H.S. Murray, and N.E. Vanderborgh, Methanol Reformer System and Design for Electric Vehicles, Piscataway, NJ: *Proceedings of the 20th Intersociety Energy Conversion Engineering Conference*, 1, 1.723-1.728, 1985.
28. Dusterwald, H.G., *et al.*, Methanol Steam-Reforming in a Catalytic Fixed Bed Reactor, *Chemical Engineering Technology*, 20, 617-623, 1997.
29. Ohl, G.L., J.L. Stein, and G.E. Smith, Fundamental Factors in the Design of a Fast-Responding Methanol-to-Hydrogen Steam Reformer for Transportation Applications, *Journal of Energy Resources*, 118, 112-119, 1996.
30. Kumar, R., *et al.*, Methanol Reformers for Fuel Cell Powered Vehicles: Some Design Considerations, Phoenix, AZ: *1990 Fuel Cell Program and Abstracts*, 76-79, 1990.
31. J.H.Hirschenhofer, D.B. Stauffer, and R.R. Englehauser, *Fuel Cells: A Handbook (Revision 3)*, Morgantown, WV: Morgantown Energy Technology Center, 1994.
32. Blomen, L.J. and M.N. Mugerwa, eds. *Fuel Cell Systems*. First ed., New York: Plenum Press, p. 614, 1993.
33. Cairns, E.J. and H.A. Liebhafsky, *The thermodynamics of a complete fuel cell*, Schenctedy, NY: General Electric Research Laboratory, p. 39, 1963.
34. Berger, C., *Handbook of Fuel Cell Technology*. First ed, ed. C. Berger, Englewood Cliffs, NJ: Prentice-Hall, p. 607, 1968.

35. Bernadi, D.M. and M.W. Verbrugge, A Mathematical Model of the Solid-Polymer Electrolyte Fuel Cell, *Journal of the Electrochemical Society*, 139, 2477-2491, 1992.
36. Lee, J.H. and T.R. Lalk, A Modeling Technique for Fuel Cell Stack Systems, *Proceedings of the ASME Dynamics Systems and Controls Division*, 58, 107-116, 1996.
37. Wohr, M., *et al.*, Dynamic Modeling and Simulation of a Polymer Membrane Fuel Cell Including Mass Transport Limitations, *International Journal of Hydrogen Energy*, 23, 213-218, 1998.
38. Rodrigues, A., *et al.*, Carbon Monoxide Poisoning of Proton-Exchange Membrane Fuel Cells, Piscataway, NJ: *Proceedings of the 1997 32nd Intersociety Energy Conversion Engineering Conference*, 768-773, 1997.
39. Paffett, M.T., *et al.*, The treatment of CO poisoning in low temperature fuel cells by the injection of oxygen or air into the anode fuel stream, Phoenix, AZ: *1990 Fuel Cell Seminar*, 441-444, 1990.
40. Mitsuda, K. and T. Murahashi, Characterization of gas flow configurations for phosphoric acid fuel cells, *Journal of Applied Electrochemistry*, 21, 395-401, 1991.
41. Springer, T.E., T.A. Zadowski, and Gottesfeld, Polymer Electrolyte Fuel Cell Model, *Journal of the Electrochemical Society*, 138, 2334-2342, 1991.
42. Amphlett, J.C., *et al.*, Performance Modeling of the Ballard Mark IV Solid Polymer Electrolyte Fuel Cell: Mechanistic Model Development, *Journal of the Electrochemical Society*, 142, 1-8, 1995.
43. Amphlett, J.C., *et al.*, Performance Modeling of the Ballard Mark IV Solid Polymer Electrolyte Fuel Cell: Empirical Model Development, *Journal of the Electrochemical Society*, 142, 9-15, 1995.
44. Amphlett, J.C., *et al.*, Parametric modelling of the performance of a 5-kW proton-exchange membrane fuel cell stack, *Journal of Power Sources*, 49, 349-356, 1994.
45. Amphlett, J.C., *et al.*, A model predicting transient responses of proton exchange membrane fuel cells, *Journal of Power Sources*, 49, 183-188, 1996.
46. Amphlett, J.C., *et al.*, Simulation of a 250 kW diesel fuel processor/PEM fuel cell system, *Journal of Power Sources*, 71, 179-184, 1998.

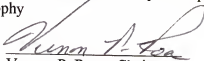
47. Sutton, R.D. and N.E. Vanderborgh, Electrochemical Engine System Modeling and Development, Tucson, AZ: *1992 Fuel Cell Seminar*, 201-203, 1990.
48. Kinoshita, K. and A.R. Landgrebe, Analysis of power and energy for fuel cell systems, *Journal of Power Sources*, 47, 159-175, 1993.
49. Kumar, R., M. Krumpelt, and B. Misra, Fuel Cells for Vehicle Propulsion Applications: AS Thermodynamic Analysis, Piscataway, NJ: *Proceedings of the 24th Intersociety Energy Conversion Engineering Conference*, 3, 1601-1606, 1989.
50. Krumpelt, M., R. Kumar, and K.M. Myles, Fundamentals of fuel cell system integration, *Journal of Power Sources*, 49, 37-51, 1994.
51. Fletcher, J.H., *The Investigation of the Component and System Modeling of a Phosphoric Acid Fuel Cell System for Transportation Application*, Masters Thesis, University of Florida: Gainesville, FL, 1990.
52. Meyers, A.P., J.M. King, and D. Kely, *Progress in Development and Application of Fuel Cell Power Plants for Automobiles and Buses*, Detroit, MI: Society of Automotive Engineers, p. 5, 1999.
53. Roan, V.P. and J.H. Fletcher, Transient Performance Modeling and Considerations for Methanol-Fueled Phosphoric Acid Fuel Cell System Designed for the Transportation Application, Piscataway, NJ: *Proceedings of the 1990 25th Intersociety Energy Conversion Engineering Conference*, 301-307, 1990.
54. Holmquist, D.H., *The Investigation of Component Modeling and Interaction in Phosphoric Acid and Proton Exchange Membrane Fuel Cell Transportation Systems*, Masters Thesis, University of Florida: Gainesville, FL, 1995.
55. Geyer, H.K., R.K. Ahluwalia, and R. Kumar, Dynamic Response of Steam-Reformed, Methanol-Fueled, Polymer Electrolyte Fuel Cell System. Piscataway, NJ: *Proceedings of the 1996 31st Intersociety Energy Conversion Engineering Conference*, 2, 1101-1106, 1996.
56. Virji, M.B.V., *et al.*, Effect of operating pressure on the system efficiency of a methane-fuelled solid polymer fuel cell power source, *Journal of Power Sources*, 71, 337-347, 1998.
57. Barbir, F., Operating Pressure and Efficiency of Automotive Fuel Cell Systems, *International Journal of Hydrogen Energy*, 21, 891-907, 1996.

58. Oliveira, J.C.T., A. Anantaraman, and W.A. Adms, Performance Evaluation of a Hydrogen/Air PEM-FC System under Variable Load, Tucson, AZ: *1992 Fuel Cell Seminar*, 451-454, 1992.
59. Friedman, D.J., *Maximizing Direct Hydrogen PEM Fuel Cell Efficiency - Is Hybridization Necessary?*, Detroit, MI: Society of Automotive Engineers, 1-9, 1999.
60. Mark, J., *Environmental and Infrastructure Trade-offs of Fuel Choices for Fuel Cell Vehicles*, San Diego, CA: SAE Technical Paper Series, 1-8, 1997.
61. Arcadis Geraghty & Miller, *Evaluation of Fuel Cell Reformer Emissions*, Sacramento, CA: California Air Resources Board, p. 150, 1998.
62. ONSI Corporation, *PC25 Fuel Cell Power Plant Air Emissions*, Windsor, CT: ONSI Corporation, p. 2, 1995.
63. Wimmer, R.R., *et al.*, Emissions Testing of a Hybrid Fuel Cell Bus, Warrendale, PA: *SAE Technical Paper Series*, 265-274, 1998.
64. Arthur D. Little, *Energy Efficiency and Emissions of Transportation Fuel Chains*, Detroit, MI: Ford Motor Company, p. 100, 1996.
65. Energy Research Corporation, *Research and Development of a Fuel Cell/Battery Powered Bus System*, Danbury, CT: U.S. Department of Energy, p. 137, 1990.
66. Booz Allen & Hamilton, *Research and Development of a Fuel Cell/Battery Powered Bus System*, Bethesda, MA: Department of Energy, p. 105, 1990.

BIOGRAPHICAL SKETCH

Jim Fletcher was born on March 29, 1962. After completing a BSME at the University of Florida, he worked for a year before setting off on a year-long, “around-the-world” trip. At the conclusion of the travels, he completed a MSME again from the University of Florida. Upon graduation, he spent the next three years working in Australia at a variety of engineering positions, the best of which was designing hydroelectric plants. His Ph.D. study was very challenging, and included construction or refurbishment of two buildings, operation of a variety of fuel cell engines, near completion of a BSEE, and a position of employment with Georgetown University. With the Ph.D. study completed, he is currently working with major automobile manufacturers to develop the production fuel cell engine.

I certify that I have read this study and that in my opinion it conforms to acceptable standards of scholarly presentation and is fully adequate, in scope and quality, as a dissertation for the degree of Doctor of Philosophy



Vernon P. Roan, Chairman
Professor of Mechanical Engineering

I certify that I have read this study and that in my opinion it conforms to acceptable standards of scholarly presentation and is fully adequate, in scope and quality, as a dissertation for the degree of Doctor of Philosophy



D. Yogi Goswami
Professor of Mechanical Engineering

I certify that I have read this study and that in my opinion it conforms to acceptable standards of scholarly presentation and is fully adequate, in scope and quality, as a dissertation for the degree of Doctor of Philosophy



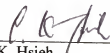
Sherif A. Sherif
Associate Professor of Mechanical
Engineering

I certify that I have read this study and that in my opinion it conforms to acceptable standards of scholarly presentation and is fully adequate, in scope and quality, as a dissertation for the degree of Doctor of Philosophy



William E. Lear
Associate Professor of Mechanical
Engineering

I certify that I have read this study and that in my opinion it conforms to acceptable standards of scholarly presentation and is fully adequate, in scope and quality, as a dissertation for the degree of Doctor of Philosophy



C.K. Hsieh
Professor of Mechanical Engineering

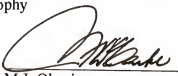
I certify that I have read this study and that in my opinion it conforms to acceptable standards of scholarly presentation and is fully adequate, in scope and quality, as a dissertation for the degree of Doctor of Philosophy



Gijs Bosman

Professor of Electrical and Computer
Engineering

This dissertation was submitted to the Graduate faculty of the College of Engineering and to the graduate School and was accepted as partial fulfillment of the requirements for the degree of Doctor of Philosophy


f M.J. Ohanian

Dean, College of Engineering

Winfred M. Phillips

Dean, Graduate School